THE UNIVERSITY OF CALGARY

Dynamics of Pulsed Laminar Jets

by

Prantik Mazumder

A THESIS

SUBMITTED TO THE FACULTY OF GRADUATE STUDIES

IN PARTIAL FULFILLMENT OF THE REQUIREMENTS FOR THE

DEGREE OF

MASTER OF SCIENCE IN ENGINEERING

DEPARTMENT OF CHEMICAL AND PETROLEUM ENGINEERING

CALGARY, ALBERTA.

JULY, 1993

ISBN 0-315-88574-2

THE UNIVERSITY OF CALGARY

FACULTY OF GRADUATE STUDIES

The undersigned certify that they have read, and recommend to the Faculty of Graduate Studies for acceptance, a thesis entitled, "Dynamics of Pulsed Laminar Jets", submitted by Prantik Mazumder in partial fulfilment of the requirements for the degree of Master of Science.

Dr. A.A. Jeje (Supervisor)
Department of Chemical and
Petroleum Engineering

Dr. R.A. Heidemann
Department of Chemical and
Petroleum Engineering

Dr. S.R. Sreenivasan
Department of Physics and
Astronomy

Richard D. Rowe

Dr. R.D. Rowe
Department of Mechanical Engineering

13.9.93

Date

ABSTRACT

The dynamics of laminar jets of water, pulsed through a submerged orifice, are studied. The flow pulsations are characterized by large amplitudes. Schlieren optics were employed for flow visualization. The steady rate of water into the nozzle assembly, the pulsation frequency and its amplitude were the independent variables. At amplitudes of ~10% and frequencies ~0.5 Hz, the jet outline was continuous but varicose. A streak of ambient water was drawn into the side of the jet during a short interval of the cycle at frequencies of 1-2 Hz. The entrained water delineated a core region within the jet. At ~2.5 Hz, a distinct rim appeared at the leading edge of the core. When the amplitude was increased, ring vortices formed at amplitudes above 25%. The vortices cascaded along the jet or were discharged singly. Cascading vortices stabilized the jet flow.

The Navier-Stokes equation was solved numerically. Computed streaklines qualitatively matched the experimental observations. Calculated results depended on the velocity profiles imposed at the orifice.

ACKNOWLEDGEMENTS

I wish to express my sincere gratitude to the following individuals who have made this work possible:

My supervisor, Dr. A.A. Jeje, for his guidance and help throughout the course of this study.

The Chemical Engineering technical staff, especially Adolf Kohl, for their assistance in the design and construction of the experimental apparatus.

Dr. V. Ramesh, of the Department of Mechanical Engineering, for his technical advice in designing the cams.

Brent Daley of the Mechanical Engineering Department for fabricating the cams.

Dr. J.D.M. Belgrave, of the Chemical Engineering Department for his time and helpful suggestions regarding the numerical simulation.

Manjit Singh, of the Electrical Engineering Department for his help in preparing this thesis.

Dr. Doug Phillips and Dr. Paul Wellings, of the Academic Computing Services for their help regarding the use of the AIX computing system.

All the secretarial staff in the Department of Chemical and Petroleum Engineering and friends for their support and encouragement over the duration of the project.

The research was supported by a grant from the Natural Sciences and Engineering Research Council of Canada (to AAJ). The Chemical and Petroleum Engineering Department of the University of Calgary also provided part of the financial support in terms of teaching assistantship (PM).

TABLE OF CONTENTS

LIST OF TABLES

LIST OF FIGURES

NOMENCLATURE

Symbol	Definition
A	Area of grid block
D	Diameter of orifice
f	Frequency of pulsation
J	Momentum rate
p	Pressure
Q	Volume rate
r	Radial distance
Δr	Radial increment
Re_0	Reynolds number, $\frac{D\bar{U}_0}{\nu}$
Re_c	Reynolds number, $\frac{D\bar{U}_c}{\nu}$
Re_{max}	Reynolds number, $\frac{D\bar{U}_0(1+\epsilon)}{\nu}$
Sr	Strouhal number, $\frac{f^*D}{\bar{U}_c}$
t	Time
Δt	Temporal increment
T	Time period of pulsation, $1/f^*$
u	Axial velocity
U	Velocity profile at the orifice

U_0	Instantaneous area-averaged velocty at orifice
$\overline{U}_0$	Steady area-averaged axial velocty at orifice
U_c	Instantaneous centreline velocty at orifice
$\overline{U}_c$	Steady centreline velocity at orifice
v	Radial velocity
z	Axial distance
Δz	Axial increment

Greek Letters

Γ	Circulation
ε	Amplitude of pulsation in fraction of $\overline{U}_0$
ζ	Time interval between consecutive frames of photographs
λ	Refractive index of light
η	Angular frequency
μ	Absolute viscosity
ν	Kinematic viscosity
ψ	Stream function
Ψ	Stream function profile at the orifice
ω	Vorticity

Ω	Vorticity profile at the orifice
ρ	Density

Superscripts

k	Time level
*	Dimensional quantity

Subscripts

H	Horizontal wall
i	Axial index
j	Radial index
V	Vertical wall

1. INTRODUCTION

Pulsed flows with complex but laminar structures are generated in various physiological and physical systems. The ejection of blood from the heart is an important physiological example. During systole the pressure in the left ventricle exceeds the pressure in the ascending aorta and the aortic valve opens (Ganong 1991). Boli of blood are rapidly discharged into the aorta at intervals of $\sim$ 1 second. A typical Reynolds number in the aorta, the largest vessel in the mammalian circulatory system (about 2.5 cm diameter), is approximately 1200. Respiratory flow is also periodic. The flow occurs in bifurcating channels with diameters which progressively decrease towards the alveoli. The flow of air is laminar within most of the lung tree structure. Other biological examples include high frequency (20-20,000 Hz) but low amplitude displacements of fluid inside the cochlea of the inner ear in response to the vibration of the tympanic membrane; fluid movements in the semi-circular canal, the device responsible for humans maintaining upright balance; and the discharge of jets by marine animals like squids for locomotion.

In the foregoing examples, the flows are constrained by bounding surfaces. Mixing of fluids occurs primarily as a result of longitudinal dispersion and circulation involving laminar eddies as influenced by the wall. However, when a same fluid, jets form and mixing patterns are often very different. In gas furnaces, combustors (Vermeulen et al., 1991), internal combustion engines, spray dryers, tar sand extraction processes (Ross, 1990) and numerous other industrial facilities, the jets may not interact significantly with the wall. Furthermore, typically these are "steady" turbulent jets. Turbulent jets are employed for waste dispersal e.g. through smoke stacks and sewage pipes submerged in large bodies of water, aircraft propulsion and in the cutting of refractory metals.

In many applications, jets are pulsed as an inherent consequence of the operation of a system, such as the combustion gases in automobile exhaust from a reciprocating engine. Steam injected into subcooled water forms bubbles and produces pulsed jets at ~ (15 - 700) Hz frequencies. This has been useful in processing granular solids (Ross, 1990). Pulsing may be carried out deliberately to achieve other effects. Turner (1960) has suggested that chimney exhaust be pulsed to produce ring vortices so that waste gases can rise to higher levels in the atmosphere. Spacecraft jets are pulsed to alter direction of travel. Ink jets are pulsed at high frequency to produce monodisperse droplets (60 μm) in printing (Sweet, 1965).

Although jets and other free shear flows have been extensively studied (Rodi 1975, List 1982) most of the studies have been concentrated on "steady" turbulent jets (Abramovich 1963, Chen and Rodi 1980), starting jets and plumes (Turner 1962) and single event discharge to produce ring vortices (Maxworthy 1972, Shariff and Leonard 1992). The dynamics of periodic discharge of fluid at high amplitudes of discharge rate and low frequencies, typical of physiological systems in mammals, have been little studied. This study is motivated by the need to provide experimental evidence and numerical models for such systems. In section 1.1, the features of steady and pulsed jets and the differences between them are discussed. The objective and scope of the current work are presented in section 1.2.

1.1 Single phase jets

The problem of interest is introduced through a description of single phase jets produced by steady injection of a fluid into a large body of stagnant, unstratified fluid in a pool. Both the injected and ambient fluids are to be completely miscible. Such jets belong to the class of free shear flows produced when two fluid bodies moving at different velocities interact (Rodi 1975). Jets are often distinguished from mixing layers and wakes, the other examples of free shear flows. Velocity profiles and the existence of boundary layers at the source (of a jet) which give rise to rotationality in the flow stream are seldom considered although such boundary layers cause instability and formation of eddies in wake flows (List, 1982). Via jets momentum and energy are discharged through a slit or an orifice into the ambient fluid. In the process, the momentum supplied at the source is convected downstream while it is re-distributed between the injected fluid and the advected portion from the ambient. In the absence of body forces like buoyancy the momentum is conserved downstream (Tritton 1988). For turbulent jets, the temporal-mean velocity profile becomes Gaussian several nozzle diameters away from the orifice. Since the profiles are identical when normalized, they are termed self similar (Abramovich 1963, Rodi 1975). In spite of achieving similar profiles at about twenty nozzle diameters, however, the flow structures are not necessarily self preserving (Rodi, 1975) until much further downstream. The latter is not of consideration in laminar jets. In view of the foregoing, it is obvious that jets have two or more regions; i.e., a zone of flow development or establishment where velocity profiles continuously change, and a zone of developed flow. Two other important issues not yet commented upon are that, at least for turbulent jets, a potential core zone of uniform velocity exists up to about three to five nozzle diameters from the source and all jets, laminar and turbulent, disintegrate downstream under the influence of ubiquitous disturbances in the media.

Laminar and turbulent steady jets are expected to be different in their evolution and ultimate fate. First, the potential core of uniform velocity appears to be absent from laminar jets because of the dominance of viscous forces. In fact, the velocity along the jet axis may increase initially, similar to entrance pipe flow (Schlichting 1968), before decreasing downstream. The reference to a potential core by Akaike and Nemoto (1988) for laminar flows is therefore a misrepresentation. In the absence of eddies which entrain ambient fluids at the edge of the jet, mixing and jet spread are not be as significant for laminar compared to turbulent jets. The mean velocity profiles are consequently expected to differ away from the orifice, i.e., the laminar profile may also not be Gaussian. Furthermore, while small-scale eddies are continuously destroyed in turbulent jets and the high shear field at the edge leads to engulfment and stretching of ambient fluids (entrainment) (List 1982), laminar jets develop eddy structures after becoming unstable downstream of the source. That is, one pattern is becoming more macroscopically organized while the other becomes less structured. Thus both the flows and the evolution are different for the two patterns and the analytical schemes require different perspectives. Finally, the kinetic energy associated with laminar flow is dissipated primarily by viscous action. In turbulent flows, eddy interactions are significant.

The disintegration of steady laminar jets is due to shear layer instability (Michalke and Freymuth 1966, Wille 1963). At extremely low Reynolds number (based on orifice diameter), the jet simply spreads. Momentum diffuses laterally and Schlichting's (1933, 1968) solution involving a point source is valid at distances away from the virtual origin (Andrade et al. 1937, Rankin et al., 1968). The flow patterns are steady and stable over a considerable distance from the orifice (Beavers and Wilson, 1969). At intermediate Reynolds numbers through orifices of finite dimensions, the vorticity sheets discharged from sharp edges (Goldstein, 1938) roll up to form vortex rings (Yule 1978, Beavers and Wilson, 1970). As Reynolds number is increased, the surface of discontinuity becomes thinner (Akaike and Nemoto, 1989) and the roll up of the shear layer occurs faster and closer to the vorticity source. Becker and Massaro (1968) and Yule (1978), have presented pictures of the shear layer roll up events.

As earlier noted, fluids injected at a slow but steady rate via a nozzle or a slit can remain laminar only for a limited distance from the orifice. Moreover, the flow patterns near the orifice can be considerably influenced either by acoustic excitation or pulsation of the source fluid into the pool (such as via reciprocating devices or diaphragms). The latter phenomenon is of current interest. Vorticity with time-dependent strength is continually discharged through the orifice (McCormack et al. 1966). It is the relative rates at which vorticity diffuses, is convected axially or induces the curling of the surface of discontinuity (Kaden, 1931) which are suggested to lead to the variety of flow structures observed.

A number of features distinguish pulsed jets and steady or excited jets. For the same time averaged flow rate of fluid through the orifice, a pulsed jet introduces higher momentum and kinetic energy into the pool than the others. As an illustration, consider that the transient velocity profile at the orifice is spatially uniform and can be represented by

$$U_0(t^*) = \bar{U}_0(1 + \varepsilon \sin 2\pi f^* t^*) \tag{1.1}$$

where ε is the amplitude of velocity (or volumetric rate) variation and f^* is the frequency for a harmonic pulsation superposed on a mean flow. The momentum and kinetic energy of the stream discharged are respectively $(1 + \varepsilon^2/2)$ and $(1 + 3\varepsilon^2/2)$ times those values for steady jets at similar mass rates of injection. The excess quantities may be utilized to develop and maintain complicated flow structures from initiations provided in the non-uniform vorticity fields.

1.2 Objective and scope of study

The current work is aimed at determining the kinematic and dynamic characteristics of pulsed jets at Reynolds numbers low enough for the flow to be laminar but high enough for the structure to be stable for ten to twenty nozzle diameters from the source. Conditions at which ring vortices form and the patterns through which the flow structures evolve are of primary interest. The system is restricted to an axisymmetric jet of water discharged through a circular orifice submerged in a large reservoir of water at the same temperature. The orifice is sharp edged at the rim of a uniformly converging nozzle. The intent was to achieve a near uniform velocity profile at the discharge. The experiments are to provide mainly qualitative information. No velocity or pressure measurements were made. Numerical simulation of the flow was performed through solving a finite difference form of the complete Navier Stokes equation. For comparison purposes, computations were done at the same flow conditions as for the experiments. Since the velocity profiles at the orifice were not determined as functions of time and space, arbitrary velocity profiles which were anticipated to qualitatively resemble the source profiles with different discharge ports were used for the calculations. A nearly flat profile is expected for a hole in a thin plate and a parabolic profile describes the discharge through a long circular pipe.

The rest of the thesis is organized as follows. Relevant work earlier reported are reviewed in chapter 2. The experimental procedure and apparatus are described in chapter 3. The numerical analysis is described in detail in chapter 4. The experimental and computational results are presented in chapter 5. The results are discussed in chapter 6. Finally, the conclusions and recommendations are presented in chapter 7.

2. LITERATURE REVIEW

Jets are free shear flows produced by the discharge of fluids from a nozzle or a slit into an ambient fluid. Such flows have generally been studied under two categories, namely, laminar and turbulent jets. "Steady" turbulent jets are characterized by rapid and random fluctuations superimposed on a mean flow. The time-average velocity is nearly uniform over the area of the source for fluid discharge. When the ambient is stagnant, distinct zones of potential flow, laminar entrainment and temporal-mean velocity profile changes are obvious (Abramovich 1963, Chen and Rodi 1980, List 1982). For laminar jets, even when external disturbances are impressed on the flow, such disturbances may not be significantly amplified near the source. However, away from the source the disturbances are not attenuated and they grow to induce turbulence downstream. Entrainment rates, flow structures and energy dissipation patterns are also different for laminar and turbulent jets. Apart from natural disturbances, laminar jets can be made unsteady through acoustic excitation or pulsatile injection at the source. A brief review on the theoretical and experimental work already done on steady and unsteady jets are presented in this chapter. The first section involves the theories developed (Schlichting 1933) and the velocity measurements (Andrade et al. 1937 and others) done on steady laminar jets. Unsteady jets such as starting jets, excited jets and pulsed jets, are discussed in the second section. The basic features of excited jets and starting jets are also discussed in this section.

2.1 Steady Laminar Jets

The review in this section is restricted to steady laminar jets, when the injected fluid and the unstratified, stationary ambient fluid are the same or are completely miscible. A parameter characterizing the flow of a steady laminar jet is the Reynolds number, which is the ratio of inertial to viscous forces. For a jet to be steady and laminar the Reynolds number should be low (Pai, 1954). The jet emerges with a particular initial velocity profile which depends in part on the nozzle or slit geometry. As the jet emerges from the orifice, it interacts with the surrounding stationary fluid and sets the adjacent fluid into motion. As a consequence, the jet spreads as it moves downstream and the volume rate of flow at any axial position increases with distance from the orifice. The rate of increase of volumetric flow or the entrainment is considered to be due primarily to viscous streaming of the ambient fluid rather than to lateral transport of mass through formation and disintegration of eddies as anticipated for turbulent jets (List, 1982). The source momentum of the jet is shared with the ambient fluid without loss or gain. That is, the momentum across any plane perpendicular to the axis of the jet remains constant. This leads to a decrease in the area average velocity with distance from the orifice.

The flow field in a jet can be classified into two regions. A region of flow development exists in the immediate neighbourhood of the orifice. Here, the velocity profile readjusts itself. Beyond this region, the velocity profiles would approach a form theoretically derived by Schlichting (1933, 1968) if the flow remained stable.

Schlichting (1933, 1968) presented analytical solutions for both plane and axisymmetric laminar jets. Gradients for velocity along the flow direction are neglected relative to radial gradients. This is equivalent to an assumption that lateral diffusion is much greater than axial diffusion or that the boundary layer thickness is much smaller than the length scale along the flow direction. The latter cannot be related to the orifice diameter since in Schlichting's (1933, 1968) analysis of axisymmetric jet, the jet was assumed to emerge from a point source into a stagnant medium. The momentum across any plane perpendicular to the jet's axis was also assumed constant. No vorticity was injected into the ambient through the orifice and there were no transition zones within which velocity profiles changed shape. The pressure gradient along the direction of flow was neglected. The momentum and continuity equations, applied are:

$$u^* \frac{\partial u^*}{\partial z^*} + v^* \frac{\partial u^*}{\partial r^*} = \nu \frac{1}{r^*} \frac{\partial}{\partial r^*}\left(r^* \frac{\partial u^*}{\partial r^*}\right) \tag{2.1}$$

$$\frac{\partial u^*}{\partial z^*} + \frac{\partial v^*}{\partial r^*} + \frac{v^*}{r^*} = 0 \tag{2.2}$$

where, u^* and v^* are the velocity components along the axial and radial co-ordinates z^* and r^* respectively and ν is the kinematic viscosity. All the variables are dimensional. The boundary conditions are the symmetry and stationary conditions;

$$r^* = 0 \quad : \quad v^* = 0 \; ; \; \frac{\partial u^*}{\partial r^*} = 0 \tag{2.3}$$

$$r^* = \infty \quad : \quad u^* = 0 \tag{2.4}$$

Solutions for the axial and radial velocity components, u^* and v^*, were derived by Schlichting (1933, 1968) as

$$u^* = \frac{3J}{8\pi\mu z^*} \frac{1}{(1+\frac{1}{4}\xi^2)^2} \tag{2.5}$$

$$v^* = \frac{1}{4}\sqrt{\frac{3J}{\pi\rho}} \frac{1}{z^*} \frac{\xi - \frac{1}{4}\xi^3}{(1+\frac{1}{4}\xi^2)^2} \tag{2.6}$$

where,

$$\xi = \frac{1}{\nu}\sqrt{\frac{3J}{16\pi\rho}} \frac{r^*}{z^*} \tag{2.7}$$

Parameter $J = 2\pi\rho\int_0^\infty u^{*2} r dr$ is the momentum rate through any plane perpendicular to the axis of the jet, μ is the absolute viscosity and ρ is the density of the fluid. The results in equations (2.5) to (2.7) show that velocities decrease proportional to z^{*-1} as distance increases from the source. Also while u^* divided by the axial velocity along the centreline changes monotonically from 1 to 0 in the radial direction at an axial plane, similarly normalized v^* has three real roots at ξ equals 0 and $\pm$ 2. The radial velocity is consequently outwardly directed for $0 \leq \xi \leq 2$ and inwardly directed for $\xi > 2$. Equation (2.6) thereby provides information on jet spread. It is important to note that the radial profile for u^* does not satisfy a Gaussian form as is obtained for turbulent jets (Chen and Rodi, 1981). The term $(1+(\xi/2)^2)^{-2}$ is approximately equal to $e^{-\xi^2/2}$ only for small values of ξ, i.e. near the jet axis. Theoretically, the decay of axial velocity (u^*) in the radial direction is slower than Gaussian. However, the axial velocity profiles when normalized with the values along the jet axis at different z^*, become coincident, i.e. the patterns are similar.

The volumetric rate of flow $Q^* = 2\pi\int_0^\infty u^* r^* dr^*$ (volume per second) increases with the distance from the orifice owing to entrainment from the surroundings. On substituting equation (2.5) one obtains that :

$$Q^* = 8\pi\nu z^* \tag{2.8}$$

The volumetric rate of flow is hence independent of the source conditions, viz., mass rate and momentum of the jet. It is informative to consider this result in terms of spreading of the jet. If the velocity and hence the mass rate at the orifice is high, the jet remains relatively narrow; if the velocity or the mass rate is small, the jet broadens out, setting more ambient fluid in motion so that the volume rate of flow at any axial distance from the orifice remains exactly equal to that with high velocity (Pai, 1954). Schlichting's analysis has been shown to be valid only for a region far from the " source ", as the expressions for velocity components diverge when $z^* \rightarrow 0$.

Andrade and Tsien (1937) compared Schlichting's (1933, 1968) solution to results for a real jet issuing from a circular aperture of finite size. Fluid issued through a converging tube with the outlet diameter equal to 0.91 mm. The area contraction ratio was ~ 36. The orifice nearly constitutes a point source. Velocity patterns were determined in a liquid into liquid jet for $55 \leq Re \leq 300$. The term Re is the Reynolds number based on the diameter of and the average fluid velocity through the orifice. Suspended particles moving in the medium were photographed to provide streak lines from which it was possible to determine the velocity distributions away from the orifice. Without direct experimental proof, the investigators suggested that the velocity profile at the source was uniform. This implies that 1) the flow is irrotational and 2) a region for velocity profile transformation existed between the region where velocity was uniform and where it satisfied equation 2.5. These issues were not discussed by the authors. They simply noted that Schlichting's (1933, 1968) results were not matched near the orifice. Schlichting's solution also required locating a virtual source at a point below the orifice. An expression was derived relating the position of the virtual origin from the orifice with the Reynolds number.

Akaike and Nemoto (1989) studied the velocity profile in the developing region of an axisymmetric water jet. A uniformly converging nozzle with an exit diameter of 10 mm and an area contraction ratio of 5.76 was used to achieve a near uniform profile in the central portion of a jet. The boundary layer developed along the nozzle wall was considered thin. The authors nevertheless distinguished between the region of uniform velocity at the centre (misnamed potential core) and the region with shear. The radius of the region of uniform velocity (r_{co}) increased as the nozzle Reynolds number was increased. The velocity profiles were monitored with tiny hydrogen bubbles and a miniature cone-type hot probe in the Reynolds number range 100 to 600. Numerical calculation of the velocity profiles was carried out with finite difference approximation of the Navier-Stokes equations. An arbitrary velocity profile was used as the boundary condition at the source. It was assumed that the potential core extended to a radius r_{co}, where the velocity profile was flat. A boundary layer with a quadratic profile was assumed to exist between r_{co} and the wall of the nozzle. The axial velocity increased within the potential core region presumably because of viscous resistance by the ambient fluid. The core also shrank until it disappeared much as the "entrance length" of a pipe flow system. Beyond the potential core zone, the velocity along the jet axis gradually decreased. Velocity profiles for jets with both initially parabolic and flat profiles are found to approach Schlichting's solution far from the nozzle; the approach being faster for a parabolic profile at the orifice. The plot of centreline velocity versus axial distance showed that, for a jet with parabolic profile at source, the nondimensional centreline velocity decreased monotonically downstream of the orifice. The agreement between experimental results and calculations was good for jets with initially parabolic profiles. For jets with initially uniform profiles, the decay of the centreline velocity occurred faster in experimental results than was noted in the computation. This discrepancy is probably due to differences in the non-uniform velocity profile which prevailed at the nozzle and the flat profile that was assumed for the computations.

In the foregoing, references have been made to the nozzle geometry employed in the different investigations. The geometric factor is important for many reasons. In fluid flow, orifices are not ideal or without energy loss. In applying the Bernoulli equation, corrections to calculated average velocities through orifices are made by multiplying with an empirical coefficient (of discharge, C_d). (Perry and Chelton, 1973). Differently shaped orifices have different coefficient values. Apparently the shapes also have influence on the stability of the laminar jet produced. This issue has been investigated by Ito and Seno (1979). Nozzle configurations included pipes (Length to Diameter ratio of 10 and 1/10), smoothly converging nozzle with an area contraction ratio of 21.6, and a hole in a plate orifice. The Reynolds number (based on average velocity at the orifice) range was 300-8000. The form of instability of the jet column appeared to be correlated to the thickness of the boundary layer at the outlet of the nozzle. The boundary layer forms the "zone of separation" between the jet and the ambient fluid. The photographs presented by Ito and Seno (1979) illustrate that these are streets of vorticity which become curled in cylindrical structures. For a boundary layer thinner than 0.21 orifice diameter (both for the smoothly converging channel and the hole in a plate orifice), i.e. at high Reynolds number, vortices which formed were axisymmetric. At low Reynolds number, the boundary layer was greater than 0.21 orifice diameter and the structure of the vortices appeared helical.

2.2 Unsteady Jets

In the previous section only steady jets, where the velocity fields do not change with time have been discussed. Unsteadiness can be achieved in several ways. Jets or plumes such as cigarette smoke which are laminar and steady close to the source ultimately become unsteady at distances far from the source which vary with the frequency and amplitude of the natural and random disturbances in the medium. This transition can more readily be effected through mechanical or acoustic excitations at frequencies at which the jet responds. Extensive theoretical and experimental investigations have been carried out (Mollendorf and Gebhart, 1973; Chanaud and Powell, 1962; Sato, 1960; Mattingly and Chan, 1974; Anderson, 1954, 1955, 1956; Beavers and Wilson, 1970). Stability rather than the dynamics has been the principal focus for jets with steady efflux velocities. Amplitudes of the imposed disturbances are normally very low and frequencies are in the audible range, from 20 to 20,000 Hz. A disturbance mode is considered to cause instability if perturbations were amplified and the jet ultimately disintegrated. Perturbations caused by disturbances at other frequencies decayed under the influence of viscous forces.

Another example of unsteady jets occurs when a flow is suddenly initiated through a nozzle into an ambient fluid. Jets of this kind are termed as "starting jets". As soon as the fluid comes out of the orifice a "spherical vortex" is proposed to form ahead of the regular jet (Turner, 1962). Since the vortex moves downstream at a rate slower than the liquid in its wake, it is continuously supplied with fresh material and thus increases in diameter (Abramovich and Solan, 1973). That is, the vortex continuously gains mass and momentum. At the same time, the velocity of axial displacement or translation of the vortex decreases due to viscous interaction with the ambient fluid. Abramovich and Solan (1973) investigated the velocity field development of a starting jet by hot film measurement. The centreline velocity at any axial position remained zero until the spherical vortex approached very close to that position. The velocity increased to its final steady state value as the vortex passed through it. The velocity along the axis exceeds the steady value within the period for the vortex to pass over the sensor.

Pulsed jets are produced when the flow rate at the orifice is periodic. Such jets can be mechanically driven either by a reciprocating piston or by a vibrating diaphragm inside a specially designed nozzle assembly (Sweet, 1965; Bousfield et al., 1990). The momentum at and the vorticity discharge from the nozzle vary with time unlike in steady jets. As a result, flow patterns very different from those observed for steady jets can be anticipated. Primitive variables which completely describe the development of flow can be identified as the velocity profiles at the orifice, the amplitude of variation of the discharge rate ε and the characteristic frequency of pulsation f^*. From these, dimensionless quantities can be derived such as the Reynolds number based on the orifice diameter and the velocity at the nozzle averaged both spatially and over time. The velocity profile at the orifice and the amplitude give a measure of the vorticity distribution and the rates of discharge into the ambient fluid. The frequency is a measure of the time scale for transport of momentum and vorticity. Literature on this problem is sparse.

Seno et al. (1987) performed experiments to investigate the effect of "controlled" pulsation on the behaviour of vortex rings. Flow structures were observed through the movement of clouds of hydrogen bubbles. Velocities were measured with hot film (anemometer) probes. Both techniques have their drawbacks. Dense clouds of bubbles modify flow structures and may even locally alter the viscosity of the medium. Film probes are intrusive and require careful data interpretation with laminar flows. Experiments were performed with Reynolds number $\bar{U}_0 D/\nu$ varying between 1895 and 6005 corresponding to transition (not laminar) flow, Strouhal number $Sr = f^* D/\bar{U}_c$ between 0 and 5.25 or $3.86 \le f^* \le 22.48$ Hz and the amplitude ε between 0 and 0.466. The terms $\bar{U}_0$ and $\bar{U}_c$ are the steady area averaged and centreline axial velocities at the orifice. They termed the jets "natural" when the flow at the nozzle was not pulsed. Because of the technique used to generate pulsed flows, the flow is not truly harmonic and f^* is not a single perturbation frequency for the system. This is obvious from the skewed velocity-time plots and the lack of closure on material balance in their Figure 3. Since the authors reported sporadic formation of vortices in "natural jets" (also in Ito and Seno, 1979) the modes of disturbances induced by pulsation are not uniquely identifiable and many of their conclusions can be challenged. In any case, their results are presented on the basis of time-averaged velocities with the consequence that interesting features get submerged. One important result pertinent to the current study which the authors failed to mention or discuss is that the velocity profiles at the source, as revealed for laminar discharge (their Figure 10), appear to change with time within a cycle of pulsation. A curved (not parabolic) front is obtained at certain instances followed by nearly flat profiles in the centre of the jet for most of the duration of a cycle of pulsation. Vortex sheets appear to exist at the edge of the orifice. Such data, averaged over time, would appear to suggest that a perpetual potential core exists at the orifice (their Figure 4) when none such does persist.

The three papers which directly address pulsed laminar jets from an analytic or numerical simulation perspective, have involved different methods. Seno, Kageyama and Ito (1988) have used the vortex ring element method with inviscid, axisymmetric conditions. The annular shear layer or the "sheet of separation" between the jet and pool fluids was replaced by an array of identical vortex ring elements. The velocity of each vortex ring was calculated as the summation of the self induced velocity and the total induced velocity caused by all other vortex ring elements calculated by the Biot-Savart law of induction (Lighthill, 1961). Computations were done for Re = 2000, 4000 and 6000 with Sr varying between 0.3 to 5.2. Amplitudes of pulsation were varied from 0.005 to 0.3. The simulation adequately described the initial curling of the vortex sheet and the velocity of displacement of vortex rings when compared to experimental results.

McCormack et al.'s (1966) analysis pertained to how mechanical vibration of the separation plate affected the dynamics of a two dimensional laminar mixing layer between two parallel streams. The vibration at high frequencies was assumed to produce periodic fluctuation of vorticity at the source. Velocity components and the vorticity were separated into steady and fluctuating components. These terms were substituted into the unsteady vorticity transport equation with boundary layer approximations and the resulting equations were linearized. This analysis predicts an increase in the mean velocity components and a decrease in the jet spread rate which becomes appreciable at velocity modulation greater than 20%.

Lai and Simmons (1981) reported numerical solution for a sinusoidally pulsed two dimensional jet. They involved a boundary layer approximation and neglected the pressure gradient terms. The solution method involved finding a suitable transformation for the coordinate space. Computations were done at angular frequency ($\eta = 2\pi f^*$) = 0.1, 1.5, 10 and 100 for amplitude of velocity pulsation (ε) 0.1 and 0.2. The results for the mean velocity profiles, mean entrainment and mean centreline velocity were found to differ insignificantly from those for steady jets. The authors ascribed this computed response to pulsation to the absence of any large scale vortices within the range of frequencies and amplitudes computed.

3. EXPERIMENTS

The equipment and the optical system used for flow visualization are described in this chapter.

3.1 Apparatus

A schematic diagram of the apparatus is given in Figure 3.1. The facility was a tank of 1 m square horizontal section by 1.1 m high, filled with distilled water to a height of 1 m. Two of the vertical parallel sides were 19 mm (3/4 inch) thick tempered glass plate, free from optical inhomogeneity (schliere). The other two sides were 19 mm thick plexiglass. The tank bottom was a 38 mm thick layer of high density polystyrene foam pasted onto an aluminium plate. A nozzle assembly was centrally fastened on the tank bottom. A schematic diagram of the nozzle assembly is shown in figure 3.2. The nozzle assembly was constructed from a stainless steel (SS 316) cylinder of diameter 100 mm. Three holes of diameter 10 mm each were drilled circumferentially 120^0 apart. The channels led into a radial cavity. Test fluid was supplied at a steady rate through these holes. Through an adjustable radial slit (0.5 mm - 2.0 mm) the test fluid was fed into the central chamber of diameter 10 mm. The radial cavity and the slit acted as a flow regulator ensuring uniform radial flow into the central chamber. Above the plane

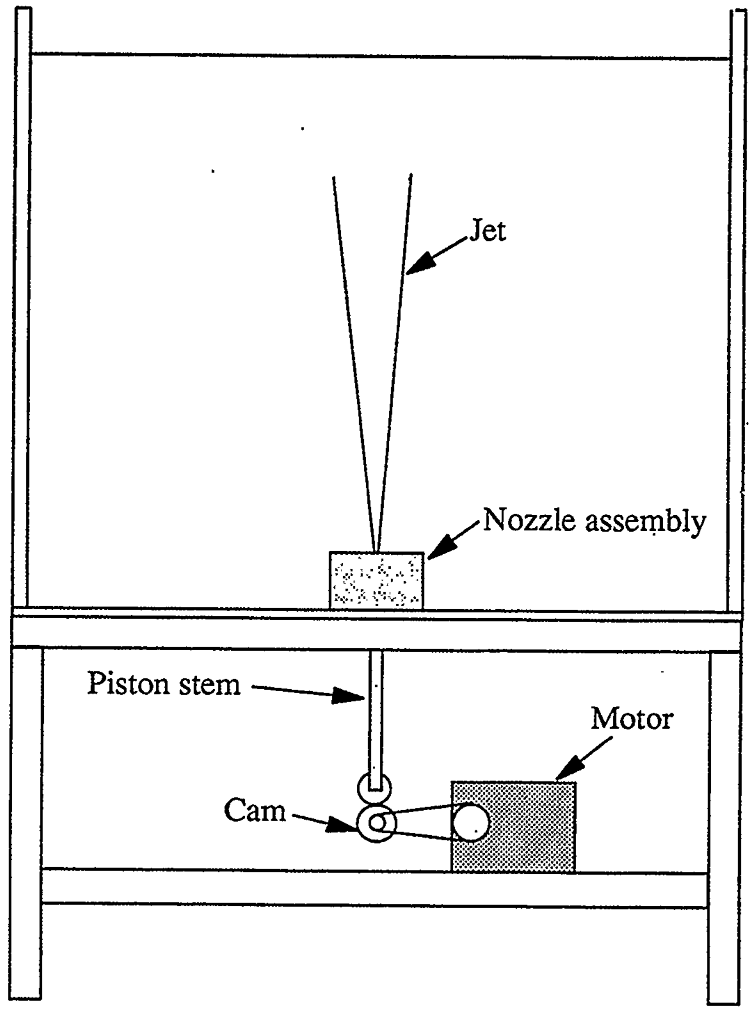

Figure 3.1 Schematic diagram of experimental apparatus

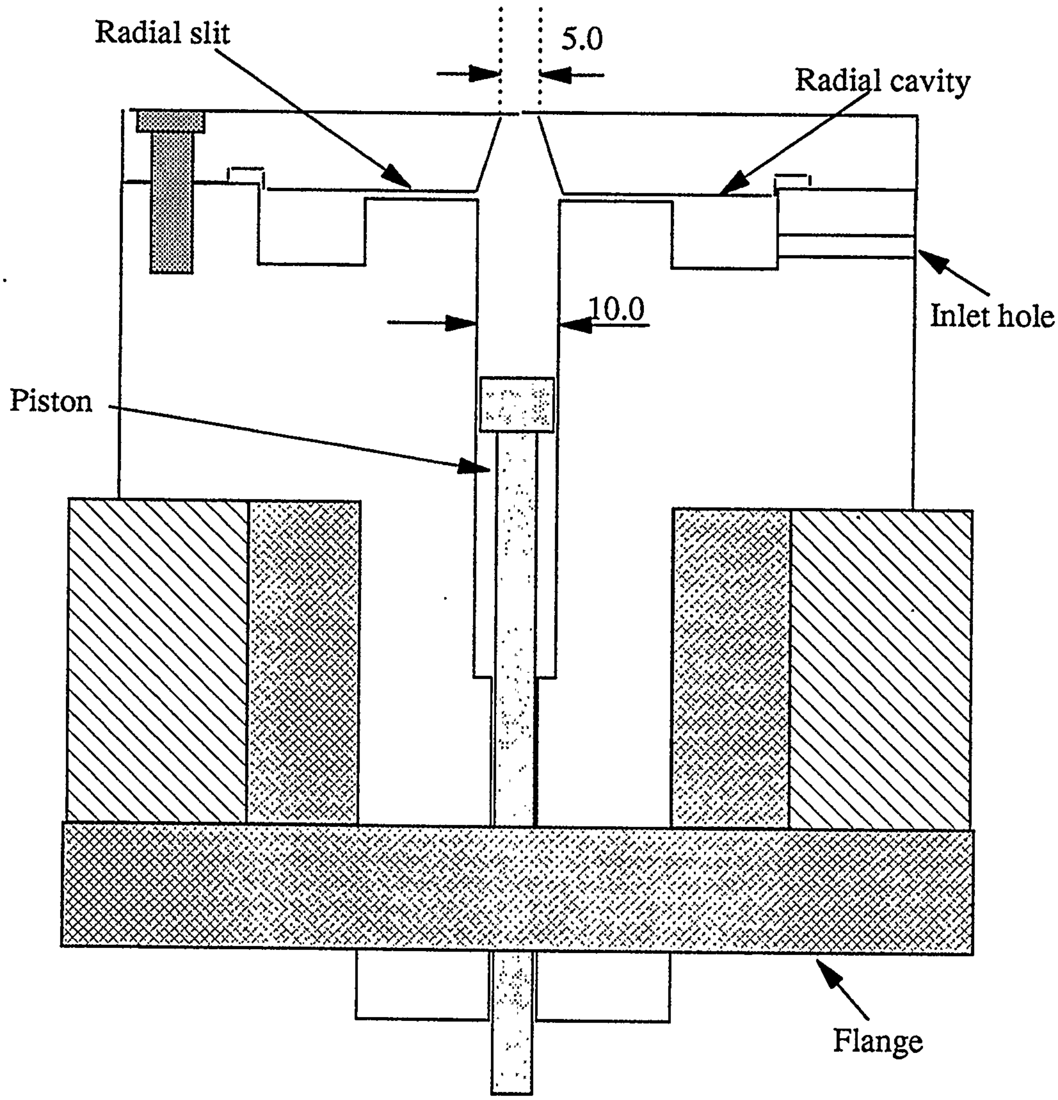

Figure 3.2 Schematic diagram of nozzle assembly

of the slit the chamber had a variable cross-section and converged into an orifice of diameter 5 mm. A near uniform velocity profile at the nozzle exit was expected due to the convergence.

A stainless steel piston was located inside the chamber. The stem of the piston was kept in direct contact with a cam (see Figure 3.1). The cam was connected to the head of a gear-box by a belt-drive. The gear box was connected to a 1/3 h.p, 115 v, 60 Hz, a.c motor operating at 1725 r.p.m. The output from the gear-box could be continuously varied between 0 to 400 r.p.m. The rotary motion of the cam was translated into the axial oscillation of the piston inside the nozzle assembly. The movement of the piston superimposed a pulsation on the steady average efflux velocity at the orifice. The adjustable radial gap mentioned earlier, created a large pressure drop across it ensuring that no backflow of water into the inlet tunnels occurred during the upward travel of the piston.

The instantaneous area averaged velocity of the jet at the nozzle exit can be expressed in the following form,

$$U_0(t^*) = \bar{U}_0(1 + \varepsilon \sin 2\pi f^* t^*) \tag{3.1}$$

where, $U_0(t^*)$ is the instantaneous area-averaged axial velocity, $\bar{U}_0$ is the steady flow velocity in the absence of pulsation, f^* is the frequency in Hz, ε is the velocity amplitude and t^* is the time in sec. The velocity amplitude ε depended pon the particular cam in operation. A large number of cams were designed and used to obtain different ε at different frequencies for different steady average velocity at the nozzle. The design of the cams is discussed in appendix A.

3.2 Preparation of test fluid

A solution of 0.5% ethyl alcohol in distilled water was used as the test fluid. The dynamic and optical properties of pure water and the ethanol solution at 20^0C are presented in Table 3.1. The density and viscosity of the test fluid were not significantly different from those of pure water. The flow visualization was made possible due to a small difference in the refractive index between the jet solution and the ambient water.

In making the solution, approximately 200 ml of 100% ethanol was added to 30 l of distilled water in an overhead tank. The solution was stirred for a few minutes to ensure uniformity. The solution was then filtered and fed into a storage vessel.

3.3 Schlieren optics

A schematic of the schlieren optics is shown in figure 3.3. The source of illumination was a 200 W mercury vapour arc lamp placed behind a variable aperture pinhole. The beam of light emerging from the pinhole passed through two lenses and fell on a front coated spherical mirror of focal length 110 cm. The parallel beam of light reflected from the mirror passed through the test section and

Table 3.1 Dynamic and optical properties of pure water and 0.5% ethyl alcohol solution at 20^{0}C (Weast, 1977)

	ρ	υ	λ
Pure water	.9982	1.004	1.33299
Ethyl alcohol solution	.9973	1.026	1.333

The table columns are:

ρ = Density at 20^{0}C, kg/l

υ = Kinematic viscosity at 20^{0}C, cS

λ = Index of refraction at 20^{0}C relative to air for sodium yellow light

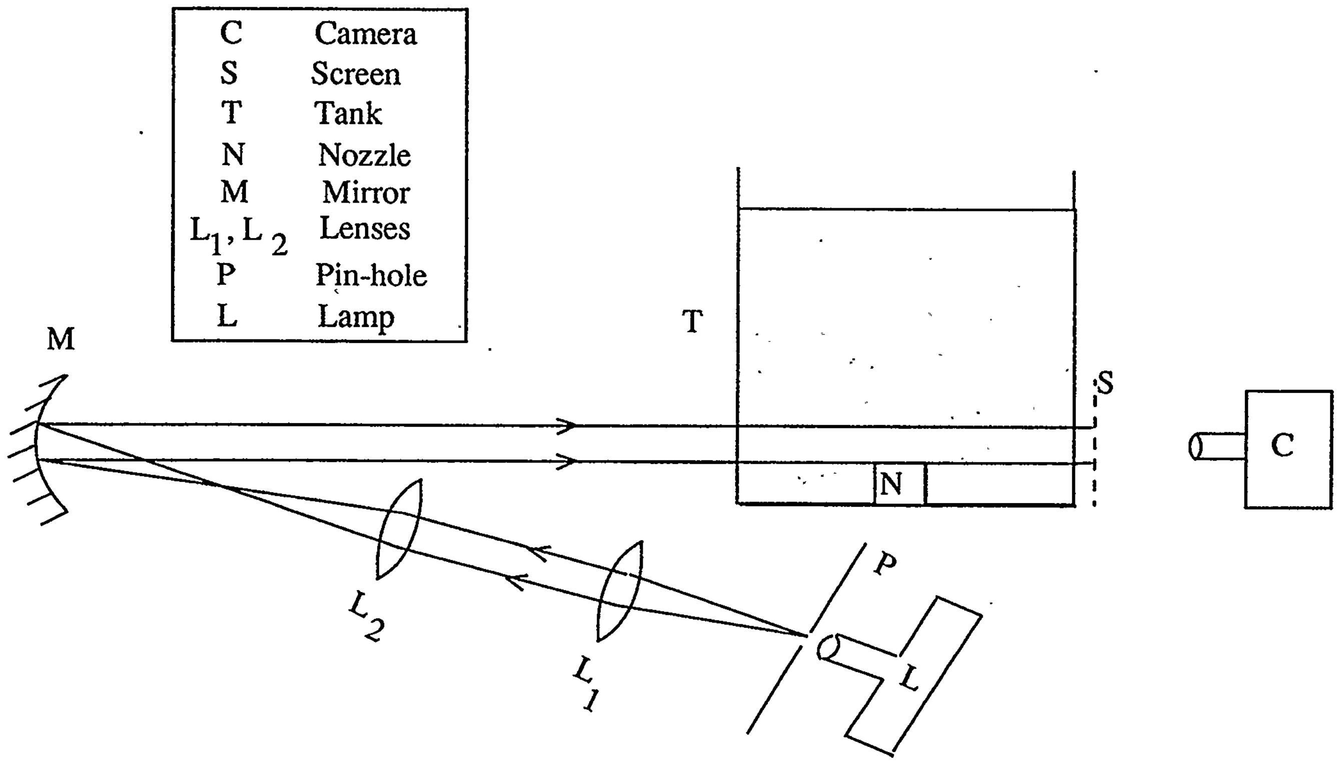

Figure 3.3 Optical arrangement for schlieren photographs

fell on a screen attached to the wall of the tank. The image on the screen was photographed by a Nikon, single lens reflex camera equipped with a motor drive. Pictures were taken at 3.3 frames per second. The maximum exposure was 1/2000 seconds with Kodak T_{max} film.

3.4 Experimental procedure

The tank was filled with distilled water. The water was allowed to stand overnight in order to minimize large scale motions. The temperature of the water was $(20 \pm 1)^0$C. The test fluid was forced out from the storage vessel using compressed air at a constant pressure of 2.5 psi gauge and fed into the nozzle. A very steady flow was attained. The volumetric flow rate was regulated and measured by a rotameter connected in series between the storage vessel and the nozzle. The calibration of the rotameter is discussed in appendix B. It required about 1-2 minutes for the rotameter reading to be steady. The piston-driving motor was then switched on and set at the desired angular velocity. The angular velocity in revolution per minute (r.p.m) was measured by an optical tachometer. The angular velocity fluctuated slightly about the desired r.p.m during the experimental runs. The maximum fluctuation was found to be ± 5.05%. The three important parameters were the Reynolds' number Re_0, frequency f^* and the velocity amplitude ε. The Reynolds' number was defined as,

$$Re_0 = \frac{\bar{U}_0 D}{\nu}$$

where, D and ν were the orifice diameter and the kinematic viscosity of 0.5% ethyl alcohol solution at 20°C. $\bar{U}_0$ was calculated by dividing the volumetric rate by the area of the orifice.

The conditions for the experiments performed are shown in table 3.2.

Table 3.2 : Outline of Experiments performed

Re_0	$\bar{U}_0$ (mm/s)	f^* (hz)	ε (%)
102.7	20.54	0	0
		0.5	10
		1.0	
		1.7	
		2.0	
		2.4	
		1.5	15
		1.0	50
		1.25	
		2.5	
		0.5	100
		2.0	
		2.5	
200.3	40.06	0	0
		2.0	10
		1.0	25
		2.5	
		5.0	
		0.5	50
		2.5	
		1.0	100
502.5	100.5	0	0
		1	10
		1.25	
		2.5	
		5.0	
		2.5	25
		5.0	50

4. ANALYSIS AND NUMERICAL SCHEME

The equations which describe the flow fields are the Navier-Stokes and continuity equations. The coordinate system is cylindrical and swirls are considered absent. This means that only the space variables r^* and z^* and time t^* constitute the independent variables for the system. The Navier-Stokes equation in the primitive variables (u^*, v^*) is formulated in terms of stream function and vorticity. The resulting expressions are set in a finite difference form and solved numerically. The approach and methods to accomplish the tasks are described in this chapter. Since the results are presented as instantaneous streamlines and streaklines, the significance and limitations of these contour display devices are reviewed.

4.1 The transport equations

Pulsed jets are developed, in the calculation procedures, from steady jets which have the same mean volumetric rates through the orifice. At time $t^* = 0$ a sinusoidal perturbation is superimposed on the flow. The velocity profile, normalized with the instantaneous value along the orifice axis was assumed invariant. Consequently, the periodic flow which results can be separated into time and space functions. This is an assumption which is not expected to be satisfied in the experiments for large amplitude pulsations. At stages when discharge rates are high, the flow profiles may differ from those for stages when flow out of the orifice is slow or halted. The equations along the axial and radial directions are respectively;

$$\frac{\partial u^*}{\partial t^*} + u^*\frac{\partial u^*}{\partial z^*} + v^*\frac{\partial u^*}{\partial r^*} = -\frac{1}{\rho}\frac{\partial p^*}{\partial z^*} + \nu\left(\frac{\partial^2 u^*}{\partial z^{*2}} + \frac{\partial^2 u^*}{\partial r^{*2}} + \frac{1}{r^*}\frac{\partial u^*}{\partial r^*}\right) \tag{4.1}$$

$$\frac{\partial v^*}{\partial t^*} + u^*\frac{\partial v^*}{\partial z^*} + v^*\frac{\partial v^*}{\partial r^*} = -\frac{1}{\rho}\frac{\partial p^*}{\partial r^*} + \nu\left(\frac{\partial^2 v^*}{\partial z^{*2}} + \frac{\partial^2 v^*}{\partial r^{*2}} + \frac{1}{r^*}\frac{\partial v^*}{\partial r^*} - \frac{v^*}{r^{*2}}\right) \tag{4.2}$$

where, u^* and v^* are the velocity components in the axial (z^*) and the radial (r^*) directions. The terms p^*, t^*, ρ and ν denote pressure, time, density and kinematic viscosity respectively. With the inclusion of the continuity equation,

$$\frac{\partial u^*}{\partial z^*} + \frac{v^*}{r^*} + \frac{\partial v^*}{\partial r^*} = 0 \tag{4.3}$$

there are three equations and three unknowns. All the variables in equations (4.1) to (4.3) are dimensional. Pressure can be eliminated from equations (4.1) and (4.2) by cross-differentiation and subtracting the resulting expressions. Through adopting the following parameters,

$$r=\frac{r^*}{D},\quad z=\frac{z^*}{D},\quad u=\frac{u^*}{\bar{U}_c},\quad v=\frac{v^*}{\bar{U}_c},\quad t=\frac{t^*\bar{U}_c}{D},\quad Re_0=\frac{\bar{U}_0 D}{\nu},\quad \omega = \frac{D\omega^*}{\bar{U}_c}$$

the resulting nondimensional vorticity transport equation is

$$\frac{\partial \omega}{\partial t} + u\frac{\partial \omega}{\partial z} + v\frac{\partial \omega}{\partial r} - \frac{v\omega}{r} = \frac{(\bar{U}_0 / \bar{U}_c)}{Re_0}\left(\frac{\partial^2 \omega}{\partial z^2} + \frac{\partial^2 \omega}{\partial r^2} + \frac{1}{r}\frac{\partial \omega}{\partial r} - \frac{\omega}{r^2}\right) \tag{4.4}$$

where ω is the vorticity, Re_0 is the Reynolds' number based on the steady average velocity $\bar{U}_0$ at the orifice and $\bar{U}_c$ is the steady centreline velocity at the orifice. The relation between the centreline velocity and the average velocity is given in Appendix C.

Since velocity in the azimuthal direction is assumed to be zero, the only component of vorticity in the field is,

$$\omega = \frac{\partial u}{\partial r} - \frac{\partial v}{\partial z} \tag{4.5}$$

If the stream function ψ is defined as,

$$u = \frac{1}{r}\frac{\partial \psi}{\partial r} \tag{4.6a}$$

then,

$$v = -\frac{1}{r}\frac{\partial \psi}{\partial z} \tag{4.6b}$$

to satisfy the continuity equation. The velocity terms in equation (4.4) may be replaced by the use of (4.6) and the stream function-vorticity (ψ,ω) transport equation is:

$$\frac{\partial\omega}{\partial t} + \frac{1}{r}\frac{\partial\psi}{\partial r}\frac{\partial\omega}{\partial z} - \frac{1}{r}\frac{\partial\psi}{\partial z}\frac{\partial\omega}{\partial r} + \frac{\omega}{r^2}\frac{\partial\psi}{\partial z} = \frac{(\bar{U}_0/\bar{U}_c)}{Re_0}\left(\frac{\partial^2\omega}{\partial z^2} + \frac{\partial^2\omega}{\partial r^2} + \frac{1}{r}\frac{\partial\omega}{\partial r} - \frac{\omega}{r^2}\right) \tag{4.7}$$

The expressions in equations (4.6a) and (4.6b) may be substituted into equation (4.5) to obtain:

$$\omega = \frac{1}{r}\left(\frac{\partial^2\psi}{\partial r^2} + \frac{\partial^2\psi}{\partial z^2} - \frac{1}{r}\frac{\partial\psi}{\partial r}\right) \tag{4.8}$$

The Boundary conditions:

The boundary conditions which apply to this problem are written explicitly as,

At $z=0$ $\quad 0 \leq r \leq 0.5, \quad t > 0$

$$u = U(r)\,(1 + \varepsilon \sin 2\pi ft), \quad v = 0 \tag{4.9a}$$

$$\psi = \Psi(r)\,(1 + \varepsilon \sin 2\pi ft), \quad \omega = \Omega(r)\,(1 + \varepsilon \sin 2\pi ft) \tag{4.9b}$$

At $z=0$ $\quad r > 0.5, \quad$ for all t

$$u = 0, \; v = 0 \tag{4.10a}$$

$$\psi = 0, \; \omega = \frac{1}{r}\frac{\partial^2\psi}{\partial z^2} \tag{4.10b}$$

At $r=0$ For all z, t $$\frac{\partial u}{\partial r} = 0, \; v = 0 \tag{4.11a}$$

$$\psi = \Psi(0)(1 + \varepsilon \sin 2\pi f t), \; \omega = 0 \tag{4.11b}$$

At $r \rightarrow \infty$ For all z, t $$u = 0 \tag{4.12a}$$

$$\frac{\partial \psi}{\partial r} = 0 \tag{4.12b}$$

The functions U(r), Ψ(r) and Ω(r) are the steady velocity, stream function and vorticity profiles at the orifice. The term f is a nondimensional frequency parameter related to its dimensional counterpart f^* by $f = f^* D/U_0$. The term ε is the amplitude of velocity pulsation.

The initial conditions:

The initial conditions for the problem are those for a steady jet. That is,

t = 0, for all r, z
$$\begin{aligned} u &= u_0(r,z) \\ v &= v_0(r,z) \\ \psi &= \psi_0(r,z) \\ \omega &= \omega_0(r,z) \end{aligned} \tag{4.13}$$

The solution for steady flow is obtained through solving the following equations

$$\frac{1}{r}\frac{\partial \psi_0}{\partial r}\frac{\partial \omega_0}{\partial z} - \frac{1}{r}\frac{\partial \psi_0}{\partial z}\frac{\partial \omega_0}{\partial r} + \frac{\omega_0}{r^2}\frac{\partial \psi_0}{\partial z} = \frac{(\bar{U}_0/\bar{U}_c)}{Re_0}\left(\frac{\partial^2 \omega_0}{\partial z^2} + \frac{\partial^2 \omega_0}{\partial r^2} + \frac{1}{r}\frac{\partial \omega_0}{\partial r} - \frac{\omega_0}{r^2}\right) \tag{4.14}$$

$$\omega_0 = \frac{1}{r}\left(\frac{\partial^2\psi_0}{\partial r^2} + \frac{\partial^2\psi_0}{\partial z^2} - \frac{1}{r}\frac{\partial\psi_0}{\partial r}\right) \tag{4.15}$$

subject to the boundary conditions .

$$\text{At } z=0 \qquad 0 \le r \le 0.5, \qquad \begin{aligned} \psi_0 &= \Psi(r) \\ \omega_0 &= \Omega(r) \end{aligned} \tag{4.16}$$

$$\text{At } z=0 \qquad r > 0.5 \qquad \begin{aligned} \psi_0 &= 0 \\ \omega_0 &= \frac{1}{r}\frac{\partial^2\psi_0}{\partial z^2} \end{aligned} \tag{4.17}$$

$$\text{At } r=0 \qquad \text{For all } z \qquad \begin{aligned} \psi_0 &= \Psi(0) \\ \omega_0 &= 0 \end{aligned} \tag{4.18}$$

$$\text{At } r\rightarrow\infty \qquad \text{For all } z \qquad \frac{\partial\psi_0}{\partial r}=0 \tag{4.19}$$

4.2 The Numerical Analysis

The system of partial differential equations which describes both the steady and unsteady jets is solved by a finite difference technique. Ideally, the domain of calculation for the jet in the medium is infinite in both coordinate directions. However, when computational molecules are to be equidistant along any direction, the domain size has to be finite. This means that a boundary is located where one does not exist. However, such a boundary should be sufficiently removed from the object of interest to cause minimal disturbance in the flow dynamics. That is, the problem is transformed into a pseudo-boundary value problem (Grant, 1974). An alternate approach is to map the infinite region in the physical plane into a finite domain by suitable transformations such as the unequally spaced grid of the "tanh" function. This alternative is not adopted here because of the accumulation of excessive artificial viscosity caused by rapid grid expansion to cover an infinite physical domain (Thompson, 1978 ; Fasel, 1979).

4.2.1 Computational domain and grid arrangement

Figure 4.1 shows the schematic of the computational domain used for the numerical simulation. Due to limited storage capacity of the computing system, the computational domain was confined to 10 nozzle diameters along both the axial and radial directions. The rectangle ACDE represents the whole integration region. A rectangular, uniform grid arrangement is laid onto this domain. In order to predict the small scale flow pattern, a very dense grid structure is used. The entire space is discretized with 121 grids along the axial direction and 161 grids along the radial direction. All the variables are defined at the mesh points where the horizontal and vertical grids intersected each other. Subscripts (i, j) refer to z, r coordinates respectively. The mesh spacings along the z and the r directions are 'Δz' and 'Δr'respectively.

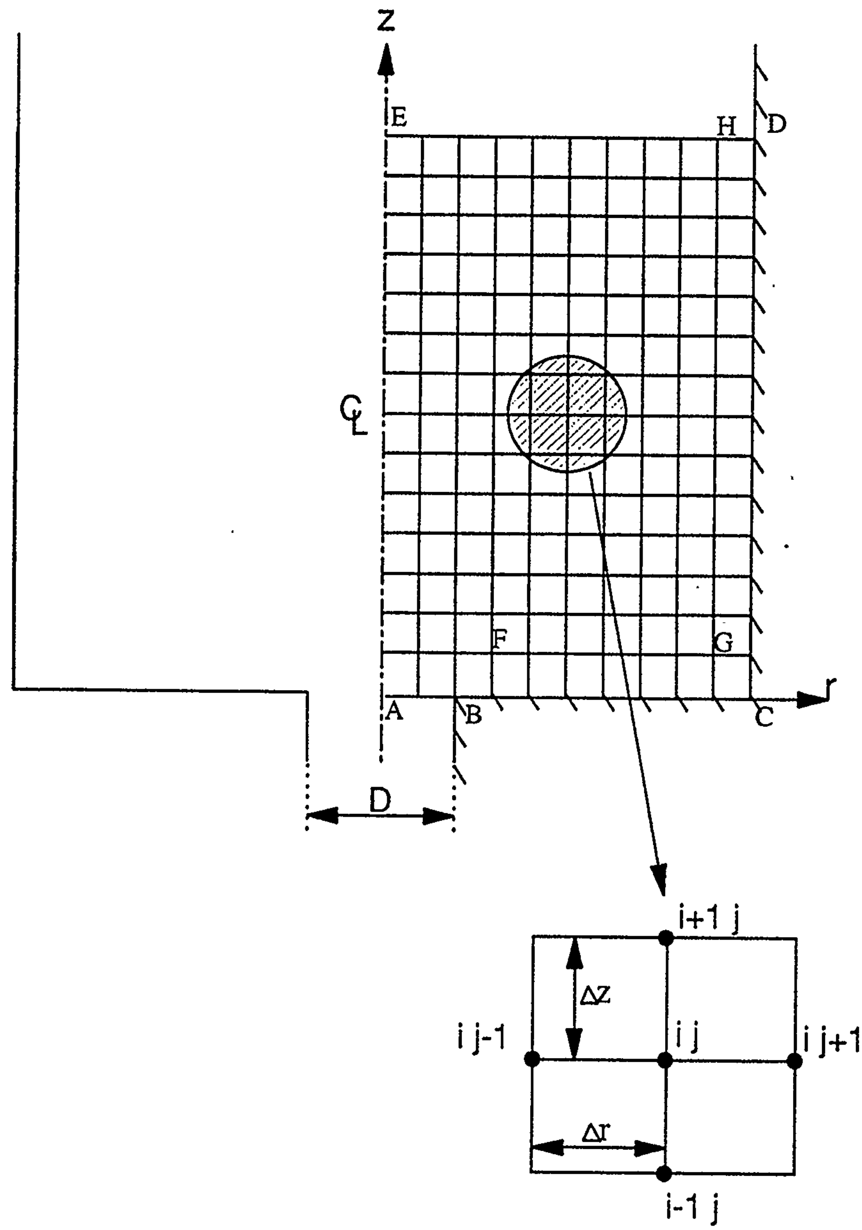

Fig 4.1 Computational domain and grid arrangement

4.2.2 The finite difference equations

4.2.2.a Steady jet:

The set of equations to be solved is comprised of (4.14) and (4.15). Approximating all the derivatives by central differences, the finite difference forms of equations (4.14) and (4.15) are obtained as follows,

$$\begin{aligned}
&\frac{1}{r_j}\frac{(\psi_{0_{i,j+1}}-\psi_{0_{i,j-1}})}{2\Delta r}\frac{(\omega_{0_{i+1,j}}-\omega_{0_{i-1,j}})}{2\Delta z} - \frac{1}{r_j}\frac{(\psi_{0_{i+1,j}}-\psi_{0_{i-1,j}})}{2\Delta z}\frac{(\omega_{0_{i,j+1}}-\omega_{0_{i,j-1}})}{2\Delta r} \\
&\qquad + \frac{\omega_{0_{i,j}}}{r_j^2}\frac{(\psi_{0_{i+1,j}}-\psi_{0_{i-1,j}})}{2\Delta z} \\
&= \frac{(\bar{U}_0/\bar{U}_c)}{Re_0}\Big[\frac{\omega_{0_{i+1,j}}-2\omega_{0_{i,j}}+\omega_{0_{i-1,j}}}{\Delta z^2} + \frac{\omega_{0_{i,j+1}}-2\omega_{0_{i,j}}+\omega_{0_{i,j-1}}}{\Delta r^2} \\
&\qquad + \frac{1}{r_j}\frac{\omega_{0_{i,j+1}}-\omega_{0_{1,j-1}}}{2\Delta r} - \frac{\omega_{0_{i,j}}}{r_j^2}\Big]
\end{aligned} \tag{4.20}$$

$$\begin{aligned}
\omega_{0_{i,j}} = \frac{1}{r_j}\Big(&\frac{\psi_{0_{i,j+1}}-2\psi_{0_{i,j}}+\psi_{0_{i,j-1}}}{\Delta r^2} + \frac{\psi_{0_{i+1,j}}-2\psi_{0_{i,j}}+\psi_{0_{i-1,j}}}{\Delta z^2} \\
&- \frac{1}{r_j}\frac{\psi_{0_{i,j+1}}-\psi_{0_{i,j-1}}}{2\Delta r}\Big)
\end{aligned} \tag{4.21}$$

4.2.2.b Unsteady jet:

A fully implicit finite difference scheme is employed to discretize equations (4.7) and (4.8). Although the scheme is algebraically more complicated than the explicit scheme, it is free from stability problems. Since, the scheme is always stable and non divergent, it allows larger (permissible) step sizes in the analysis (Fox et al., 1972). The finite difference equations corresponding to (4.7) and (4.8) are,

$$
\begin{aligned}
&\frac{\omega_{i,j}^{k+1}-\omega_{i,j}^{k}}{\Delta t} + \frac{1}{r_j}\frac{\psi_{i,j+1}^{k+1}-\psi_{i,j-1}^{k+1}}{2\Delta r}\frac{\omega_{i+1,j}^{k+1}-\omega_{i-1,j}^{k+1}}{2\Delta z} - \frac{1}{r_j}\frac{\psi_{i+1,j}^{k+1}-\psi_{i-1,j}^{k+1}}{2\Delta z}\frac{\omega_{i,j+1}^{k+1}-\omega_{i,j-1}^{k+1}}{2\Delta r} \\
&\quad + \frac{\omega_{i,j}^{k+1}}{r_j^2}\frac{\psi_{i+1,j}^{k+1}-\psi_{i-1,j}^{k+1}}{2\Delta z} \\
&= \frac{(\bar{U}_0/\bar{U}_c)}{Re_0}\left[\frac{\omega_{i+1,j}^{k+1}-2\omega_{i,j}^{k+1}+\omega_{i-1,j}^{k+1}}{\Delta z^2} + \frac{\omega_{i,j+1}^{k+1}-2\omega_{i,j}^{k+1}+\omega_{i,j-1}^{k+1}}{\Delta r^2}\right. \\
&\quad \left. + \frac{1}{r_j}\frac{\omega_{i,j+1}^{k+1}-\omega_{i,j-1}^{k+1}}{2\Delta r} - \frac{\omega_{i,j}^{k+1}}{r_j^2}\right]
\end{aligned}
\tag{4.22}
$$

$$
\omega_{i,j}^{k+1} = \frac{1}{r_j}\left(\frac{\psi_{i,j+1}^{k+1}-2\psi_{i,j}^{k+1}+\psi_{i,j-1}^{k+1}}{\Delta r^2} + \frac{\psi_{i+1,j}^{k+1}-2\psi_{i,j}^{k+1}+\psi_{i-1,j}^{k+1}}{\Delta z^2} - \frac{1}{r_j}\frac{\psi_{i,j+1}^{k+1}-\psi_{i,j-1}^{k+1}}{2\Delta r}\right) \tag{4.23}
$$

where, k and Δt denote the time index and temporal increment respectively.

4.2.3 Treatment of the boundary conditions

Specification of the boundary conditions for the type of flow fields described in this work is a challenging problem. Describing the free boundaries (CD and ED in figure 4.1) with a computationally compatible and at the same time physically realistic, accurate and stable method poses great difficulties. Due to the absence of any unique scheme of handling these problems, a number of numerical experiments were carried out and finally the following approximations were arrived at along the grid boundaries.

(a) Surface ED (outflow boundary) in Figure 4.1 : The terms $\frac{\partial^2\omega}{\partial z^2}$ and $\frac{\partial^2\psi}{\partial^2 z}$ can not be evaluated using space-centered differences since no mesh points exist beyond ED. Following Grant (1974) it was assumed that along this boundary the double derivatives with respect to z are much smaller than the double derivatives with respect to r, i.e

$$\frac{\partial^2\omega}{\partial z^2} << \frac{\partial^2\omega}{\partial r^2} \tag{4.24}$$

$$\frac{\partial^2\psi}{\partial z^2} << \frac{\partial^2\psi}{\partial r^2} \tag{4.25}$$

This is equivalent to setting both $\frac{\partial^2\omega}{\partial z^2}$ and $\frac{\partial^2\psi}{\partial z^2}$ equal to zero on ED. Therefore, the differential equations describing the condition at ED are

$$\frac{1}{r}\frac{\partial\psi_0}{\partial r}\frac{\partial\omega_0}{\partial z} - \frac{1}{r}\frac{\partial\psi_0}{\partial z}\frac{\partial\omega_0}{\partial r} + \frac{\omega_0}{r^2}\frac{\partial\psi_0}{\partial z} = \frac{(\bar{U}_0/\bar{U}_c)}{Re_0}\left(\frac{\partial^2\omega_0}{\partial r^2} + \frac{1}{r}\frac{\partial\omega_0}{\partial r} - \frac{\omega_0}{r^2}\right) \tag{4.26}$$

$$\omega_0 = \frac{1}{r}\left(\frac{\partial^2\psi_0}{\partial r^2} - \frac{1}{r}\frac{\partial\psi_0}{\partial r}\right) \tag{4.27}$$

$$\frac{\partial\omega}{\partial t} + \frac{1}{r}\frac{\partial\psi}{\partial r}\frac{\partial\omega}{\partial z} - \frac{1}{r}\frac{\partial\psi}{\partial z}\frac{\partial\omega}{\partial r} + \frac{\omega}{r^2}\frac{\partial\psi}{\partial z} = \frac{(\bar{U}_0/\bar{U}_c)}{Re_0}\left(\frac{\partial^2\omega}{\partial r^2} + \frac{1}{r}\frac{\partial\omega}{\partial r} - \frac{\omega}{r^2}\right) \tag{4.28}$$

$$\omega = \frac{1}{r}\left(\frac{\partial^2\psi}{\partial r^2} - \frac{1}{r}\frac{\partial\psi}{\partial r}\right) \tag{4.29}$$

(4.26) and (4.27) are the equations for the steady jet, whereas (4.28) and (4.29) are the equations for the unsteady jet. Approximating all the first derivatives with respect to z by backward difference, the following finite difference equations are obtained,

$$\frac{1}{r_j}\frac{(\psi_{0_{i,j+1}}-\psi_{0_{i,j-1}})}{2\Delta r}\frac{(\omega_{0_{i,j}}-\omega_{0_{i-1,j}})}{\Delta z} - \frac{1}{r_j}\frac{(\psi_{0_{i,j}}-\psi_{0_{i-1,j}})}{\Delta z}\frac{(\omega_{0_{i,j+1}}-\omega_{0_{i,j-1}})}{2\Delta r} + \frac{\omega_{0_{i,j}}}{r_j^2}\frac{(\psi_{0_{i,j}}-\psi_{0_{i-1,j}})}{\Delta z} = \frac{(\bar{U}_0/\bar{U}_c)}{Re_0}\left[\frac{\omega_{0_{i,j+1}}-2\omega_{0_{i,j}}+\omega_{0_{i,j-1}}}{\Delta r^2} + \frac{1}{r_j}\frac{\omega_{0_{i,j+1}}-\omega_{0_{1,j-1}}}{2\Delta r} - \frac{\omega_{0_{i,j}}}{r_j^2}\right] \tag{4.30}$$

$$\omega_{0_{i,j}} = \frac{1}{r_j}\left(\frac{\psi_{0_{i,j+1}}-2\psi_{0_{i,j}}+\psi_{0_{i,j-1}}}{\Delta r^2} - \frac{1}{r_j}\frac{\psi_{0_{i,j+1}}-\psi_{0_{i,j-1}}}{2\Delta r}\right) \tag{4.31}$$

$$\frac{\omega_{i,j}^{k+1}-\omega_{i,j}^{k}}{\Delta t}+\frac{1}{r_j}\frac{\psi_{i,j+1}^{k+1}-\psi_{i,j-1}^{k+1}}{2\Delta r}\frac{\omega_{i,j}^{k+1}-\omega_{i-1,j}^{k+1}}{\Delta z}-\frac{1}{r_j}\frac{\psi_{i,j}^{k+1}-\psi_{i-1,j}^{k+1}}{\Delta z}\frac{\omega_{i,j+1}^{k+1}-\omega_{i,j-1}^{k+1}}{2\Delta r}$$
$$+\frac{\omega_{i,j}^{k+1}}{r_j^2}\frac{\psi_{i,j}^{k+1}-\psi_{i-1,j}^{k+1}}{\Delta z}=\frac{(\bar{U}_0/\bar{U}_c)}{Re_0}\cdot\left[\frac{\omega_{i,j+1}^{k+1}-2\omega_{i,j}^{k+1}+\omega_{i,j-1}^{k+1}}{\Delta r^2}\right.$$
$$\left.+\frac{1}{r_j}\frac{\omega_{i,j+1}^{k+1}-\omega_{i,j-1}^{k+1}}{2\Delta r}-\frac{\omega_{i,j}^{k+1}}{r_j^2}\right] \tag{4.32}$$

$$\omega_{i,j}^{k+1}=\frac{1}{r_j}\left(\frac{\psi_{i,j+1}^{k+1}-2\psi_{i,j}^{k+1}+\psi_{i,j-1}^{k+1}}{\Delta r^2}-\frac{1}{r_j}\frac{\psi_{i,j+1}^{k+1}-\psi_{i,j-1}^{k+1}}{2\Delta r}\right) \tag{4.33}$$

(b) Surface CD (outer boundary) : A problem similar to the above is posed at this surface since the terms $\frac{\partial^2\psi}{\partial r^2}$ and $\frac{\partial^2\omega}{\partial r^2}$ cannot be evaluated. The asymptotic boundary conditions (equations (4.12a, 4.12b) or (4.19)) needed to be modified so that they could be handled numerically. Akaike et al. (1988) imposed Schlichting's velocity profile along this boundary. This approach is, however, not suitable for the present work as Schlichting's solution is valid only for steady jets. Grant (1974) treated this boundary in a manner similar to the outflow boundary ED and neglected the terms $\frac{\partial^2\psi}{\partial r^2}$ and $\frac{\partial^2\omega}{\partial r^2}$. This approach also failed for the present work since the solution algorithm converged to different solutions depending on the different initial guesses. Grant did not encounter this problem since he used an explicit time marching algorithm, in which case he did not have to solve a large system of nonlinear simultaneous equations.

In order to obtain a well posed system, a solid wall was assumed along this boundary in the present work. The wall was kept at a distance of 10 nozzle diameters from the axis in order to have a small wall effect on the jet (Ito et al. 1979). The position of the wall could not be extended due to the limited storage capacity of the computing system.

The boundary conditions are modified as follows,

$$\text{At } r=10, \qquad z > 0 \qquad \psi = 0, \quad \frac{1}{r}\frac{\partial^2 \psi}{\partial r^2} = \omega \tag{4.34}$$

$$\text{At } r=10, \qquad z > 0 \qquad \psi_0 = 0, \quad \frac{1}{r}\frac{\partial^2 \psi_0}{\partial r^2} = \omega_0 \tag{4.35}$$

The second order difference formulation derived from a Taylor's series expansion (Roache, 1972) is used to approximate these equations. The higher order difference formulations are not used as they increase the band width of the Jacobian matrix. On representing the vertical wall surface by V, one obtains

$$\omega_{i,V}^{k+1} = \frac{2\,(\psi_{i,V-1}^{k+1} - \psi_{i,V}^{k+1})}{r_V\, \Delta r^2} \tag{4.36}$$

$$\omega_{0_{i,V}} = \frac{2\,(\psi_{0_{i,V-1}} - \psi_{0_{i,V}})}{r_V\, \Delta r^2} \tag{4.37}$$

(c) Horizontal wall adjacent to the jet BC : The boundary conditions at this surface are given by equations (4.10b) or (4.17). On representing the horizontal wall by H, one obtains the following difference equations

$$\omega_{H,j}^{k+1} = \frac{2\,(\psi_{H+1,j}^{k+1} - \psi_{H,j}^{k+1})}{r_j\,\Delta z^2} \tag{4.38}$$

$$\omega_{0_{H,j}} = \frac{2\,(\psi_{0_{H+1,j}} - \psi_{0_{H,j}})}{r_j\,\Delta z^2} \tag{4.39}$$

(d) The orifice AB : The conditions are represented by equations (4.9a) and (4.9b) for an unsteady jet and by equation (4.16) for a steady jet. The functions U(r), Ψ(r) and Ω(r) are the nondimensional mean velocity, stream function and vorticity profile at the orifice. Three different arbitrary velocity profiles were used.

$$\text{Profile I :} \quad U(r) = 1 - (2r)^2 \tag{4.40}$$

$$\text{Profile II :} \quad U(r) = 1 - (2r)^6 \tag{4.41}$$

$$\text{Profile III} \quad U(r) = 1 - (2r)^{10} \tag{4.42}$$

The profiles are plotted in figure 4.2 for comparison. Profile I, Profile II and Profile III will be termed as parabolic, sixth power and tenth power profiles in the subsequent sections. The corresponding stream function and vorticity profiles are,

$$\text{Profile I:} \quad \begin{aligned} \Psi(r) &= \frac{r^2}{2} - r^4 - 0.0625 \\ \Omega(r) &= -\,8r \end{aligned} \tag{4.43}$$

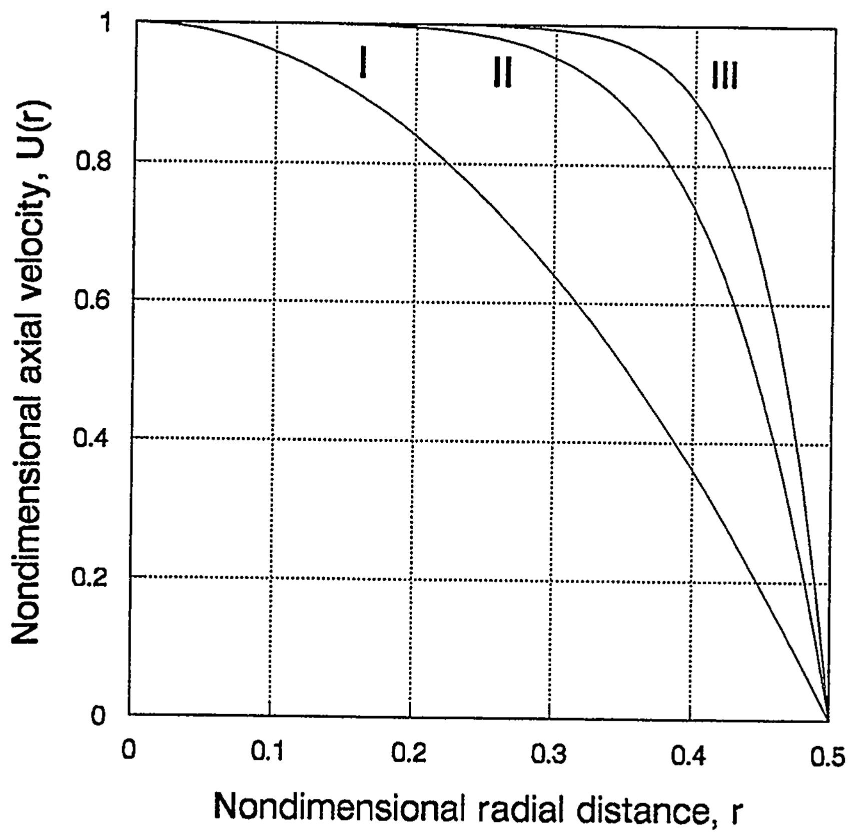

Figure 4.2 : Axial velocity profile at the orifice.

$$\text{Profile II:} \qquad \Psi(r) = \frac{r^2}{2} - \frac{2^6}{8} r^{*} - 0.09375 \qquad (4.44)$$
$$\Omega(r) = -384r$$

$$\text{Profile III:} \qquad \Psi(r) = \frac{r^2}{2} - \frac{2^{10}}{12} r^{12} - 0.104167 \qquad (4.45)$$
$$\Omega(r) = -10240\, r^9$$

The derivation of streamfunction and vorticity is dicussed in Appendix C.

(e) The centreline AE : Along the centreline the boundary conditions are given by Equations (4.11b) and (4.18) for steady jet and unsteady jet respectively.

4.2.4 Solution procedure

a) Steady jet :

For a single mesh point (i, j) the equations (4.20) and (4.30) can be represented in the following form:

$$\phi_{i,j} [\ \omega_{0_{i-1,j}}, \psi_{0_{i-1,j}}, \omega_{0_{i,j-1}}, \psi_{0_{i,j-1}}, \omega_{0_{i,j}}, \psi_{0_{i,j}}, \omega_{0_{i,j+1}}, \psi_{0_{i,j+1}}, \omega_{0_{i+1,j}}, \psi_{0_{i+1,j}}\ ] = 0 \quad (4.46)$$

Similarly the equations (4.21) and (4.31) can also be written as,

$$\gamma_{i,j} [\ \omega_{0_{i-1,j}}, \psi_{0_{i-1,j}}, \omega_{0_{i,j-1}}, \psi_{0_{i,j-1}}, \omega_{0_{i,j}}, \psi_{0_{i,j}}, \omega_{0_{i,j+1}}, \psi_{0_{i,j+1}}, \omega_{0_{i+1,j}}, \psi_{0_{i+1,j}}\ ] = 0 \quad (4.47)$$

When the equations (4.46) and (4.47) are written for all the grid points, a set of 2x120x159 non linear algebraic equations results which must be solved for the vorticity and the stream function at each point. These system of equations are coupled. Decoupling of the equations with an iteration loop was attempted which showed a slow convergence for low values of Re_0 (~ 10). For higher Re_0 (≥50) the convergence rate deteriorated even further and the iteration finally failed to converge at all. In the present method, the convergence was improved enormously by solving the system of equations simultaneously. The convergence is further improved by substituting equation (4.37) for the values of $\omega_{i,j+1}$ along GH and equation (4.39) for the values of $\omega_{i-1,j}$ along FG. This result in elimination of the unknown wall vorticities from the system of equations and hence no initial guess and updating of the wall vorticity is required. Newton's method is used to solve the system of nonlinear equations. The solution algorithm is as follows (Burden et al., 1989)

STEP 1 : Represent the system of equations (4.46) and (4.47) in a more general form as,

$$\Phi(X) = 0 \tag{4.48}$$

$$\Gamma(X) = 0 \tag{4.49}$$

where, **X** is the solution vector defined as

$$\mathbf{X} = (x_1, x_2, x_3, \ldots\ldots\ldots, x_N)^T \tag{4.50}$$

and,

$$\Phi(x_1,x_2,x_3,\ldots\ldots\ldots,x_N) = [\ \phi_1(x_1,x_2,\ldots,x_N),\ \phi_2(x_1,x_2,\ldots,x_N),\ldots\ldots,\ \phi_N(x_1,x_2,\ldots,x_N)\ ] \tag{4.51}$$

$$\Gamma(x_1,x_2,x_3,\ldots\ldots\ldots,x_N) = [\ \gamma_1(x_1,x_2,\ldots,x_N),\ \gamma_2(x_1,x_2,\ldots,x_N),\ldots\ldots,\ \gamma_N(x_1,x_2,\ldots,x_N)\ ] \tag{4.52}$$

where, $x_i = \omega_{i,j}\ ,\ \psi_{i,j}$

STEP 2: Define the Jacobian matrix $\mathbf{J(X)}$ by

$$\mathbf{J(X)} = \begin{bmatrix} \frac{\partial\phi_1(\mathbf{X})}{\partial x_1} & \frac{\partial\phi_1(\mathbf{X})}{\partial x_2} & \cdots\cdots & \frac{\partial\phi_1(\mathbf{X})}{\partial x_N} \\ \frac{\partial\gamma_1(\mathbf{X})}{\partial x_1} & \frac{\partial\gamma_1(\mathbf{X})}{\partial x_2} & \cdots\cdots & \frac{\partial\gamma_1(\mathbf{X})}{\partial x_N} \\ \frac{\partial\phi_2(\mathbf{X})}{\partial x_1} & \frac{\partial\phi_2(\mathbf{X})}{\partial x_2} & \cdots\cdots & \frac{\partial\phi_2(\mathbf{X})}{\partial x_N} \\ \frac{\partial\gamma_2(\mathbf{X})}{\partial x_1} & \frac{\partial\gamma_2(\mathbf{X})}{\partial x_2} & \cdots\cdots & \frac{\partial\gamma_2(\mathbf{X})}{\partial x_N} \\ \cdot & \cdot & \cdots\cdots & \cdot \\ \cdot & \cdot & \cdots\cdots & \cdot \\ \frac{\partial\phi_N(\mathbf{X})}{\partial x_1} & \frac{\partial\phi_N(\mathbf{X})}{\partial x_2} & \cdots\cdots & \frac{\partial\phi_N(\mathbf{X})}{\partial x_N} \\ \frac{\partial\gamma_N(\mathbf{X})}{\partial x_1} & \frac{\partial\gamma_N(\mathbf{X})}{\partial x_2} & \cdots\cdots & \frac{\partial\gamma_N(\mathbf{X})}{\partial x_N} \end{bmatrix} \tag{4.53}$$

STEP 3: Make an initial guess of the solution vector as,

$$\mathbf{X}^0 = (x_1^{\,0}, x_2^{\,0}, x_3^{\,0}, \ldots\ldots\ldots, x_N^{\,0}) \tag{4.54}$$

STEP 4: Compute $\Phi(\mathbf{X})$, $\Gamma(\mathbf{X})$ and $\mathbf{J(X)}$

STEP 5: Define the right hand side vector $\mathbf{F(X)}$ as

$$\mathbf{F(X)} = [\ \phi_1(\mathbf{X}), \gamma_1(\mathbf{X}),\ \phi_2(\mathbf{X}),\ \gamma_2(\mathbf{X}), \ldots\ldots,\ \phi_N(\mathbf{X}),\ \gamma_N(\mathbf{X})\ ]^T \tag{4.55}$$

STEP 6: Solve the linear system of equations

$$\mathbf{J(X)}\ \delta\mathbf{X} = -\ \mathbf{F(X)} \tag{4.56}$$

STEP 7 : Improve the solution vector as,

$$X = X + \delta X \tag{4.57}$$

STEP 8 : If $\| \delta X \|_{\infty} < 10^{-6}$ stop calculation. Otherwise go to step 4

b) Unsteady jet :

The system of equations (4.22), (4.23), (4.32) and (4.33) are solved for every time step. The steady state solution is used as the initial guess for the first time step. Steps 4-8 mentioned earlier are followed until convergence. The solution vector at the first time step is used as the initial guess for the second time step and so on. The computation is carried out until the maximum time level is reached.

4.2.5 Streak line

Streak lines are computed and plotted for numerical flow visualization. A streak line is defined as a continuous line passing through the loci of all the particles passing through the same point. From three different locations which were fixed at the orifice, passive marker particles were released at short intervals and their positions were tracked by numerical integration following the method used by Hama (1962). It is important to recognize that monitoring a flow domain with streakline patterns has its limitations and requires care in interpretation.

Hama (1962), for example, calculated the streaklines in a shear flow perturbed by a stable travelling wave. The streaklines at the critical layer (interface of two different streams of fluid moving at different velocities) were always found to roll up irrespective of the wave parameters. This, according to the author might lead to an incorrect impression that the waves were amplified and developed into discrete vortices, despite the fact that the wave was infact, stable (nonamplifying).

The procedure to generate streaklines is outlined as follows (Hama 1962). Consider one single source at z_0 and r_0. The motion of a particle discharged from this point is governed by the equations

$$\frac{dz}{dt} = u(z(t),r(t),t) \tag{4.58}$$

$$\frac{dr}{dt} = v(z(t),r(t),t) \tag{4.59}$$

The position of the particle at time t is given by

$$z(t) = \int_{t_0}^{t} u(z(t),r(t),t)dt + z_0 \tag{4.60}$$

$$r(t) = \int_{t_0}^{t} v(z(t),r(t),t)dt + r_0 \tag{4.61}$$

The integration of equations (4.60) and (4.61) was carried out by a step-by-step time marching algorithm,i.e,

$$z_1(t_0 + \Delta t) = u(z_0, r_0, t_0)\Delta t + z_0 \tag{4.62}$$

$$r_1(t_0 + \Delta t) = v(z_0, r_0, t_0)\Delta t + r_0 \tag{4.63}$$

and

$$z_1(t_0 + 2\Delta t) = u(z_1, r_1, t_0 + \Delta t)\Delta t + z_1 \tag{4.64}$$

$$r_1(t_0 + 2\Delta t) = v(z_1, r_1, t_0 + \Delta t)\Delta t + r_1 \tag{4.65}$$

and so on. The subscript 1 refers to particle No. 1. A short time $\Delta\tau$ after the particle No. 1 is released , No. 2 particle is marked at the same location z_0, r_0. The path of No. 2 particle is similarly given by

$$z_2(t_0 + \Delta\tau + \Delta t) = u(z_0, r_0, t_0 + \Delta\tau)\Delta t + z_0 \tag{4.66}$$

$$r_2(t_0 + \Delta\tau + \Delta t) = v(z_0, r_0, t_0 + \Delta\tau)\Delta t + r_0 \tag{4.67}$$

and so on. The locus of all the particles marked at the same location gives the streak line at that particular time level.

The velocity of a marker particle inside a grid block is computed by averaging the velocities at the four surrounding grid points. An area-weighting scheme (Sarpkaya, 1989) is used as shown in figure 4.3. The velocity of the marker particle is computed as,

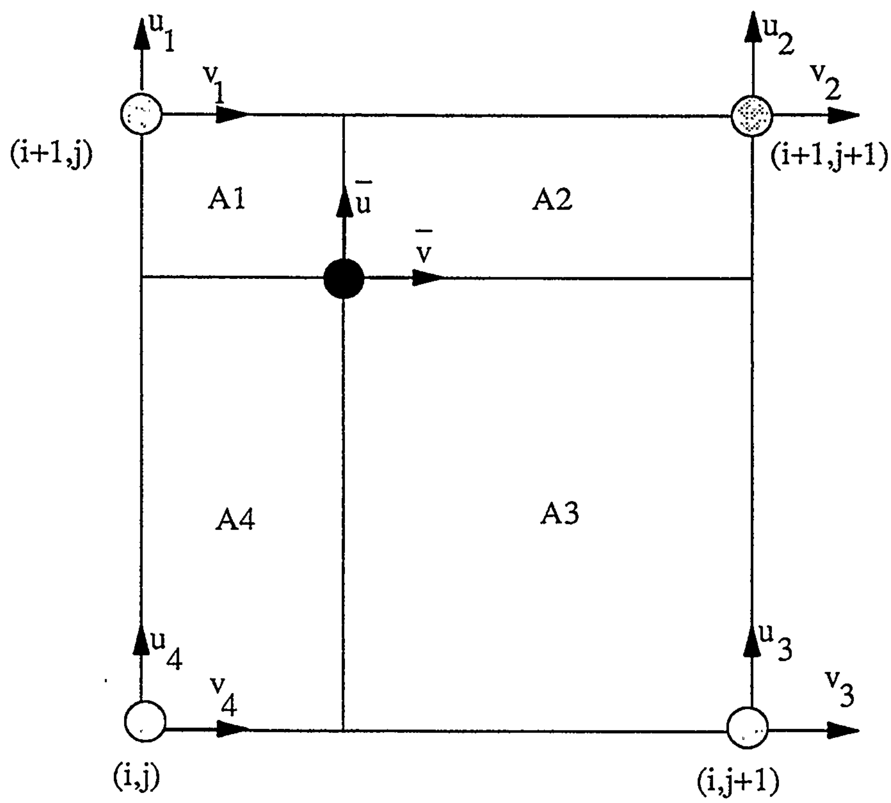

Figure 4.3 Area averaging scheme

$$\bar{u} = \frac{u_1A3 + u_2A4 + u_3A1 + u_4A2}{A} \tag{4.69}$$

$$\bar{v} = \frac{v_1A3 + v_2A4 + v_3A1 + v_4A2}{A} \tag{4.69}$$

where, A is the total area of the grid block,i,e,

$$A = A_1 + A_2 + A_3 + A_4 \tag{4.70}$$

The axial and radial velocities at a grid point (i, j) are calculated from equations (4.6a) and (4.6b) as,

$$u_{i,j} = \frac{1}{r_j}\frac{\Psi_{i,j+1} - \Psi_{i,j-1}}{2fa} \tag{4.71}$$

$$v_{i,j} = -\frac{1}{r_j}\frac{\Psi_{i+1,j} - \Psi_{i-1,j}}{2a} \tag{4.72}$$

4.2.6 Streamline contours

A streamline is defined as a continuous curve, within a fluid, for which the tangent at any point is in the direction of the velocity vector at that point (Tritton 1988). For steady flow, the streamline contours are very useful in visualizing the flow field (Kline 1980, Tritton 1988). In all flow visualization experiments with dye injection, however, streaklines are visualized. For steady flow the streaklines and streamlines match with each other since all the particles move along the same streamline on which they were initially discharged. When the flow is unsteady the streamlines vary with time and hence the streaklines and streamlines do not appear to be identical. As the streamline concept is basically mathematical in nature (Kline, 1980) the actual motion of the fluid particles is not fully revealed by them. However, the streamline contours provide useful information about the instantaneous direction and strength of the velocity fields.

The extent of the computations performed is presented in Table 4.1

Table 4.1 Outline of computations performed

Re_0	f^*	ε (%)	Profile
100	0.5	10	III
		100	I, III
	1	10	I, II, III
		50	III
		100	III
	1.25	50	I, II, III
	1.5	7.5	III
	2	10	I, III
		100	III
	2.5	50	III
200	0.5	50	III
		100	III
	1	25	III
		100	III
	2	10	III
	2.5	50	III

5. RESULTS

The experimental and computed results are presented in this section. The experimental observations were made with a Schlieren optical system which detects variations in the gradients of refractive indices. The refractive index of water flowing out of the nozzle was modified relative to the water in the reservoir by adding a low concentration of alcohol (0.5% by weight). Other properties of the injected solution, (particularly the density) were not significantly different from those for water so that buoyancy did not become a factor. The behaviour of steady jets was used to demonstrate that the above requirements were met. The photograph in Figure 5.1 shows a steady jet at a Reynolds number (Re_0) of 240. The jet is laminar for more than 20 nozzle diameters and it shows a small but noticeable spread. Since, the effect of buoyancy, even at low values, is to prevent or hinder the spread of a laminar jet (Mollendorf, 1973), the observation is consistent with the assumption that the buoyancy defect was negligible.

5.1 Steady Jets

Computed streamlines of a steady jet at two different Reynolds numbers are shown in Figure 5.2. The initial velocity profiles at the orifice were 10th power (Profile III, Equation 4.42). Away from the centreline of the jet the streamlines are not perpendicular to the axis of the jet as might be anticipated for a strictly radial

Figure 5.1 : Photograph of a steady jet at $Re_0 = 240$

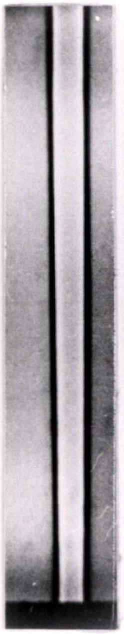

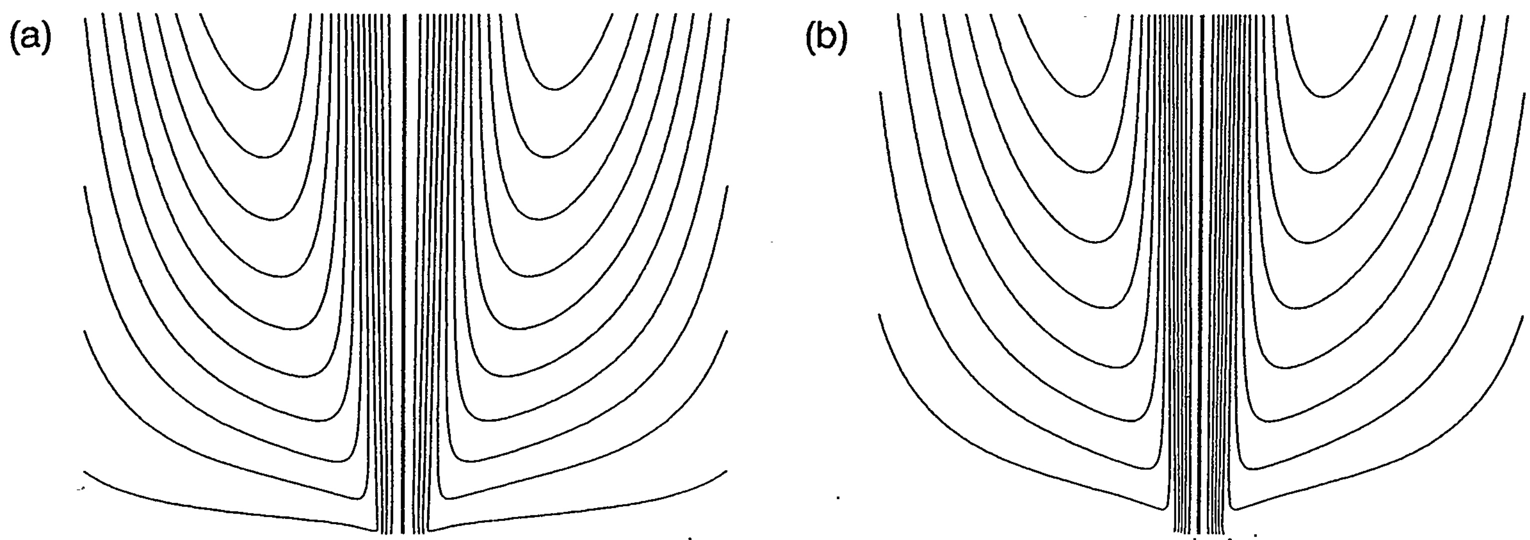

Figure 5.2 : Streamlines for steady jet. (a) Re_0 = 100, Profile III (eq. 4.42).
(b) Re_0 = 200, Profile III (eq. 4.42).

influx in the medium which extends to infinity along the r-direction (Schlichting, 1933, Zauner 1985). This is because of the solid wall located for convenience at a radial distance of 10 nozzle diameters from the axis in the computational procedure. The streamlines suggest that re-circulation is occurring in the ambient fluid. Streamlines, however, indicate only orientation of the velocity vectors. Velocities outside the jet were found to be much smaller (order of 10^{-3}) than along the axis. The walls are, therefore, not expected to influence significantly the dynamics of the jet itself. The streamlines at $Re_0 = 200$ are more closely spaced around the axis of the jet than at $Re_0 = 100$. At the two Re_0 used, the jet diameters down-stream are only slightly greater than the orifice diameter when the flow is laminar.

The calculated velocity profiles, non-dimensionalized with the centreline velocity at the orifice for the foregoing conditions are presented in Figure 5.3 and Figure 5.4. The velocity profile of a jet at Reynolds number 100 with a parabolic profile at the orifice (Figure 5.3a) decreases monotonically from the orifice. The corresponding velocity profile for a 10th power profile (Figure 5.3b) increases immediately after the orifice and then gradually decreases. Similar observations were made by Akaike and Nemoto (1989). The velocity profiles for $Re_0 = 200$ show similar trends.

The radial components of the velocity field for a steady jet at $Re_0 = 100$ and $Re_0 = 200$ are shown in Figure 5.5 and Figure 5.6. Positive radial velocities

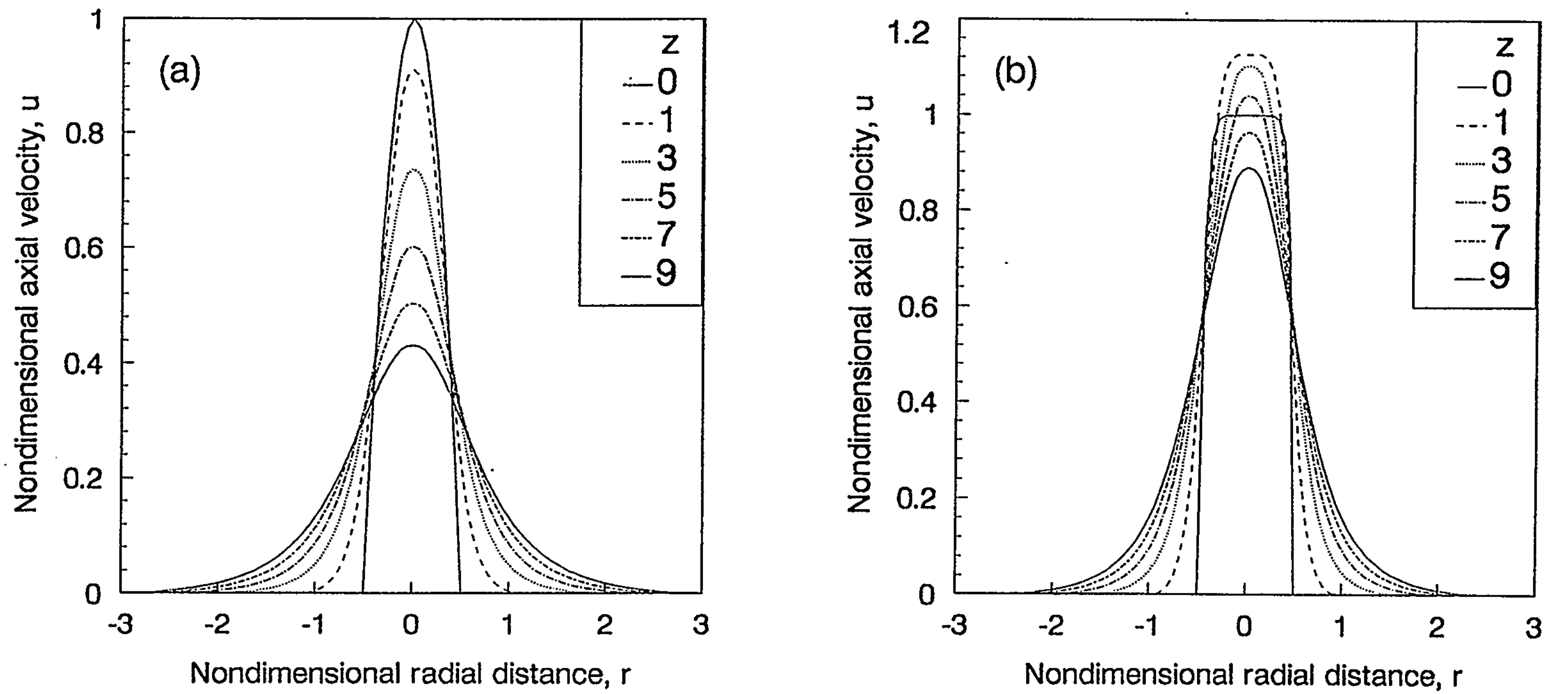

Figure 5.3 : Axial velocity profiles across the steady jet at Re_0 = 100.
(a) Profile I (eq. 4.40). (b) Profile III (eq. 4.42).

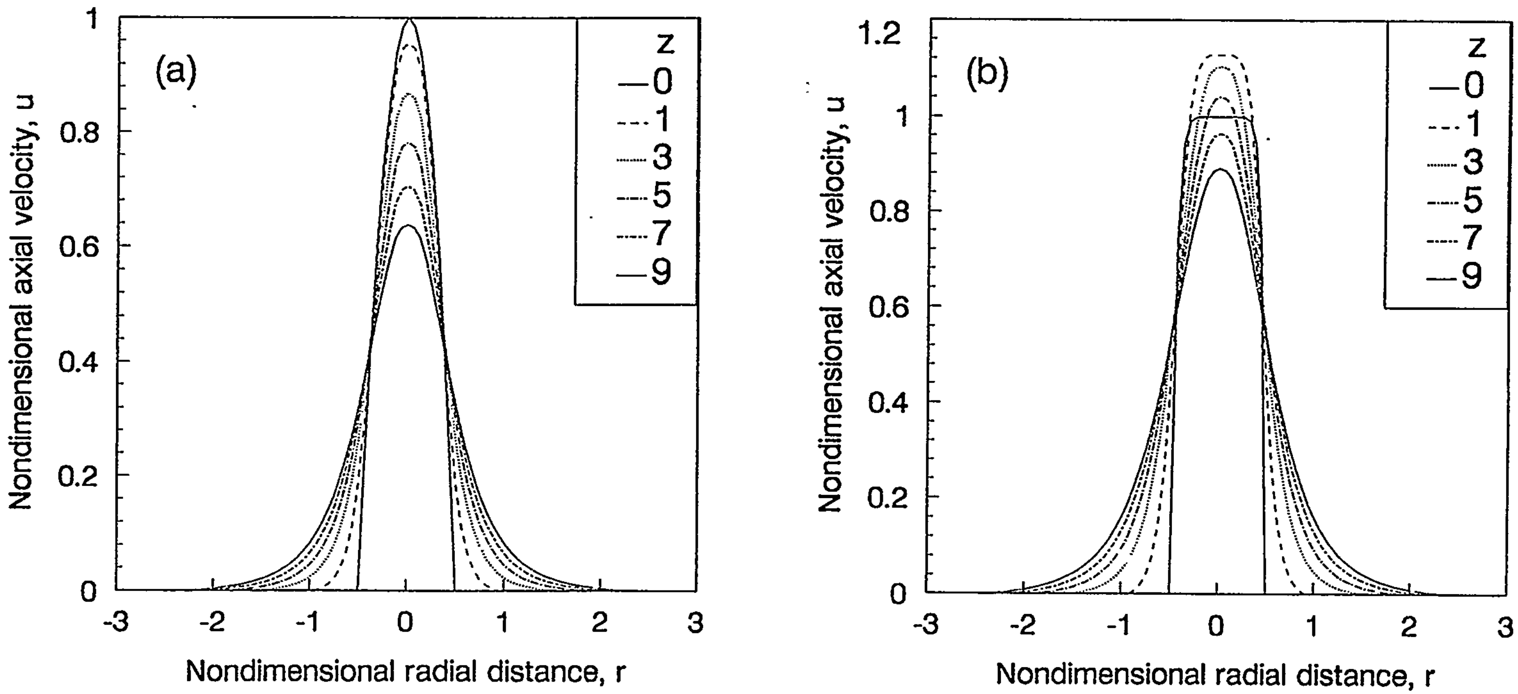

Figure 5.4 : Axial velocity profiles across the steady jet at $Re_0 = 200$.
(a) Profile I (eq. 4.40). (b) Profile III (eq. 4.42).

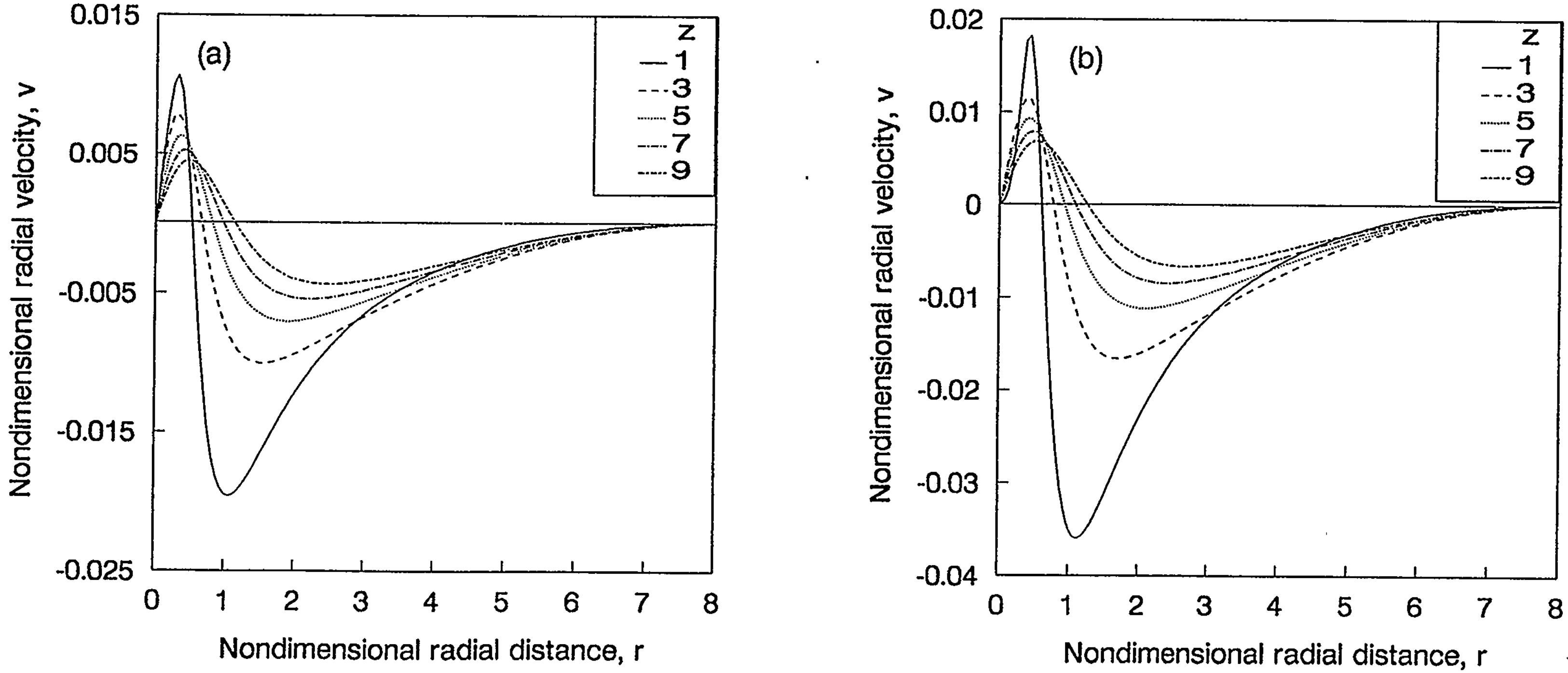

Figure 5.5 : Radial velocity profiles across the steady jet at $Re_0 = 100$.
(a) Profile I (eq. 4.40). (b) Profile III (eq. 4.42).

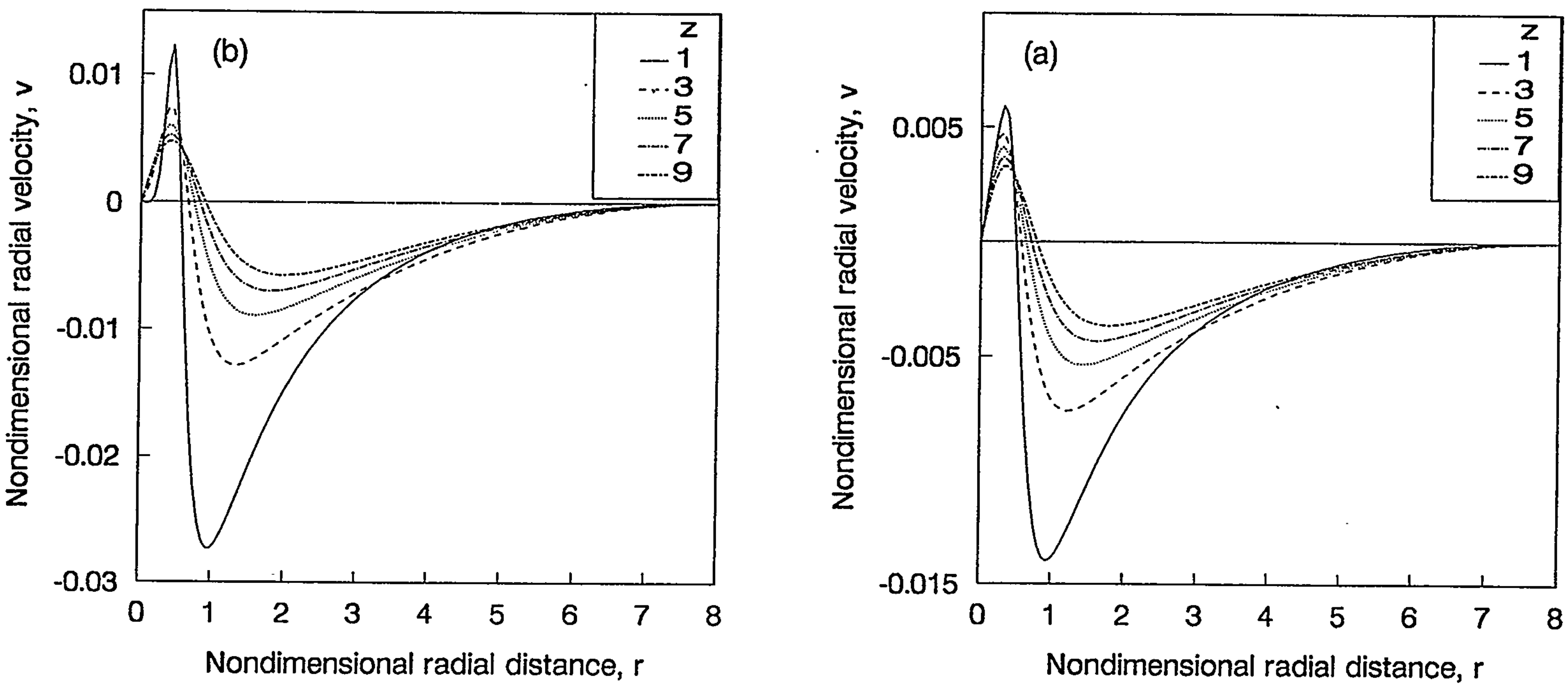

Figure 5.6 : Radial velocity profiles across the steady jet at $Re_0 = 200$.
(a) Profile I (eq. 4.40). (b) Profile III (eq. 4.42).

indicate flow outward from the jet axis and negative values indicate flow towards the jet axis. At any axial position, the radial velocity first increased from zero to a maximum, then decreased to a negative minimum and again slowly increased until it approached zero at the wall. If the "edge" of the jet corresponds to where the radial velocity is zero, the rates of spread may be determined from the data in Figures 5.5 and 5.6. The spread rates may be shown to depend on the velocity profile at the source and the Reynolds number. Another observation is that the side wall may have foreshortened the distance at which the radial velocity can be approximated to zero. Without the wall the velocity approaches zero asymptotically.

5.2 Pulsed Jets

The photographs and computed streakline and streamline plots for pulsed jets at different operating conditions are presented in Figure 5.7 to 5.41. The sequence for flow patterns over a complete cycle was reconstructed in each photographic sets. The results are presented in four different sections.

5.2.1 Low amplitude pulsations: $Re_0 \sim 100$, $\varepsilon = 10\%$, $0.5 \leq f^* \leq 2.5$ Hz

The experimentally observed and computed flow patterns of a jet at a constant Reynolds number ~ 100 and low amplitude ε of 10%, with varying frequencies are presented in Figures 5.7 to 5.16. The experimental flow patterns at a frequency of 0.5 Hz are shown in Figure 5.7. Slight but noticeable swellings were observed on the outline of the jet column. The swellings were symmetric close to the nozzle but became longitudinally asymmetric as they moved downstream. No internal structures were apparent. A slight surface perturbations were observed on the jet outline which probably were induced by mechanical devices in the apparatus. The perturbations decayed downstream from the orifice. The corresponding streakline plots computed with a 10th power profile at the orifice are shown in Figure 5.8. The first plot in the sequence corresponds to a time of 8 seconds from initiation of pulsation of the steady jet. This time was allowed so that the initial transient nature of the flow development could disappear. The figures are plotted at an interval of 0.2 second over one full cycle. Each figure is composed of three streaklines originating from three different locations. The outermost streaklines originated from a point adjacent to the rim of the orifice. A slight swelling of the jet outline was observed similar to that in experimental observations. The streaklines within the jet boundary showed the formation of a little skirt which was not prominent in the photographs. The swellings in the computation were found to be shorter than the experimentally observed ones.

As the frequency was increased to 1 Hz (Figure 5.9), thin sheets of ambient water were drawn into the solution of the jet downstream. The steep lateral gradient in the refractive index allowed it to be seen. Mixing by diffusion

Figure 5.7 : Sequence for pulsation cycles (a through f) reconstructed from still photographs taken at ~ 3 frames per second. $Re_0 = 102.7$, $f^* = 0.5$ Hz and $\varepsilon = 10\%$. The time interval between consecutive frames (ξ) are within 0.38 and 0.42 seconds.

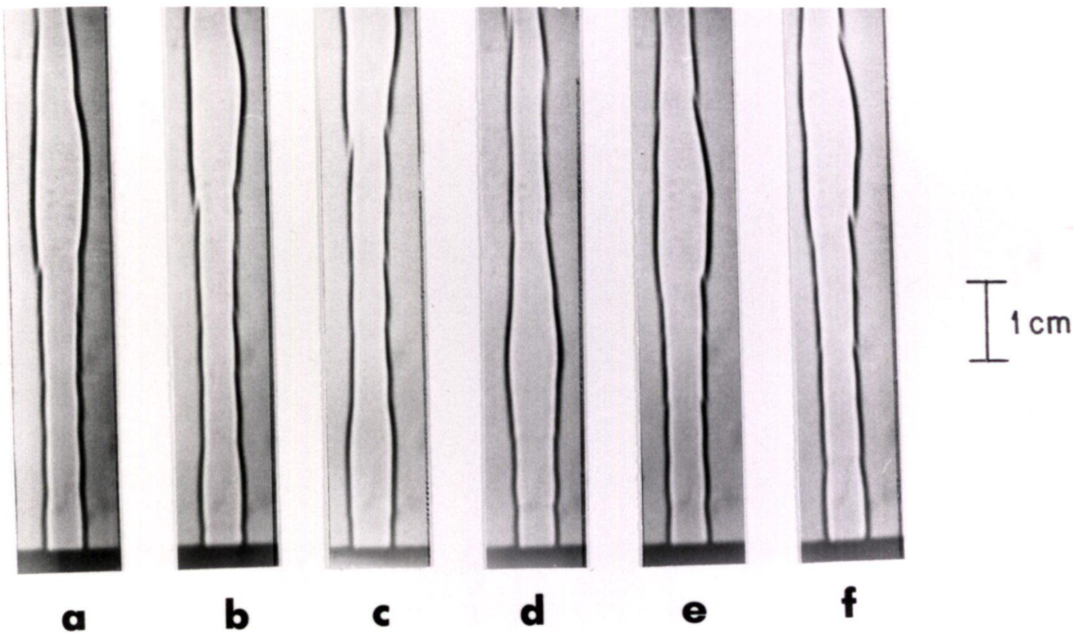
1 cm
a
b
c
d
e
f

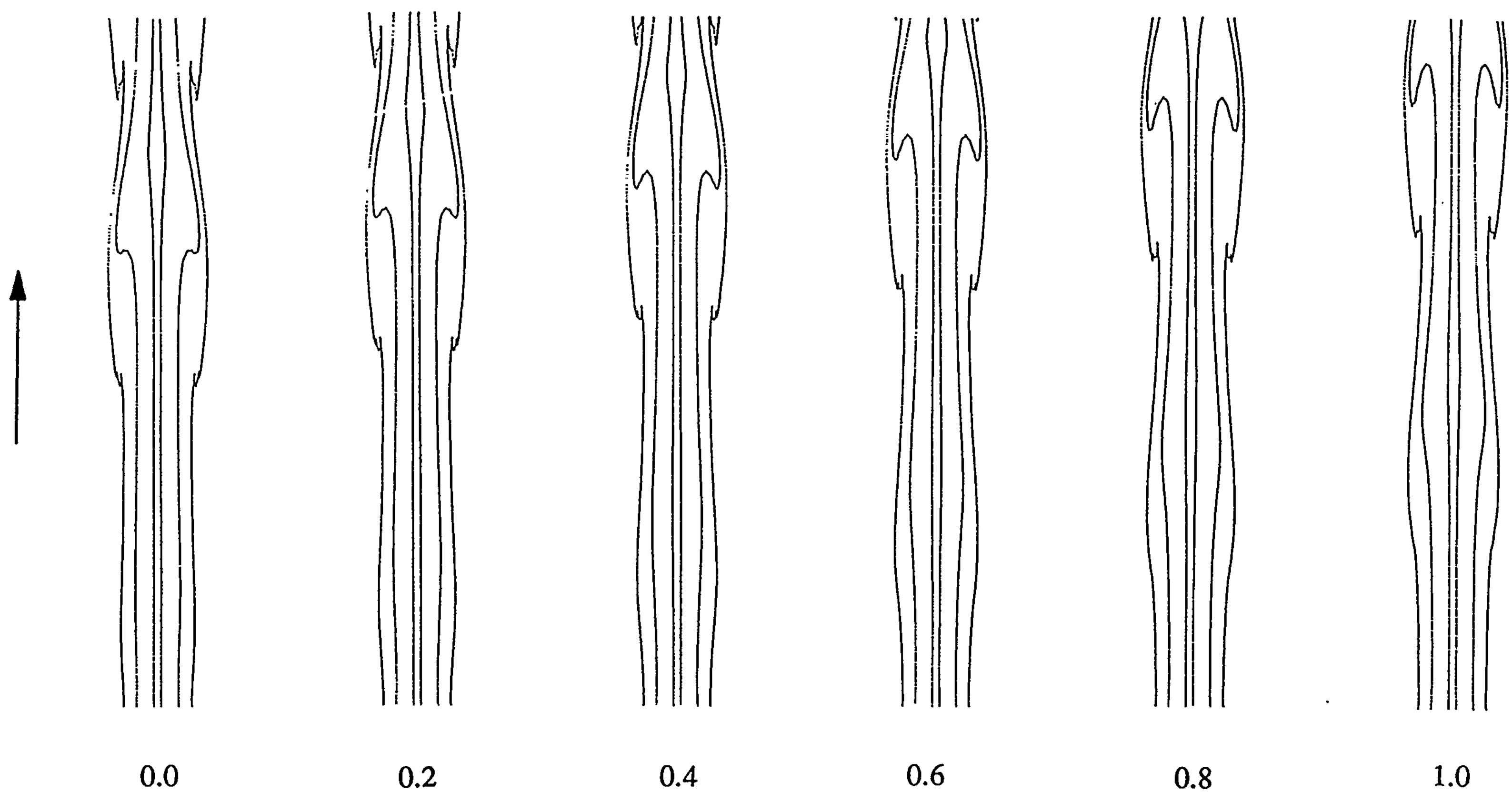

Figure 5.8 : Streaklines for pulsed laminar jets. $Re_0 = 100$, $f^* = 0.5$ Hz, $\varepsilon = 10\%$, Profile III (eq. 4.42). The first figure (0) corresponds to time (t_c) of 8 s from initiation of pulsation of a steady jet.

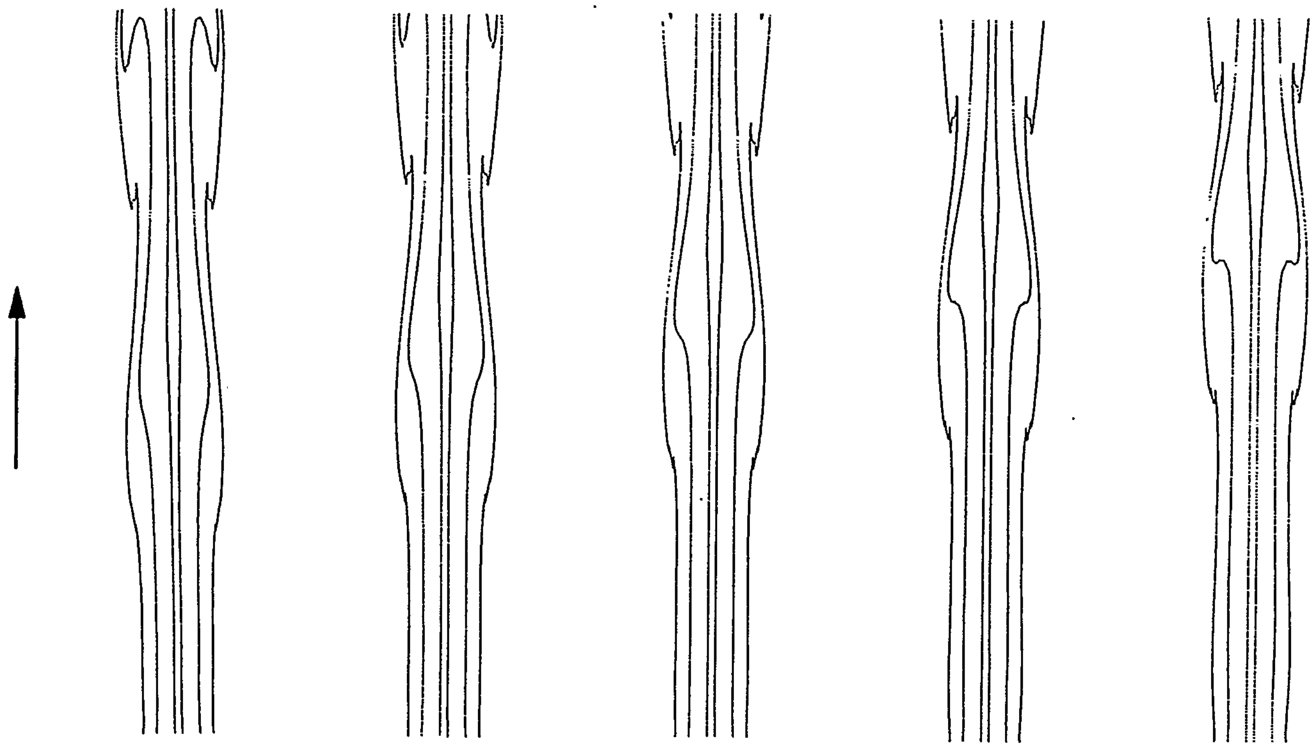

Figure 5.8 : continued

Figure 5.9 : Sequence of photographs for a pulsation cycle. $Re_0 = 102.7$, $f^* = 1$ Hz and $\varepsilon = 10\%$. $0.2 \leq \xi \leq 0.3$.

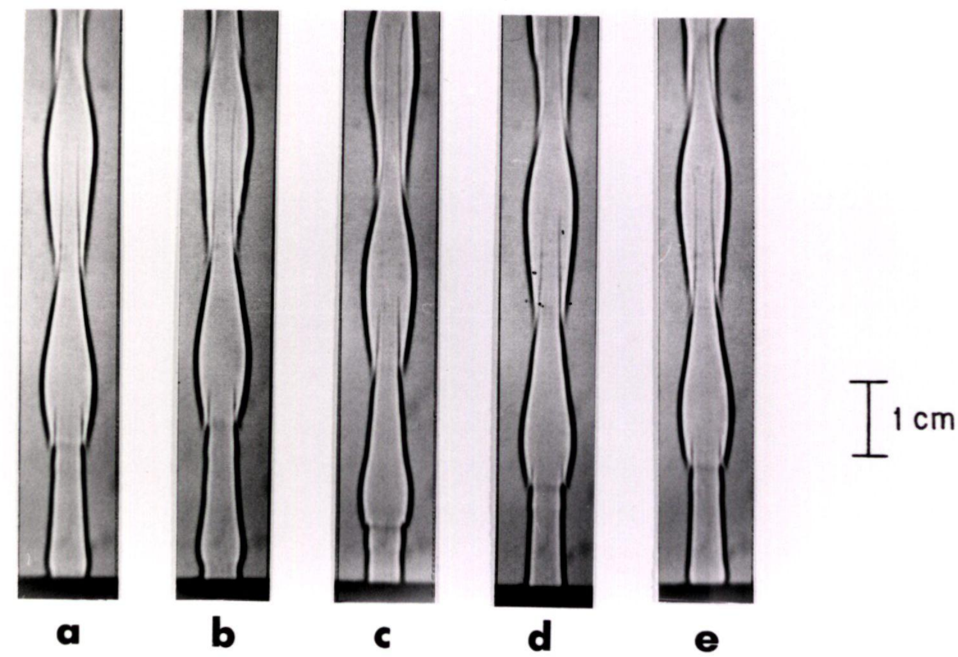
a
b
c
d
e
1 cm

must be relatively slow. Since, the sheets delineate the boundary of a core moving faster than its surroundings, such features will be termed as " core flow ". It is important to stress that this does not imply that the flow in the core is potential or irrotational. The central portion stretched axially as flow occurs downstream. The outline of the "entrained" but unmixed sheet abruptly ended without forming any sharp rim or edge and without curling significantly. The external outline of the jet showed alternate swelling and contraction.

In Figure 5.10 is presented the corresponding streakline plots. The velocity profile at the orifice is 10th power (Profile III, Equation 4.42). The outermost steakline penetrated into the jet column suggesting entrainment of sheets of the ambient fluid. A core flow was established similar to that observed in the experiment (Figure 5.9). The core elongated as it moved downstream. Close to the orifice alternate swelling and contraction were observed on the jet outline but the jet diameter became almost uniform downstream of the orifice. The length of the swellings was found to be shorter than the experimentally observed ones. To better reproduce experimental results, it may be necessary to change the velocity profile at the source into a form which would vary with time.

The streakline plots computed with a parabolic profile at the orifice (Profile I, Equation 4.40) are shown in Figure 5.11. The jet outline shows a slight undulation, but no penetration of the outermost streakline into the jet column is observable. Streaklines were also computed with a 6th power profile (Profile II,

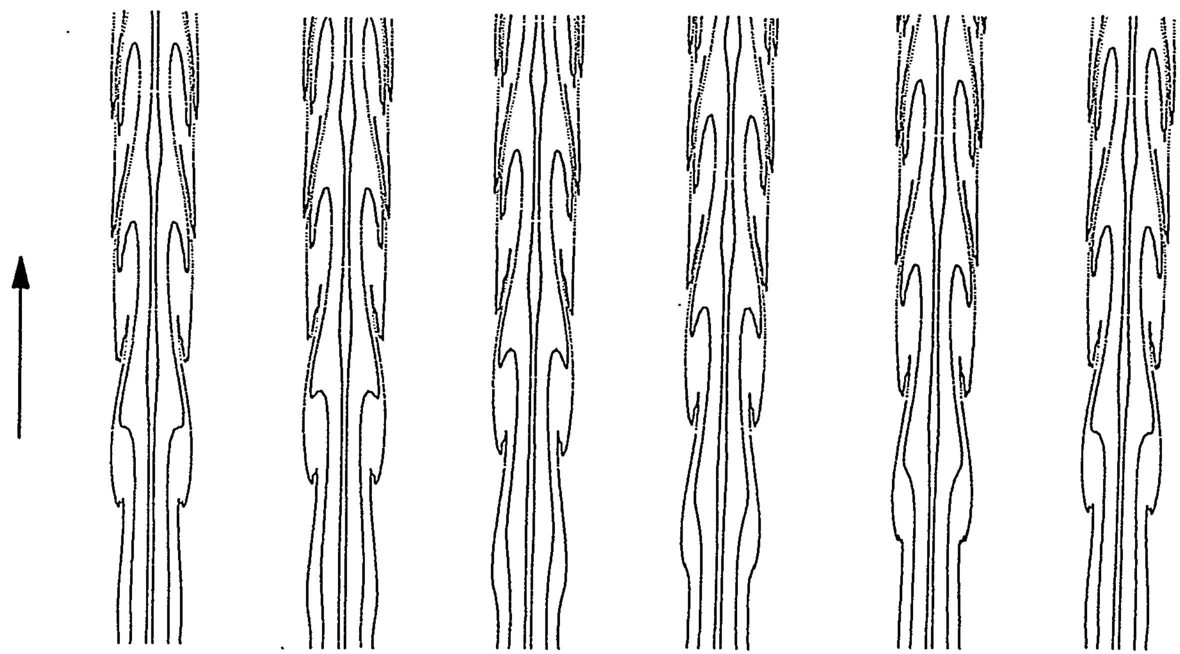

0.0 0.2 0.4 0.6 0.8 1.0

Figure 5.10 : Streaklines for pulsed laminar jets. $Re_0 = 100$, $f^* = 1$ Hz, $\varepsilon = 10\%$, Profile III (eq. 4.42), $t_c = 6$ s.

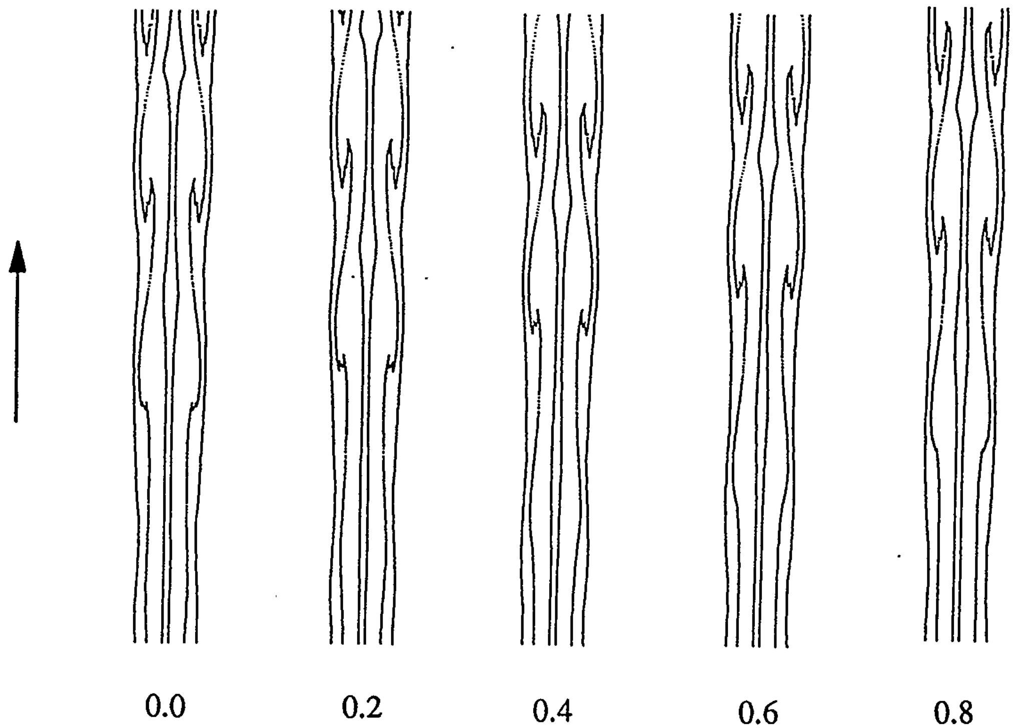

Figure 5.11 : Streaklines for pulsed laminar jets. $Re_0 = 100$, $f^* = 1$ Hz, $\varepsilon = 10\%$, Profile I (eq. 4.40), $t_c = 6$ s.

Equation 4.41), which is intermediate to the parabolic and a 10th power profile. The outline of the jet and the internal patterns (Figure 5.12) are similar but the ambient fluid has penetrated much less into the body of the jet than that with 10th power profile (Figure 5.10). That is, the streakline originating from the orifice rim shows less of an overlap in Figure 5.12 compared to that in Figure 5.10.

The streamlines for the same conditions are presented in Figure 5.13. The streamlines are instantaneous contours and show a wavy perturbation close to the orifice. The diameter of the streamtube confining the streamlines originating from the orifice remained almost uniform downstream of the orifice. This suggests that the jet spread was not very significant.

The photographic sequence for a pulsation cycle at $f^* = 1.7$ Hz is shown in Figure 5.14. The flow is very similar to that observed in Figure 5.9. The jet outline showed alternate swelling and contraction close to the nozzle. The core flow occupied a large portion of the jet's interior than for the conditions in Figure 5.9. The jet diameter was maintained almost uniform.

Streakline plots at a frequency of 2 Hz are shown in Figure 5.15. The cores appeared to cascade with each other and stabilize the downstream flow. The jet diameter became almost uniform after about 3 nozzle diameters from the orifice.

The photographic sequence of flow patterns at a frequency of 2.4 Hz is shown in Figure 5.16. Here, the core ends show distinct rims. The cores axially stretched, cascaded with each other and stabilized the downstream flow. The

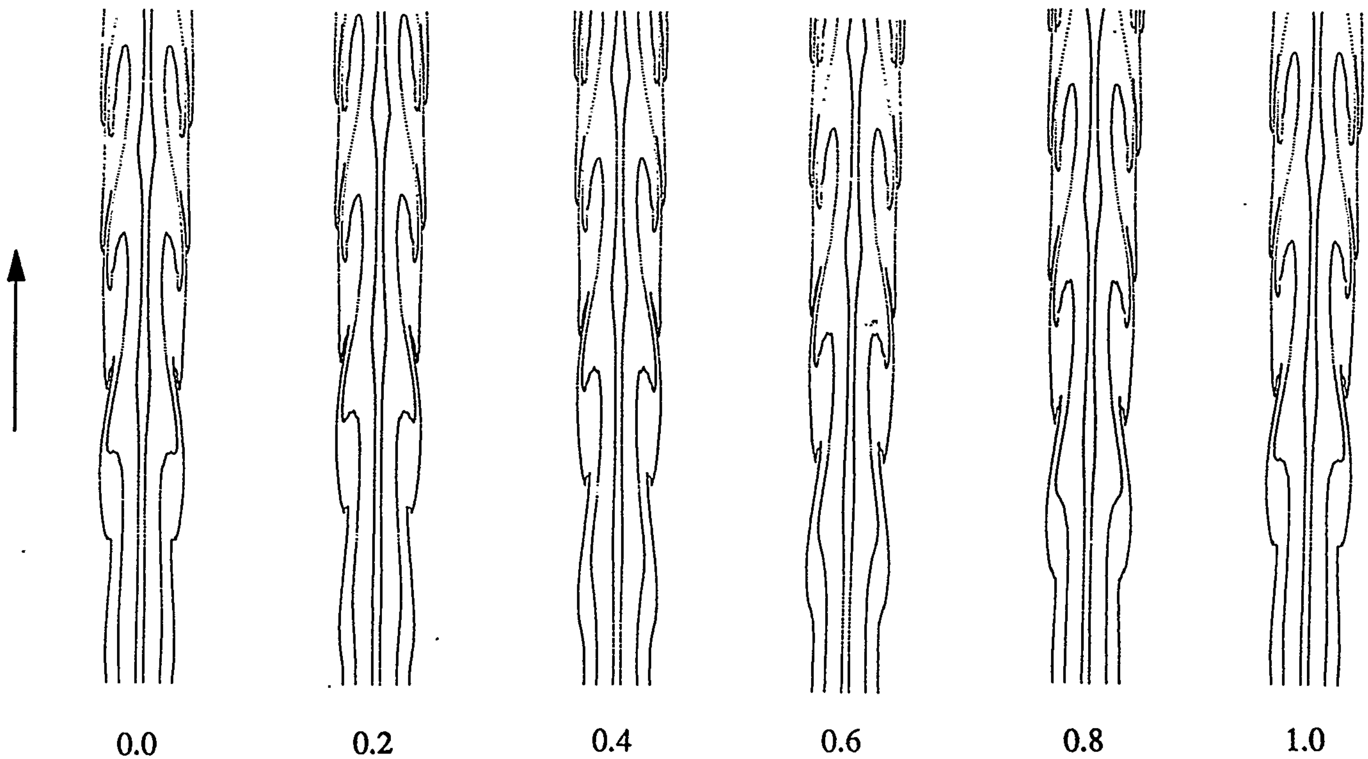

Figure 5.12 : Streaklines for pulsed laminar jets. $Re_0 = 100$, $f^* = 1$ Hz, $\varepsilon = 10\%$, Profile II (eq. 4.41), $t_c = 7.02$ s.

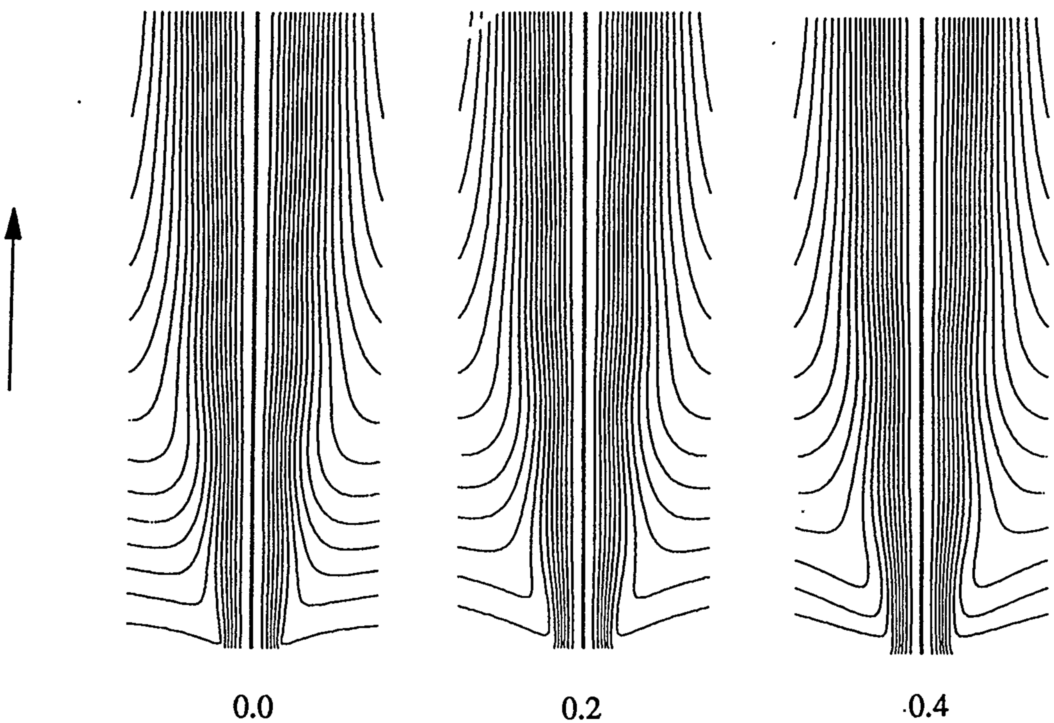

Figure 5.13 : Streamlines for pulsed laminar jets. $Re_0 = 100$, $f^* = 1$ Hz, $\varepsilon = 10\%$, Profile III (eq. 4.42), $t_c = 6$ s.

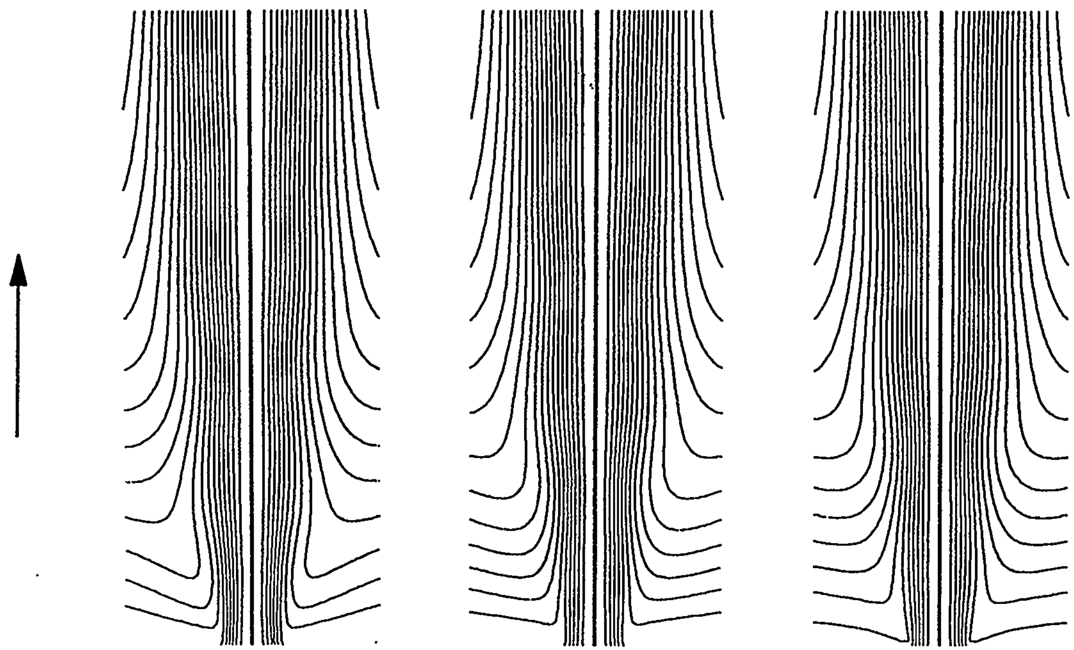

0.6 0.8 1.0

Figure 5.13 : continued

Figure 5.14 : Sequence of photographs for a pulsation cycle. $Re_0 = 102.7$, $f^* = 1.7$ Hz and $\varepsilon = 10\%$. $0.14 \leq \xi \leq 0.16$.

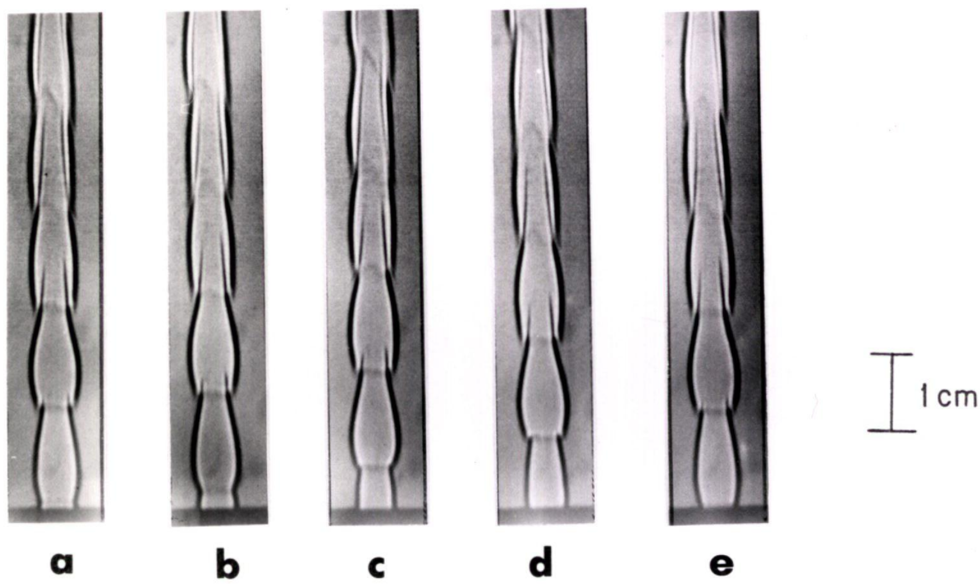
1 cm
a
b
c
d
e

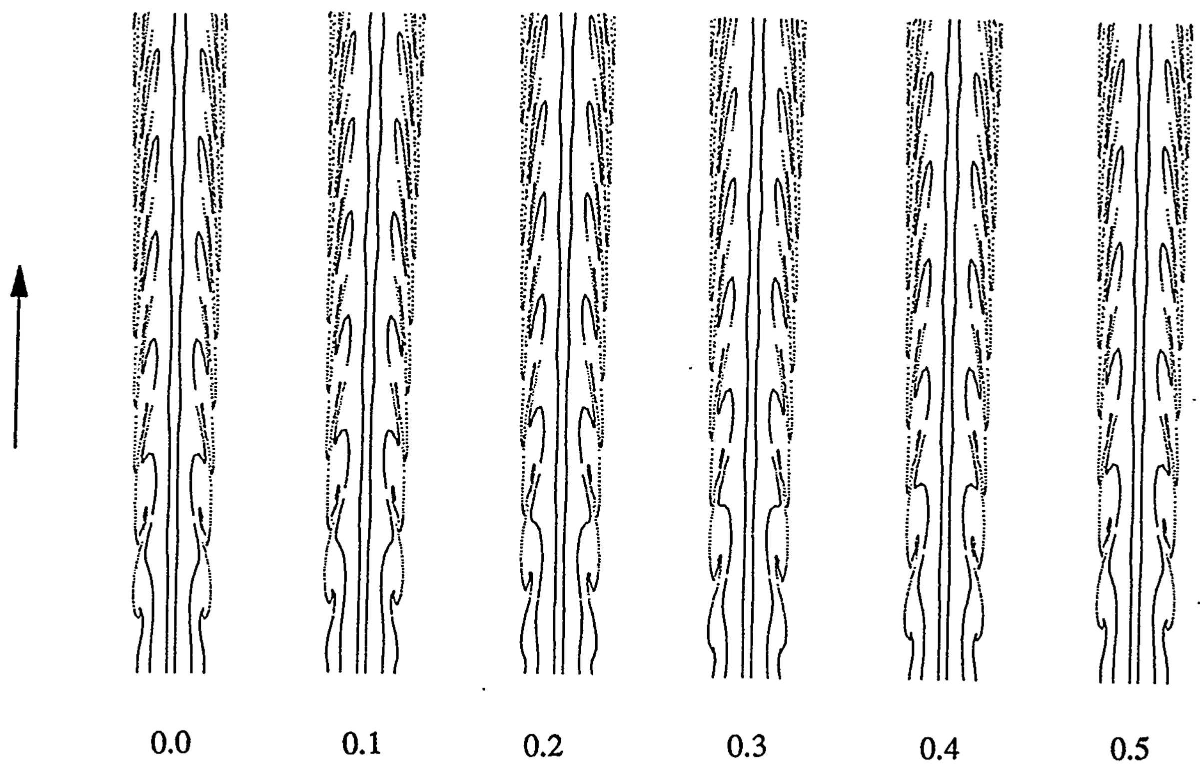

Figure 5.15 : Streaklines for pulsed laminar jets. $Re_0 = 100$, $f^* = 2$ Hz, $\varepsilon = 10\%$, Profile III (eq. 4.42), $t_c = 10$ s.

Figure 5.16 : Sequence of photographs for a pulsation cycle. $Re_0 = 102.7$, $f^* = 2.4$ Hz and $\varepsilon = 10\%$. $0.08 \leq \xi \leq 0.12$.

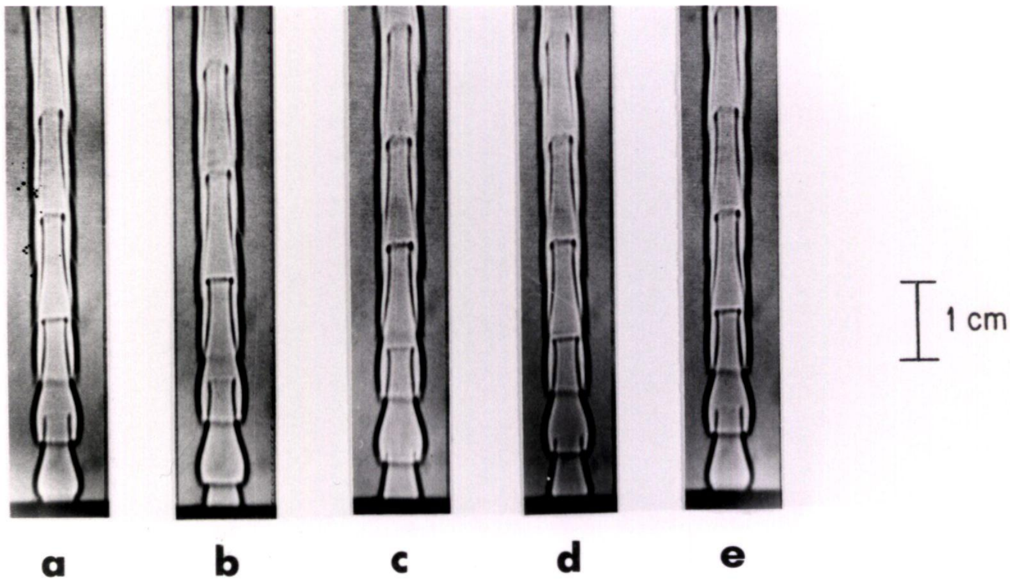
1 cm
a
b
c
d
e

diameter of the cores were comparable with the diameter of the jet. After about 3 nozzle diameter from the orifice, the jet diameter became almost uniform.

5.2.2 Intermediate amplitude pulsation; $Re_0 \sim 100$, $\varepsilon = 50\%$, $1.25 \leq f^* \leq 2.5$ Hz

The flow patterns of jets at a constant Reynolds number of ~ 100 and moderate amplitude ε of 50% with varying frequency $1.25 \leq f^* \leq 2.5$ Hz are presented in Figure 5.17 to 5.24. Figure 5.17 is the photographic sequence for a pulsation cycle at a frequency of 1.25 Hz which showed curling of drawn sheets of water within swellings. At the beginning of the cycle, a radially enlarging bulb grew at the orifice (a-b-c of Figure 5.17). As the swelling was detached from the orifice (similar in respects to the growth and release of bubbles at orifices) and moved downstream, a sheet of ambient water was entrained into the core. It is this entrained water which makes visible the spiral structures (in the Schlieren optics) as they develop into spirals during transport downstream. The distance between the centres of the swellings remained almost constant to suggest a steady rate of convection and a negligible rate of axial dispersion. The vortical motions are separate, i.e. not cascaded.

Streaklines for the above conditions, computed with the 10th power velocity profile at the orifice, are shown in Figure 5.18. The formation and initial development of the ring vortices are very similar to the experimentally observed

Figure 5.17 : Sequence of photographs for a pulsation cycle. $Re_0 = 102.7$, $f^* = 1.25$ Hz and $\varepsilon = 50\%$. $0.07 \leq \xi \leq 0.13$.

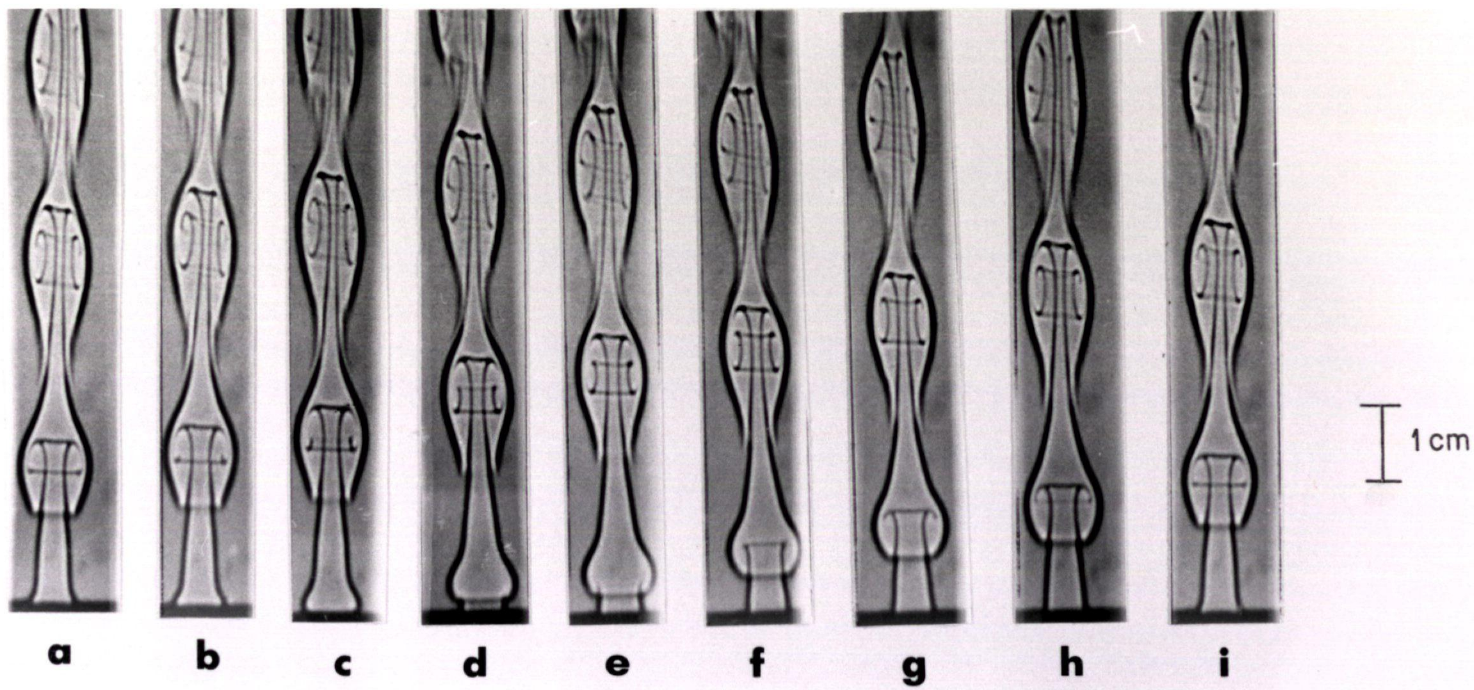
1 cm
a
b
c
d
e
f
g
h
i

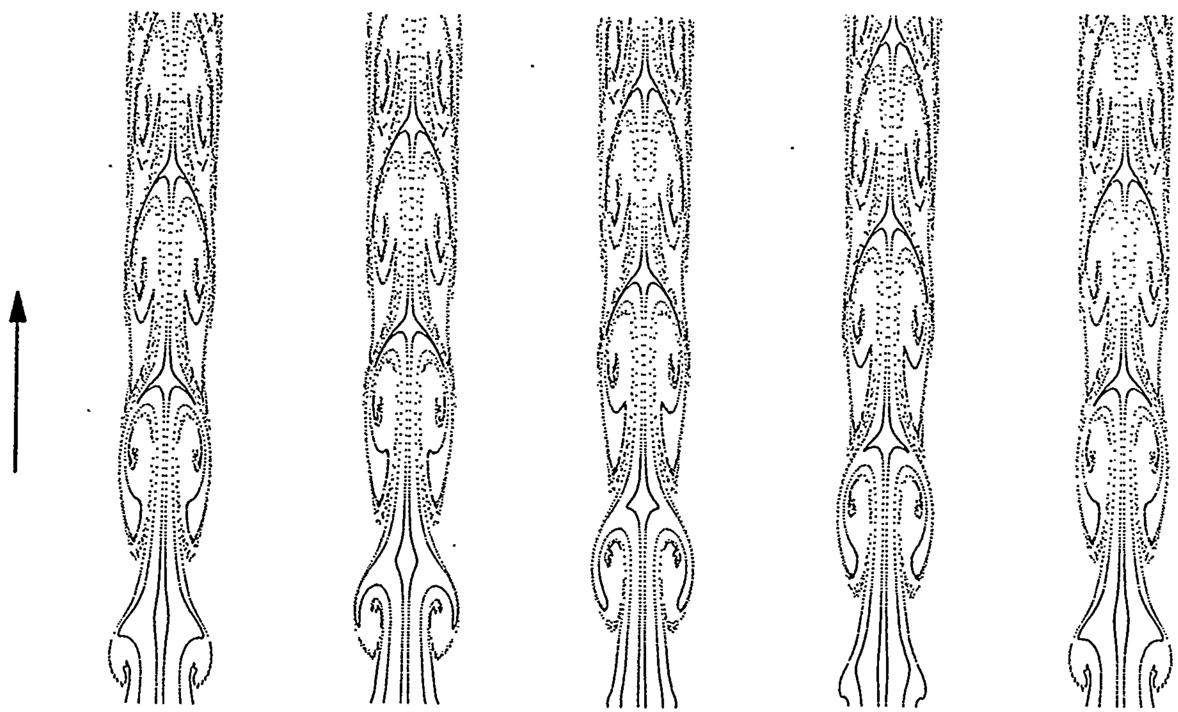

0.0 0.2 0.4 0.6 0.8

Figure 5.18 : Streaklines for pulsed laminar jets. $Re_0 = 100$, $f^* = 1.25$ Hz, $\varepsilon = 50\%$, Profile III (eq. 4.42), $t_c = 7.5$ s.

ones. The outermost streaklines predict the formation of a radially growing bulb at the orifice at the start of the formation of a ring vortex. As soon as the bulb detached from the orifice, the outermost streakline wrapped around and engulfed some ambient fluid. The entrapped fluid was apparently stretched into the spiral structure. The length of the segments which correspond to each pulse are found to be shorter than observed in the experiments. The streakline patterns for the same flow condition but with a sixth power profile at the orifice are shown in Figure 5.19. The flow patterns are similar to those with the tenth power profile but the circulation inside the vortices appeared to be a little weaker. Streaklines were also computed and plotted with a parabolic profile at the orifice (Figure 5.20). The outermost streaklines do not show any involution. Only a core flow is observed. These variations reinforce the idea that knowledge of the profiles at the source is essential if experimental results are to be predicted exactly.

The sequence of photographs at a frequency of 2.5 Hz are shown in Figure 5.21. The vortices stretched axially and cascaded with each other. The spiralling flow remained confined within an annular layer between the edge and the central core of the jet. The jet diameter became almost uniform after about five nozzle diameter from the orifice. The corresponding streaklines computed with a tenth power profile at the orifice are shown in Figure 5.22. The stretching and cascading of vortices leading to the stabilized downstream flow were predicted by the streaklines. However, the cascading of vortices was much exaggerated in the

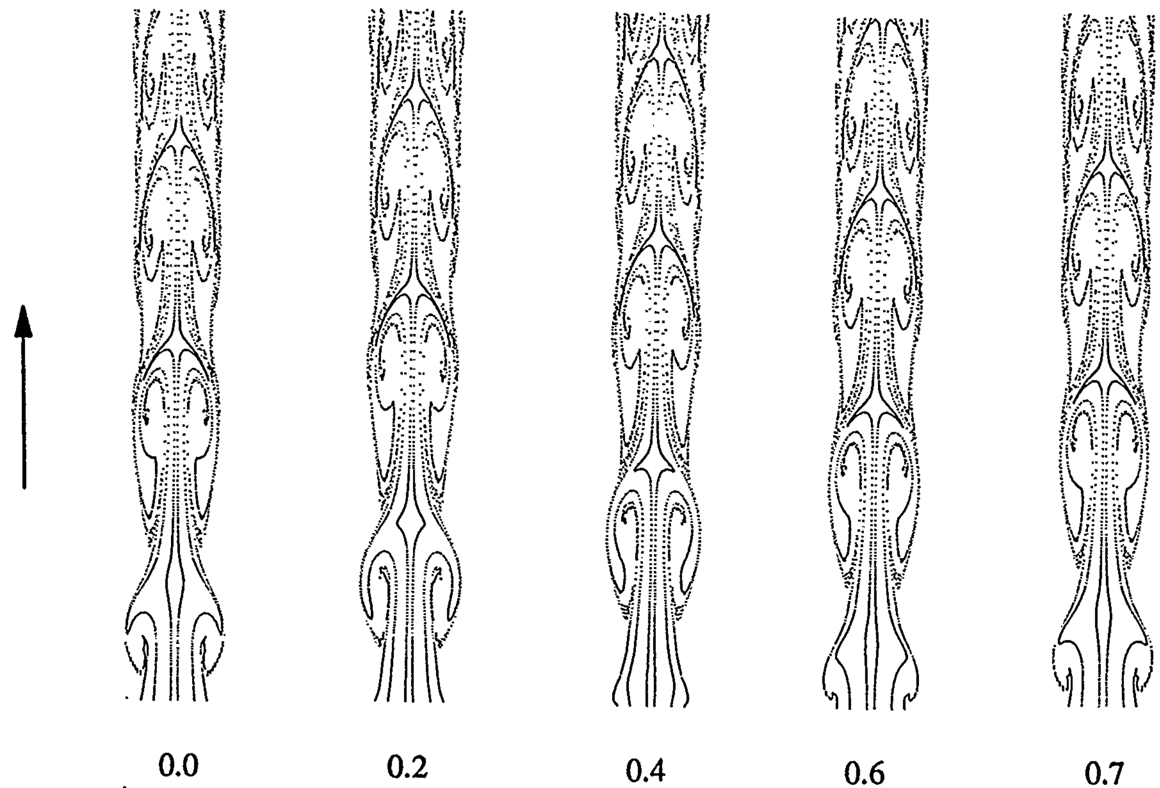

Figure 5.19 : Streaklines for pulsed laminar jets. $Re_0 = 100$, $f^* = 1.25$ Hz,
$\varepsilon = 50\%$, Profile II (eq. 4.41), $t_c = 7.59$ s.

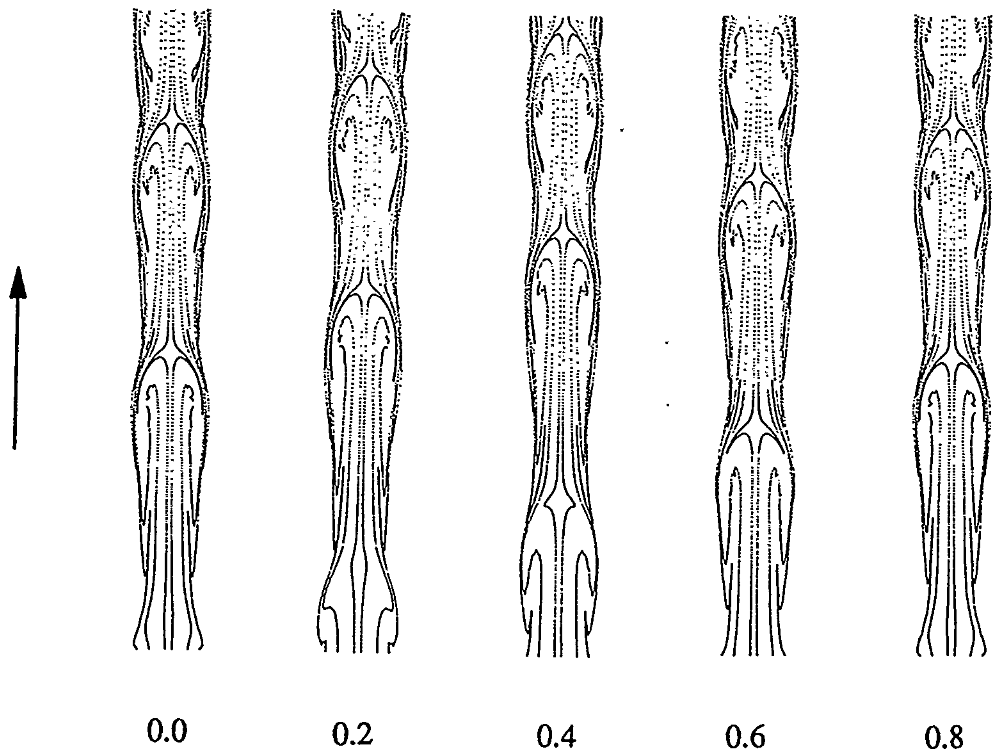

Figure 5.20 : Streaklines for pulsed laminar jets. $Re_0 = 100$, $f^* = 1.25$ Hz, $\varepsilon = 50\%$, Profile I (eq. 4.40), $t_c = 6.4$ s.

Figure 5.21 : Sequence of photographs for a pulsation cycle. $Re_0 = 102.7$, $f^* =$ 2.5 Hz and $\varepsilon = 50\%$. $0.06 \le \xi \le 0.09$.

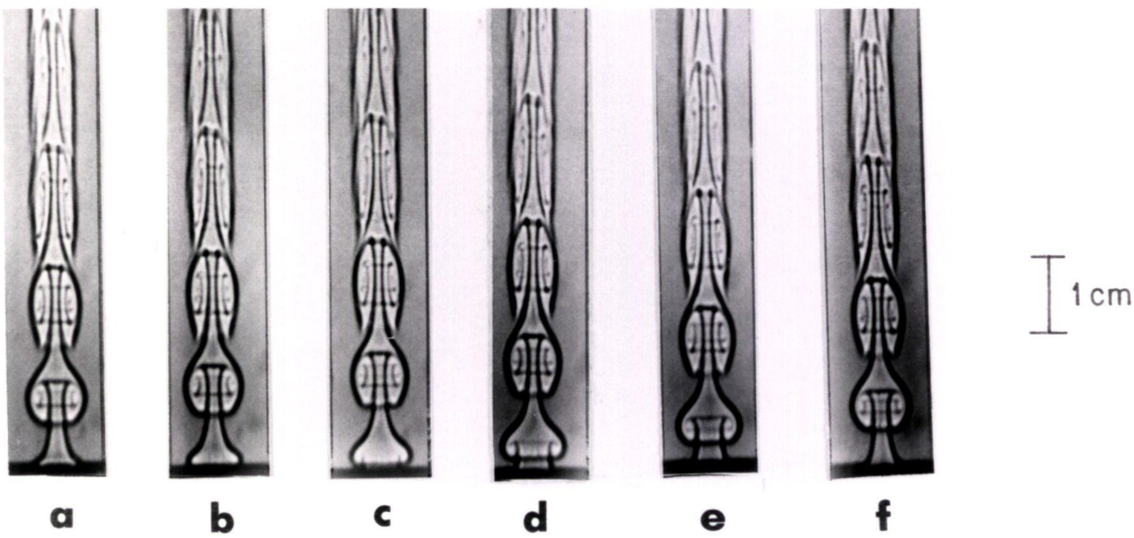
1 cm
a
b
c
d
e
f

0.0 0.1 0.20 0.3 0.4

Figure 5.22 : Streaklines for pulsed laminar jets. $Re_0 = 100$, $f^* = 2.5$ Hz, $\varepsilon = 50\%$, Profile III (eq. 4.42), $t_c = 8$ s.

computed flow patterns. The streaklines computed with a sixth power profile (Figure 5.23) appeared similar to those with the tenth power profile. But the stretching and cascading of vortices were a little weaker. Streaklines computed with parabolic profile at the orifice are shown in Figure 5.24. No spiralling or vortex motion was predicted. Only a core flow was observed. However, the cascading of the cores is very apparent.

5.2.3 High amplitude pulsation; $Re_0 \sim 100$, $\varepsilon = 100\%$, $0.5 \leq f^* \leq 2$ Hz

The flow patterns at a constant Reynolds number ~ 100, amplitude ε of 100% and frequency varying from 0.5 Hz to 2Hz are presented in Figure 5.25 to 5.31. The sequence of photographs of a pulsation cycle at $f^* = 0.5$ Hz is shown in Figure 5.25. The growth of a bulb and its lifting from the orifice plate occur over a short span (a-b-c of Figure 5.25) of time compared to the period of the pulsation (a-h). During the rest of the cycle the vortex is convected downstream with a continuous column of jet in the wake. That is, the flow was not interrupted. The vortex noticeably grew in size due to entrainment, and its ascent was progressively slowed down. These features are reasonably reproduced in the computed streakline plots (Figure 5.26). When the streamlines in Figure 5.27 are compared with the corresponding streakline plots, it is seen that the centre of closed streamlines is radially displaced from the centre of the ring vortices. The close but non-uniform spacing between streamlines suggest that vorticity might be

0.0 0.2 0.4 0.6

Figure 5.23 : Streaklines for pulsed laminar jets. $Re_0 = 100$, $f^* = 2.5$ Hz, $\varepsilon = 50\%$, Profile II (eq. 4.41), $t_c = 7.5$ s.

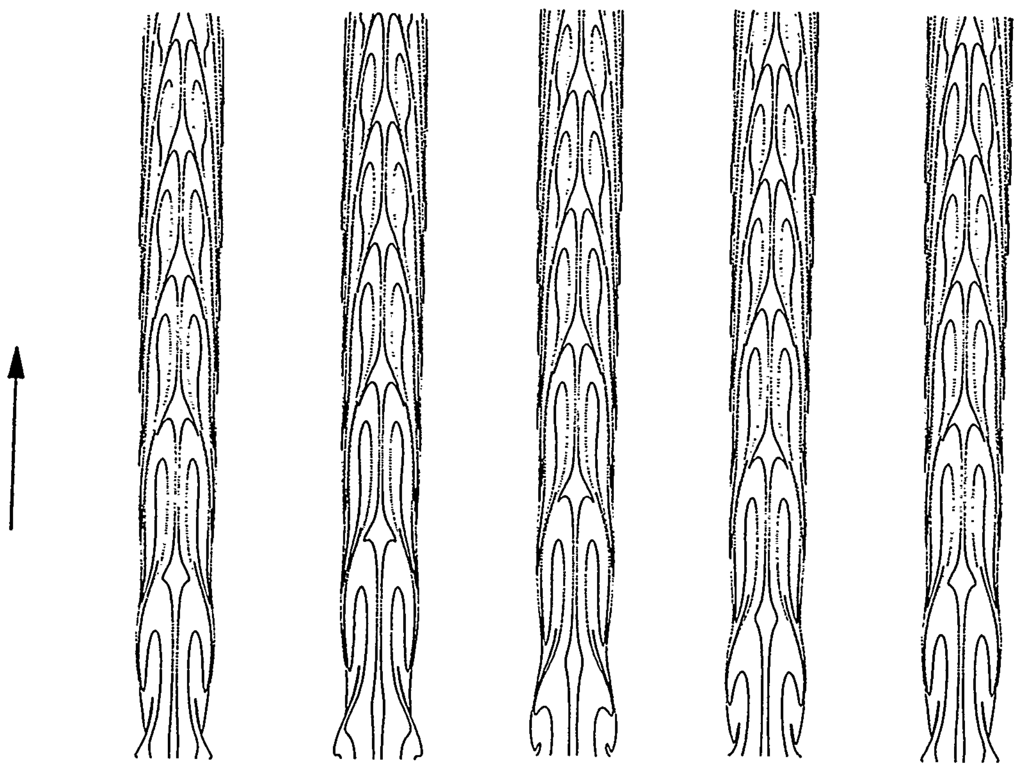

0.0 0.1 0.2 0.3 0.4

Figure 5.24 : Streaklines for pulsed laminar jets. $Re_0 = 100$, $f^* = 2.5$ Hz, $\varepsilon = 50\%$, Profile I (eq. 4.40), $t_c = 3.6$ s.

Figure 5.25 : Sequence of photographs for a pulsation cycle. $Re_0 = 102.7$, $f^* = 0.5$ Hz and $\varepsilon = 100\%$. $0.28 \leq \xi \leq 0.32$.

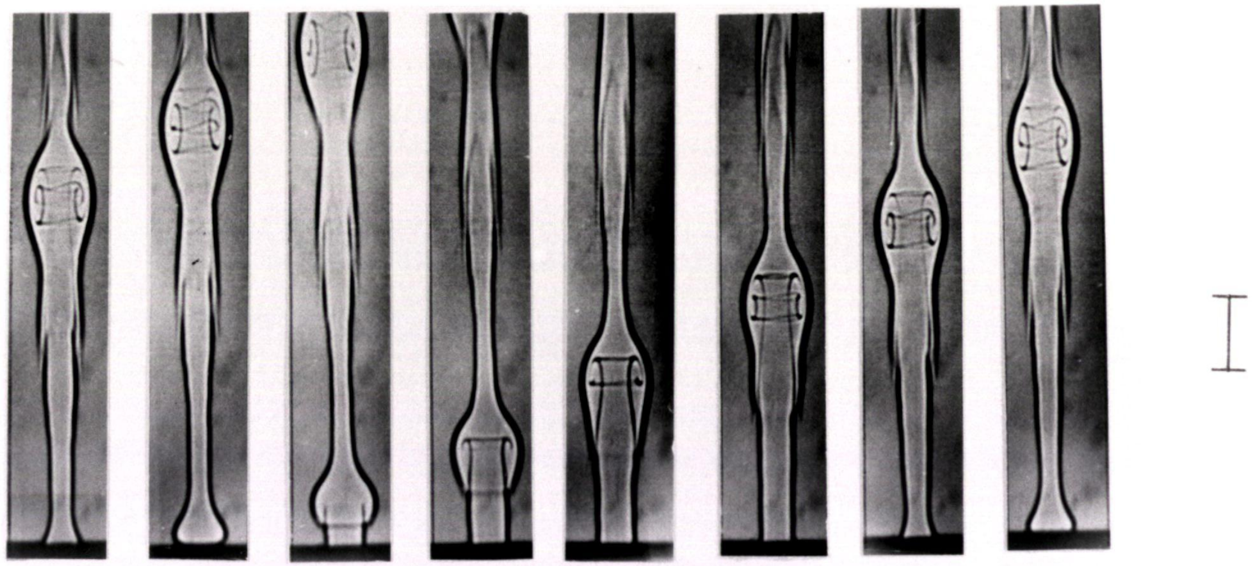

a b c d e f g h

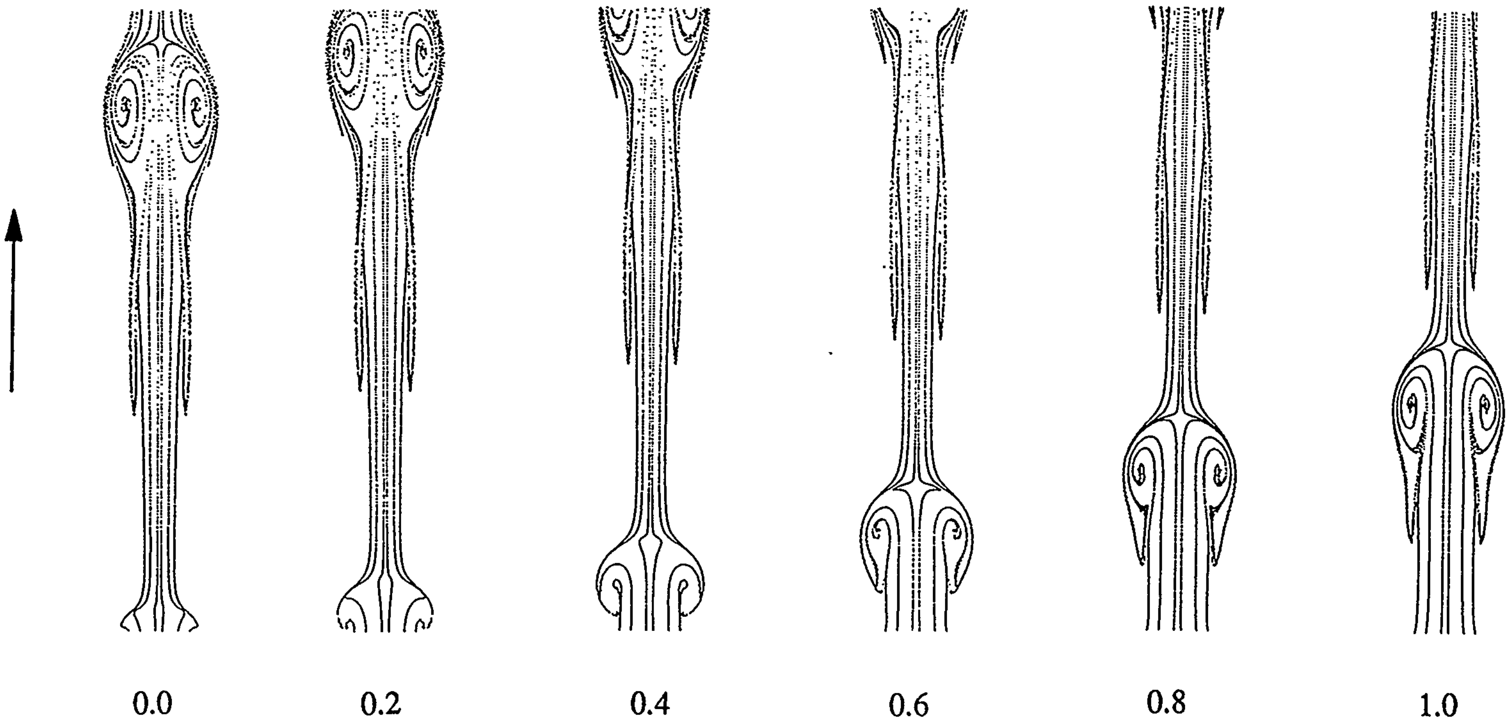

Figure 5.26 : Streaklines for pulsed laminar jets. $Re_0 = 100$, $f^* = 0.5$ Hz, $\varepsilon = 100\%$, Profile III (eq. 4.42), $t_c = 5.94$ s.

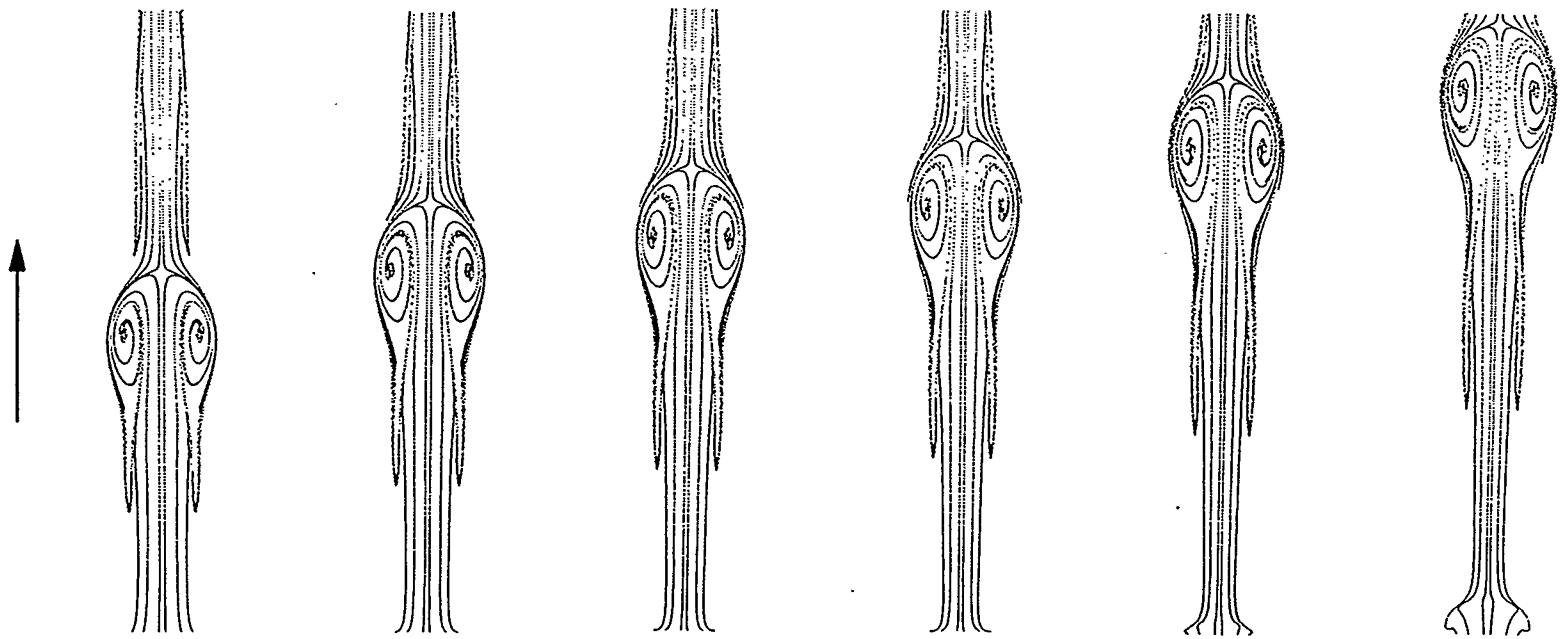

1.2 1.4 1.5 1.6 1.8 2.0

Figure 5.26 : continued

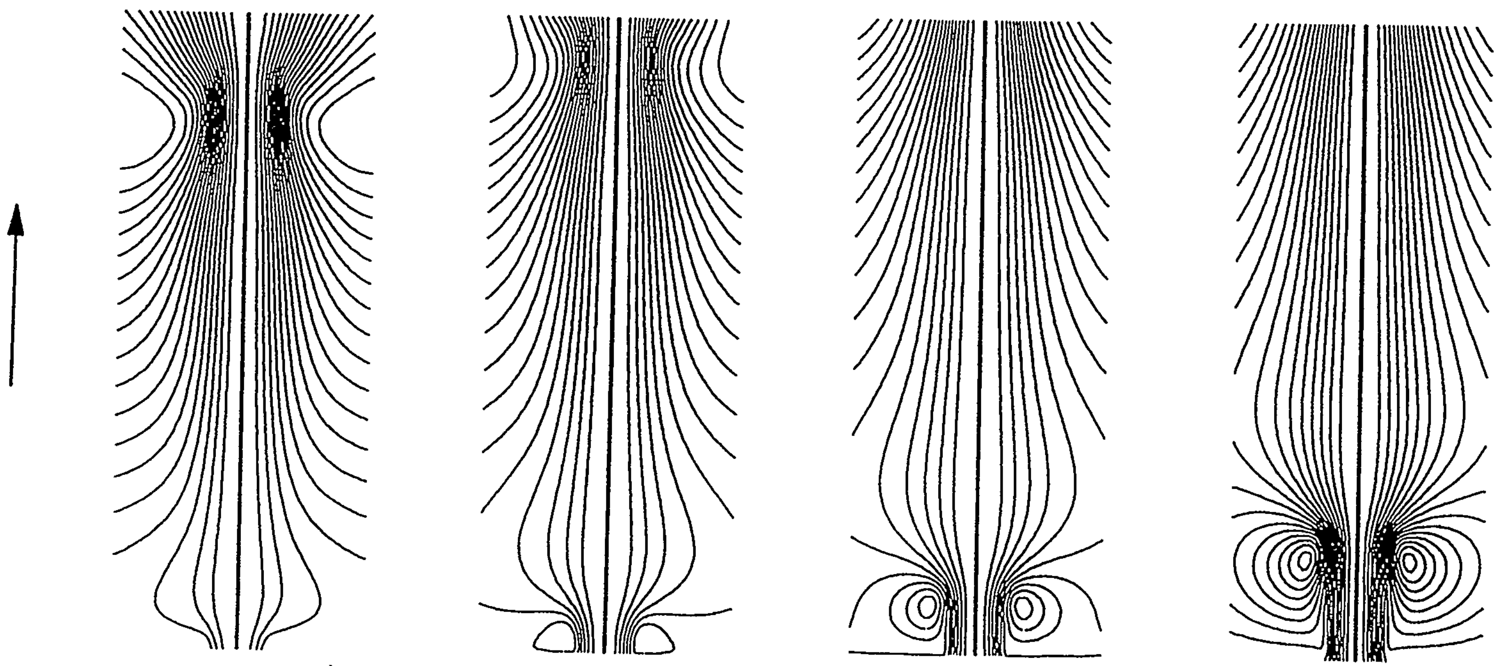

0.0 0.2 0.4 0.6

Figure 5.27 : Streamlines for pulsed laminar jets. $Re_0 = 100$, $f^* = 0.5$ Hz, $\varepsilon = 100\%$, Profile III (eq. 4.42), $t_c = 5.94$ s.

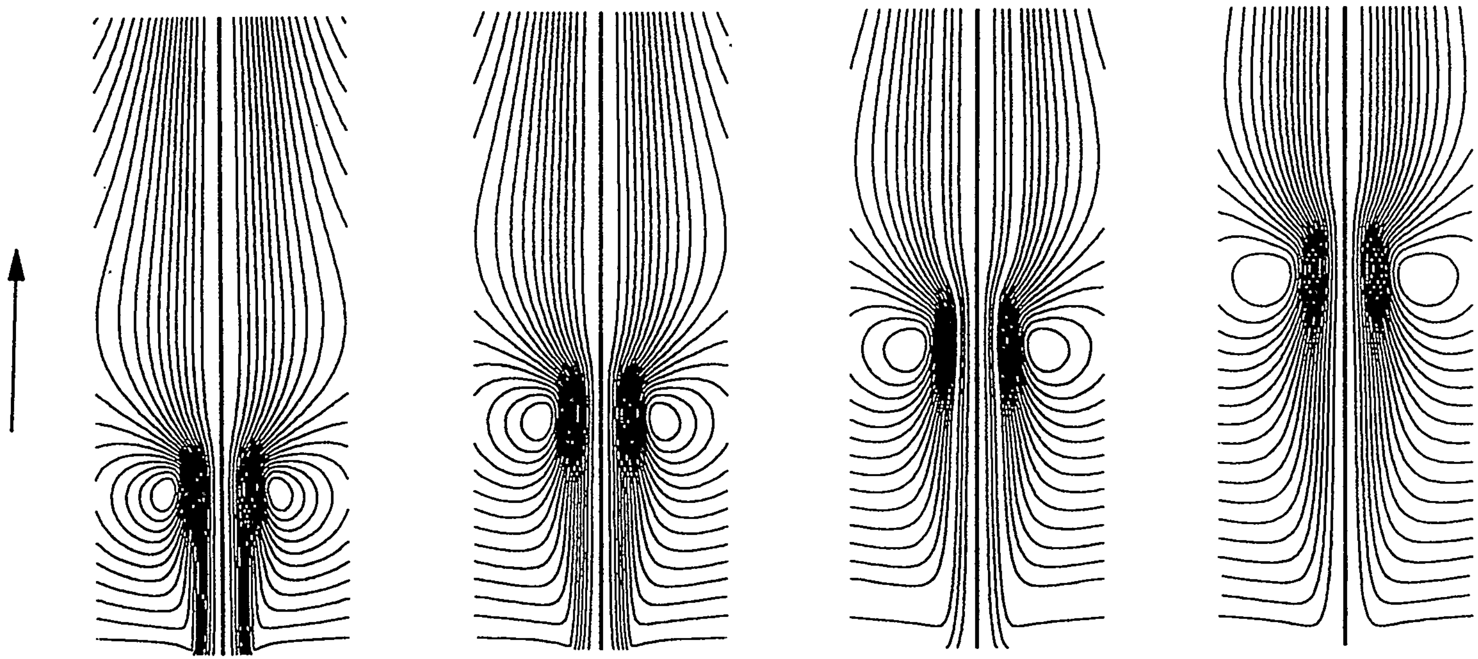

0.8 1.0 1.2 1.4

Figure 5.27 : continued

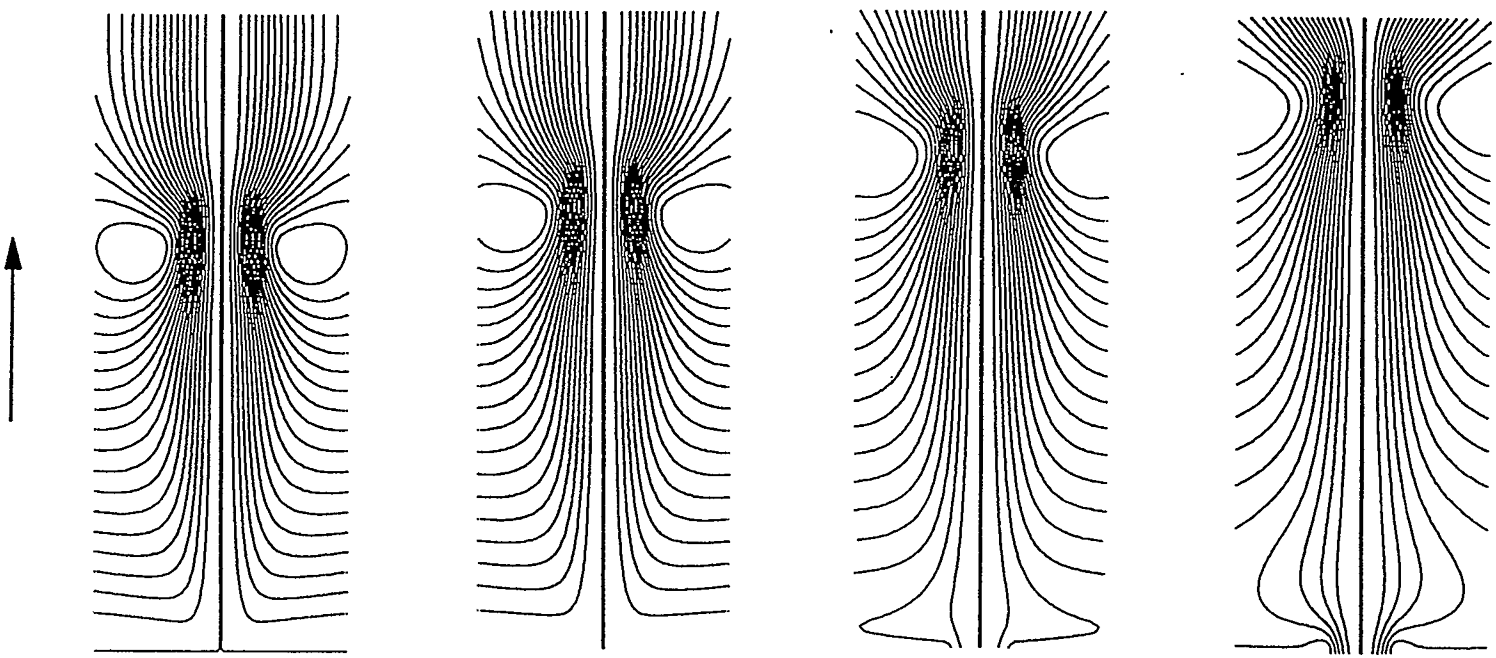

1.5 1.6 1.8 2.0

Figure 5.27 : continued

highly concentrated in this region even though the streamlines are not closed. The closed loops are in the flow region external to the jet. This indicates that the domain is rotational.

The streaklines at the same condition (Re_0=100, f^*=0.5 Hz, ε=100%) but with a parabolic velocity profile at the orifice are shown in Figure 5.28. Although the streakline immediately next to the outermost streakline and inside the jet involutes and gives appearance of a vortex, the outermost streakline does not show any involution. This may be due to the fact that for the parabolic profile at the orifice, the velocity gradient and hence the vorticity at the edge of the nozzle is much lower than that for the tenth power profile (see Figure 4.42).

Streakline patterns for the jet (Re_0=100, ε=100%) at f^* = 1Hz are shown in Figure 5.29. The initial velocity profile is 10th power. The formation and shape of the individual vortices and their wakes are again similar to that at f^* = 0.5 Hz (Figure 5.26). The distance between successive vortices decreased downstream of the orifice which suggests that the vortices may be catching up with each other outside the computational domain.

The sequence of flow patterns of the jet (Re_0 ~ 100, ε = 100%) at a frequency of 2 Hz is shown in Figure 5.30. The flow is very similar to that observed in Figure 5.21 (Re_0 = 100, f^* = 2.5Hz, ε = 50%). The spiralling remains confined within an annular layer between the edge and the central core of the vortices. The vortices are stretched and cascade with each other. This behaviour

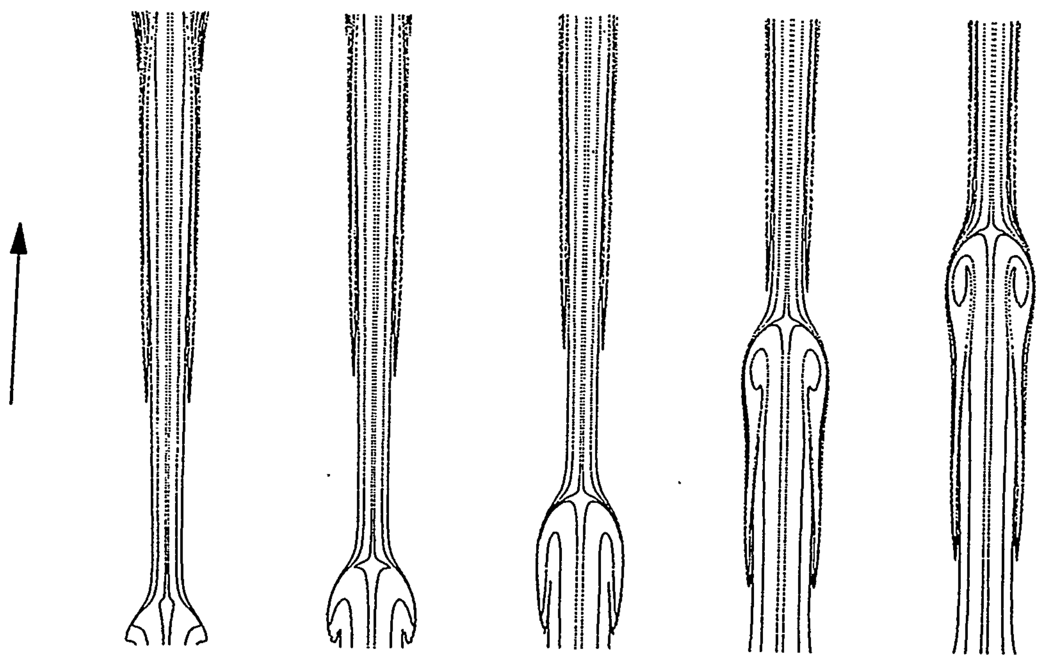

Figure 5.28 : Streaklines for pulsed laminar jets. Re_0 = 100, f^* = 0.5 Hz, ε = 100%, Profile I (eq. 4.40), t_c = 6.02 s.

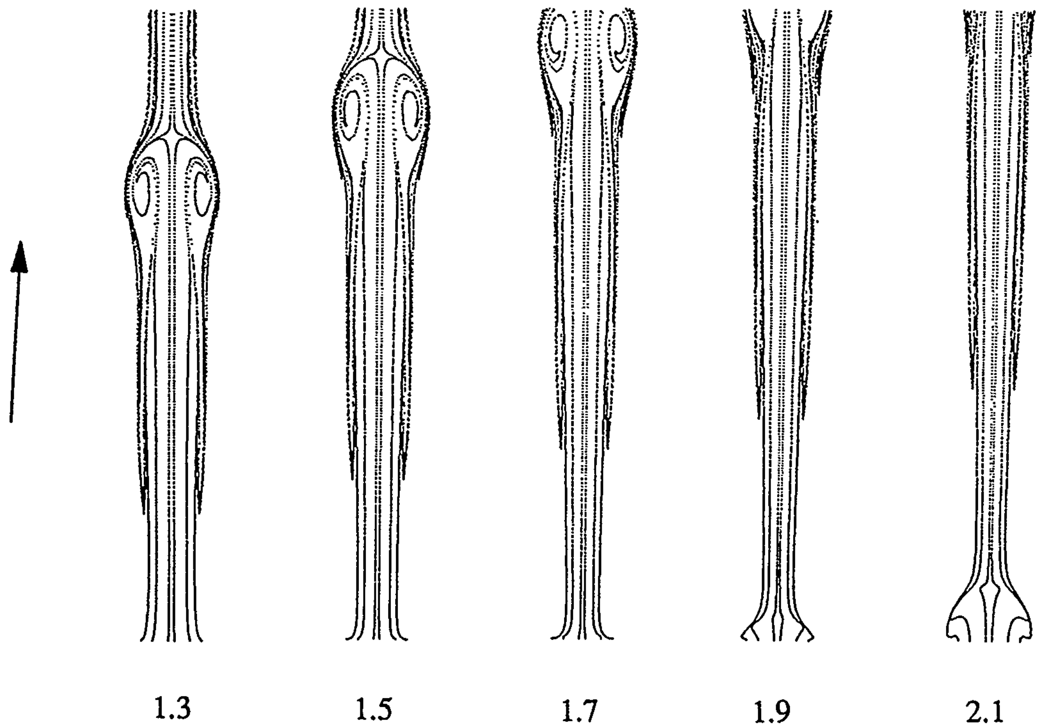

Figure 5.28 : continued

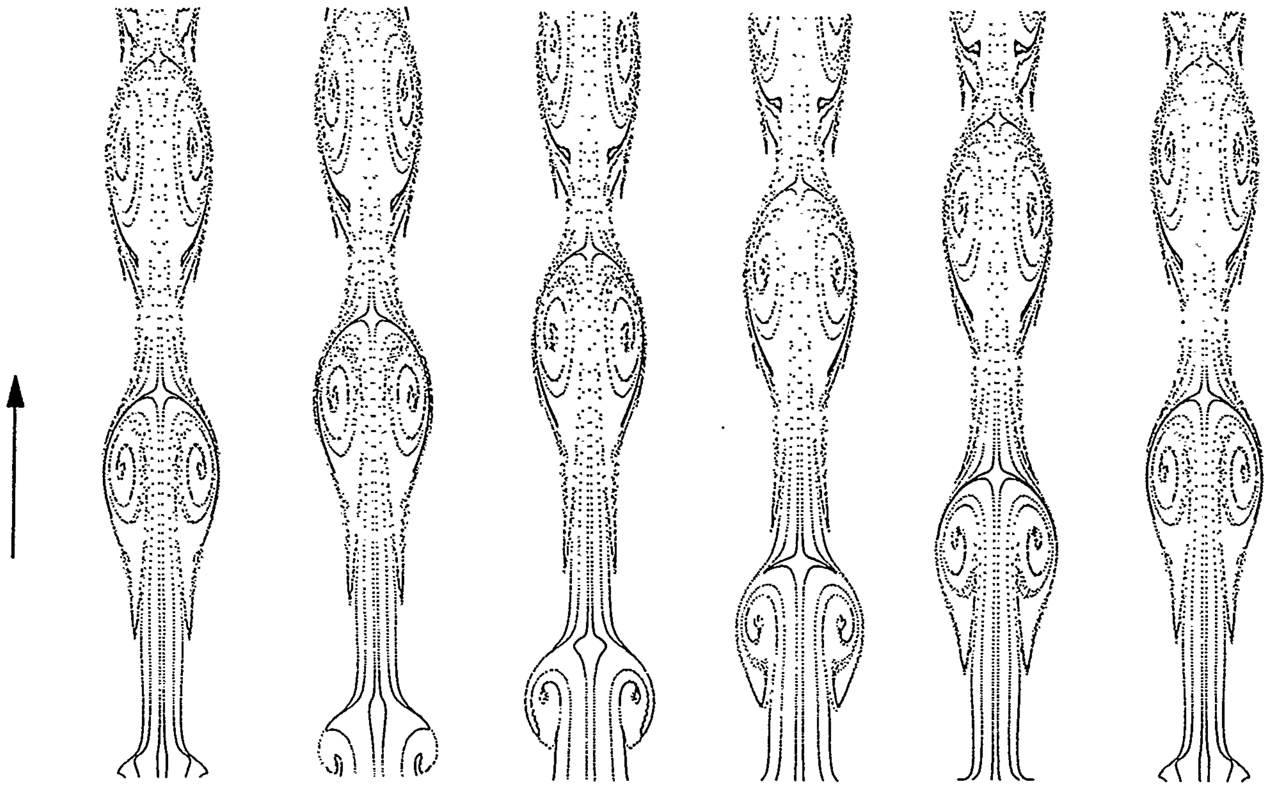

0.0 0.2 0.4 0.6 0.8 1.0

Figure 5.29 : Streaklines for pulsed laminar jets. $Re_0 = 100$, $f^* = 1$ Hz, $\varepsilon = 100\%$, Profile III (eq. 4.42), $t_c = 6$ s.

Figure 5.30 : Sequence of photographs for a pulsation cycle. $Re_0 = 102.7$, $f^* = 2$ Hz and $\varepsilon = 100\%$. $0.1 \leq \xi \leq 0.16$.

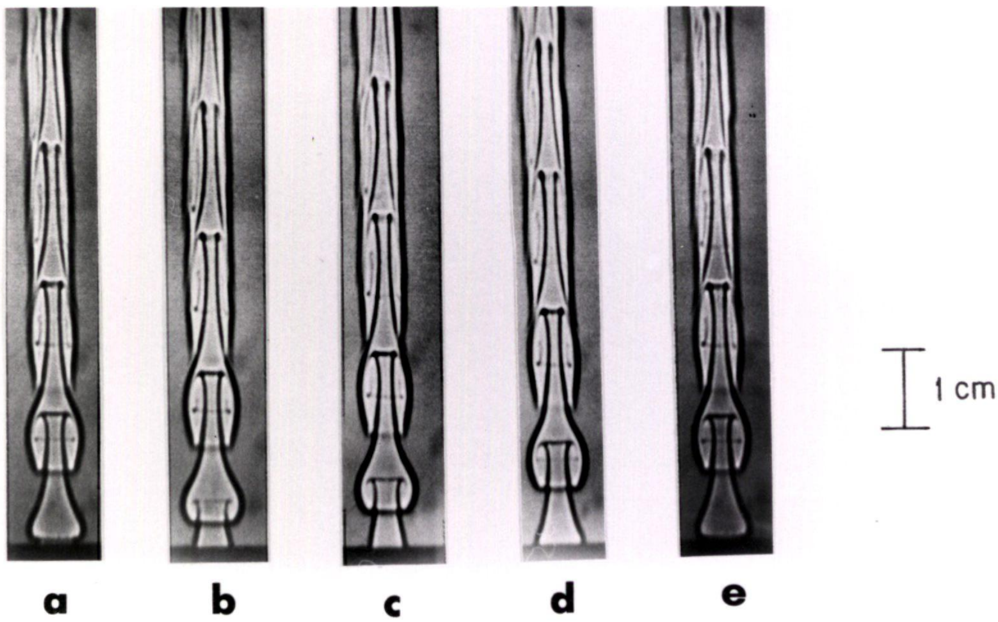
1 cm
a
b
c
d
e

causes the jet diameter to be almost uniform. The corresponding streaklines computed with tenth power profile at the orifice are shown in Figure 5.31. Similar to the experimental observations the vortices cascade with each other and keep the jet diameter almost uniform.

Although the velocity amplitude was 100% of the mean flow, no break or discontinuity at the nozzle is observed for any of the flows described above.

5.2.4 Intermediate to large amplitude of pulsation; $Re_0 = 200$, $25\% \leq \varepsilon \leq 50\%$, $0.5 \leq f^* \leq 5$ Hz

In this section evolution of flow patterns at $Re_0 \sim 200$ and intermediate to large amplitudes (25% - 50%) with varying frequencies are considered.

Figure 5.32 shows the sequence of photographs of the jet pulsed with a frequency of 1 Hz and amplitude of 25%. The flow is similar to that for $Re_0 = 102.7$, $f^* = 0.5$ Hz and $\varepsilon = 10\%$ (Figure 5.7). The jet outline shows slight undulation. Weak surface perturbations or disturbances are observed. These do not become amplified. No apparent internal patterns are observed.

The corresponding streaklines are shown in Figure 5.33. At the start a little swelling of the jet column is observed close to the nozzle. The diameter of the swollen part increases as it convects downstream. After 0.4 seconds, the outermost streakline starts to penetrate into the jet column and thus a core flow is established. The core flow is not observed in the actual experiments.

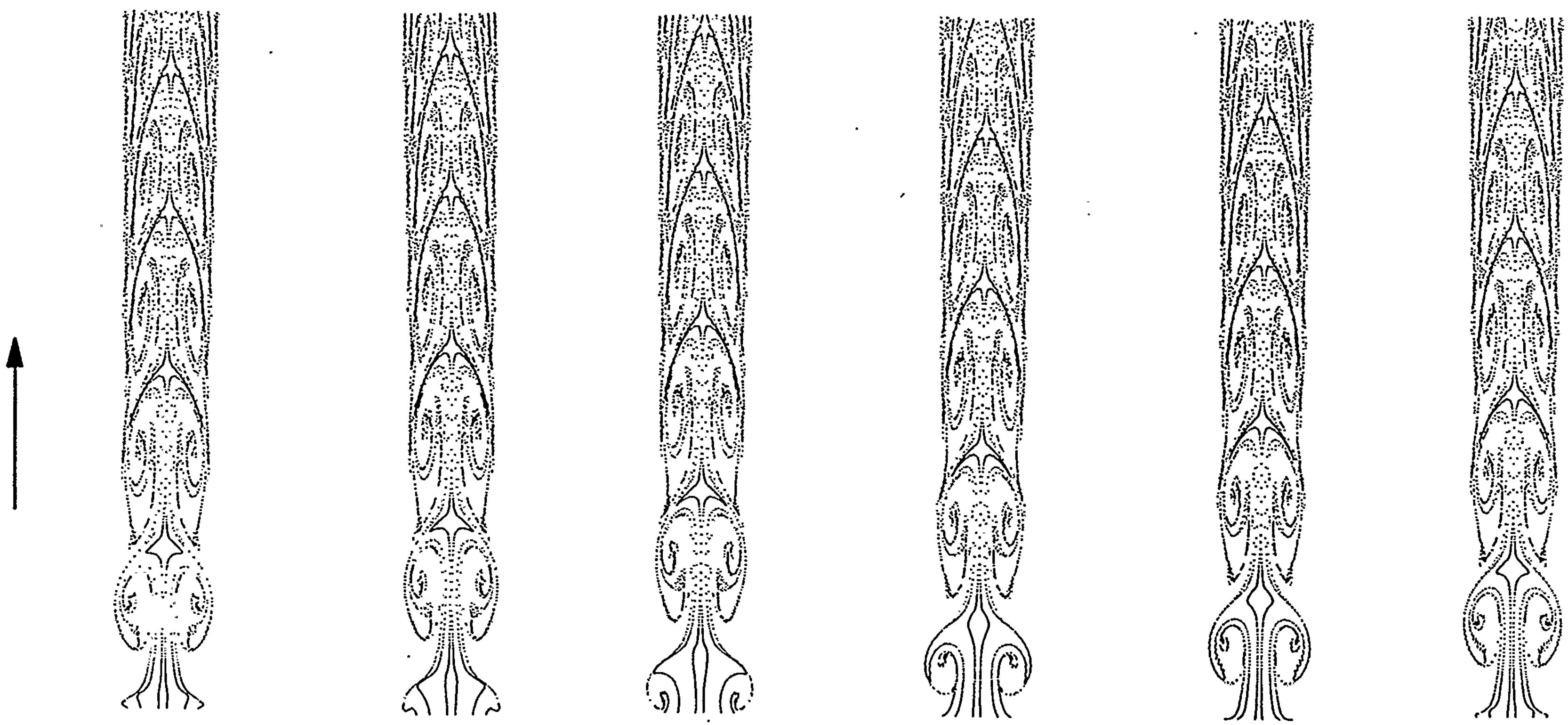

0.0 0.1 0.2 0.3 0.4 0.5

Figure 5.31 : Streaklines for pulsed laminar jets. $Re_0 = 100$, $f^* = 2$ Hz, $\varepsilon = 100\%$, Profile III (eq. 4.42), $t_c = 8.02$ s.

Figure 5.32 : Sequence of photographs for a pulsation cycle. $Re_0 = 200.3$, $f^* = 1$ Hz and $\varepsilon = 25\%$. $0.3 \leq \xi \leq 0.35$.

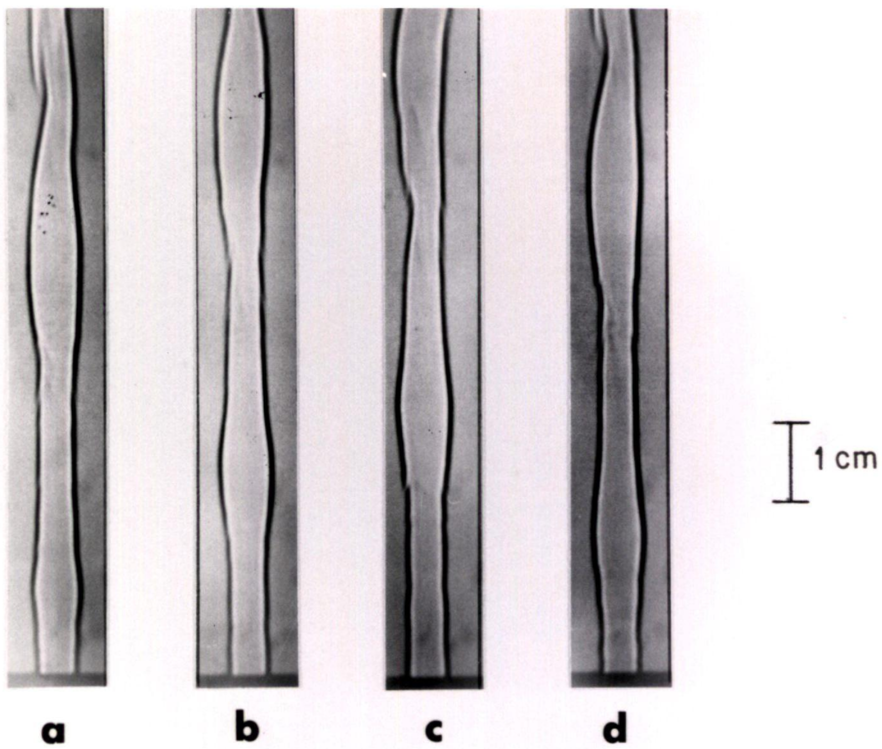
1 cm
a
b
c
d

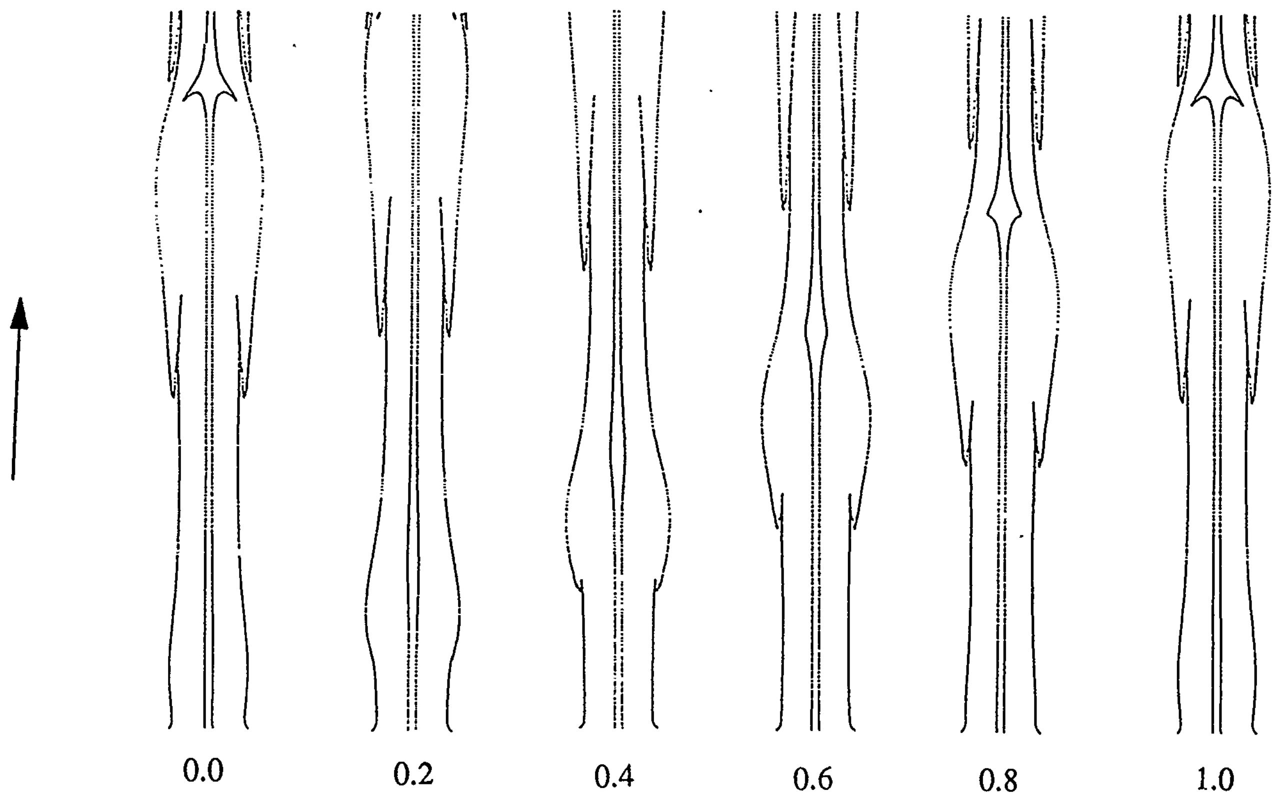

Figure 5.33 : Streaklines for pulsed laminar jets. $Re_0 = 200$, $f^* = 1$ Hz, $\varepsilon = 25\%$, Profile III (eq. 4.42), $t_c = 5$ s.

The sequence of photographs of the jet when pulsed at a frequency of 2.5 Hz and amplitude of 25% is shown in Figure 5.34. Close to the nozzle the dynamics and shapes of the vortices are similar to those observed in Figure 5.21 ($Re_0 = 100$, $f^* = 1.25$ Hz, $\varepsilon = 50\%$). However, in the present flow the spiralling flow does not remain confined within an annular layer between the edge of the vortex and its central core. The ring vortex is unstable and immediately breaks into a rapidly spreading irregular flow pattern.

The sequence of photographs at twice the amplitude in the foregoing and at a frequency of 2.5 Hz is shown in Figure 5.35. The flow patterns are not significantly different except in details. The spread of the irregular jet is also higher than in Figure 5.34.

The streakline plots for $f^* = 2.5$ Hz and $\varepsilon = 50\%$ are shown in Figure 5.36. The shape and dynamics of the computed vortices match closely with the experiment (Figure 5.35), close to the orifice. However, the discharge of isolated vortex rings and disintegration of the rings (onset of instability) were not predicted in the computation. The corresponding instantaneous streamline plots are shown in Figure 5.37.

The sequence of photographs at a high frequency of 5 Hz and amplitude ε of 25% is shown in Figure 5.38. The flow is stabilized due to stretching and cascading of the vortices. The jet diameter becomes almost uniform after about 6 nozzle diameter from the nozzle.

Figure 5.34 : Sequence of photographs for a pulsation cycle. $Re_0 = 200.3$, $f^* = 2.5$ Hz and $\varepsilon = 25\%$. $0.10 \leq \xi \leq 0.15$.

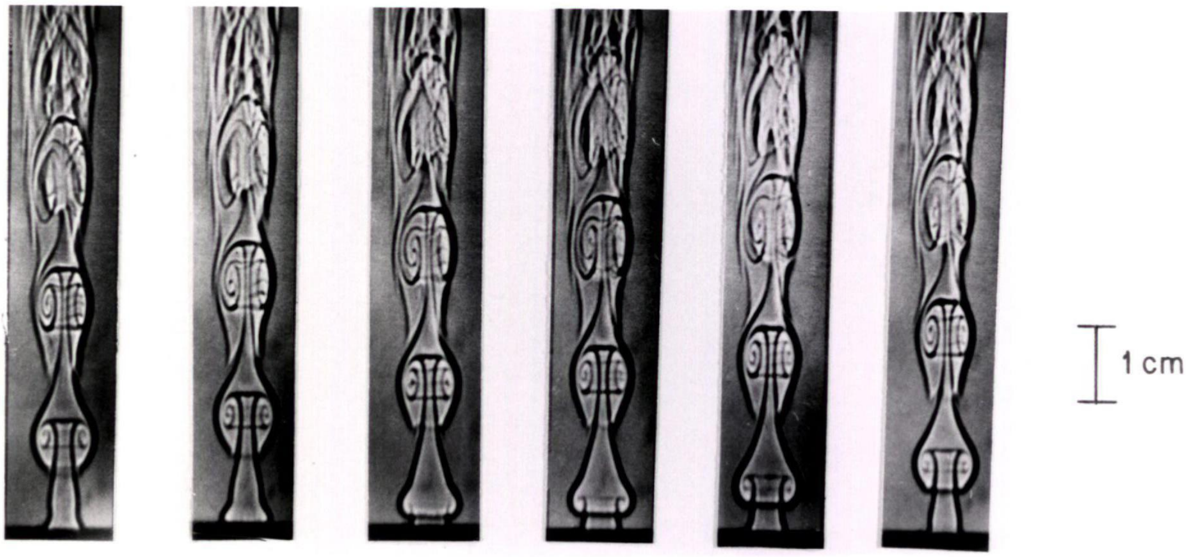

a b c d e f

Figure 5.35 : Sequence of photographs for a pulsation cycle. $Re_0 = 200.3$, $f^* = 2.5$ Hz and $\varepsilon = 50\%$. $0.10 \leq \xi \leq 0.15$.

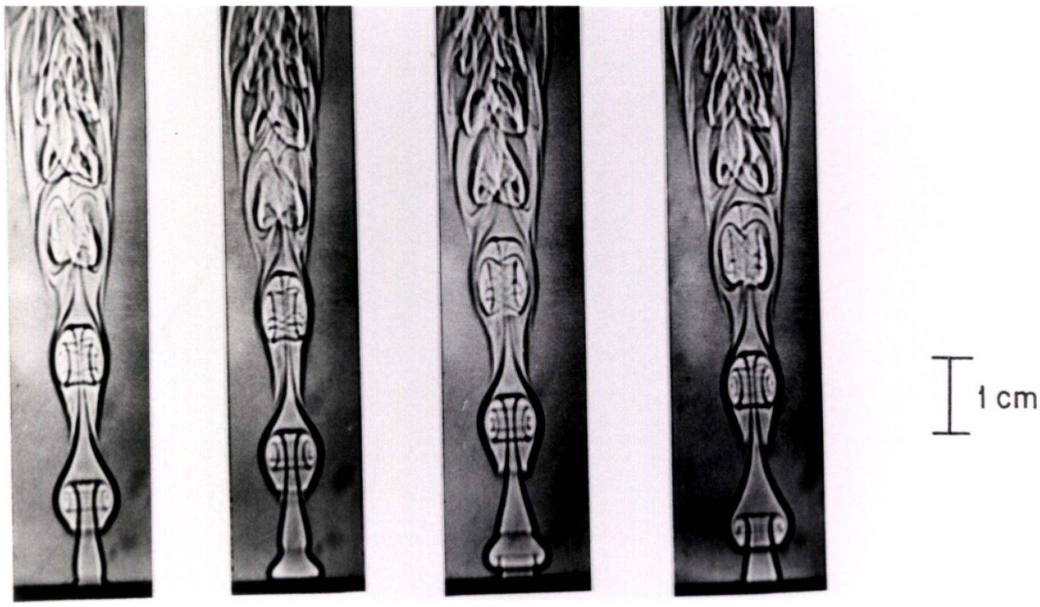

a b c d

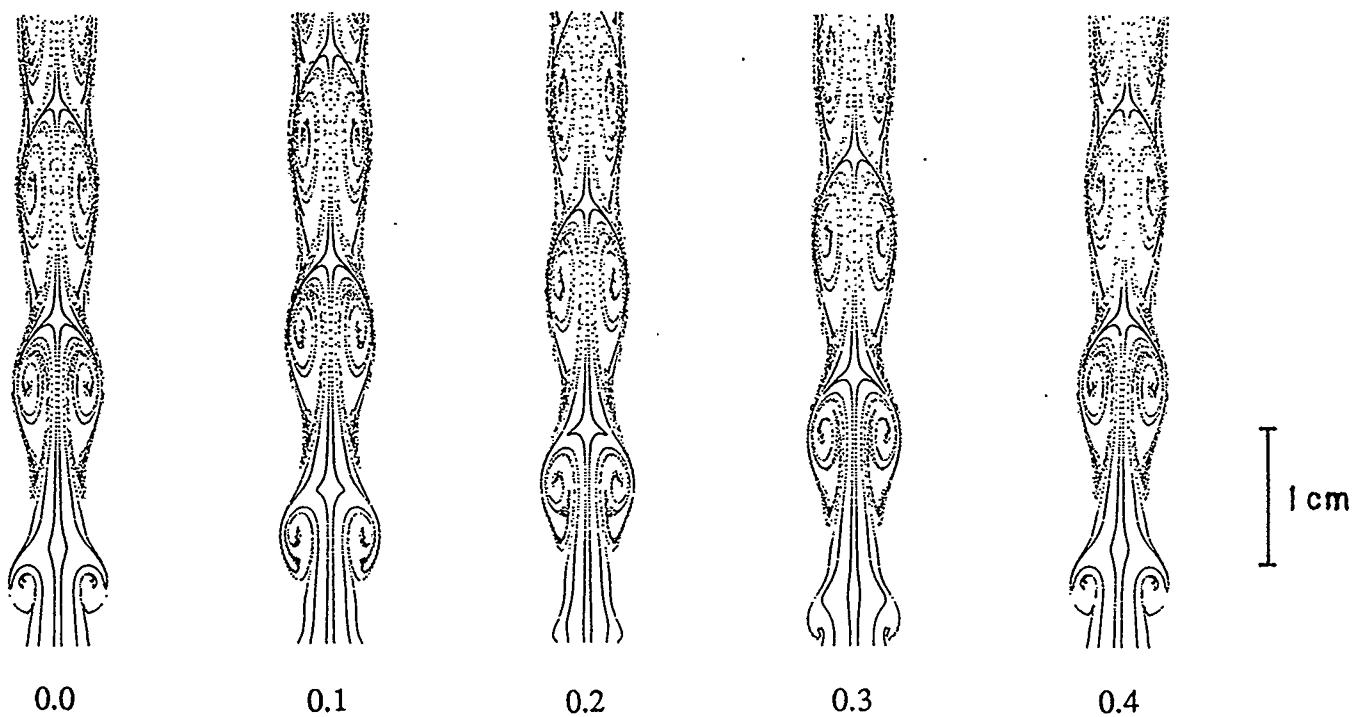

Figure 5.36 : Streaklines for pulsed laminar jets. $Re_0 = 200$, $f^* = 2.5$ Hz, $\varepsilon = 50\%$, Profile III (eq. 4.42), $t_c = 3$ s.

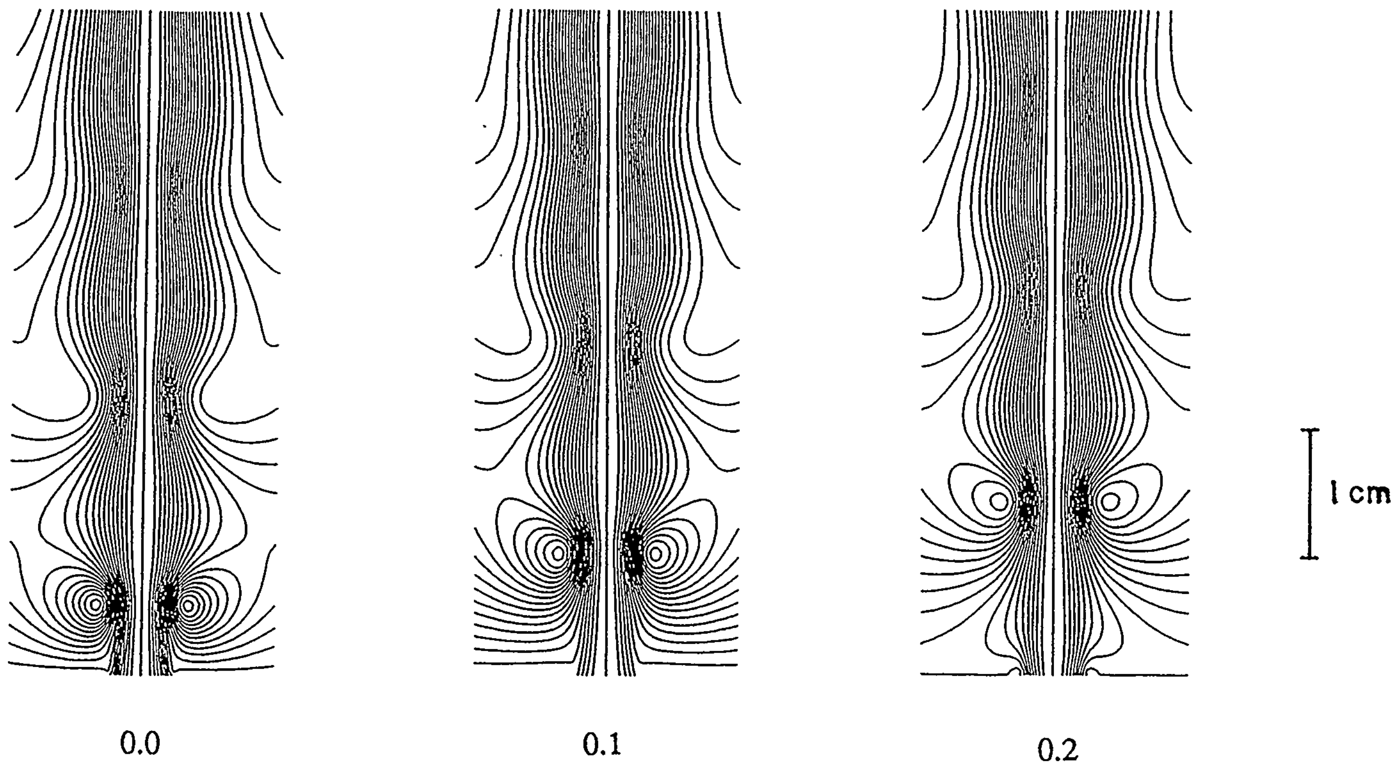

Figure 5.37 : Streamlines for pulsed laminar jets. $Re_0 = 200$, $f^* = 2.5$ Hz, $\varepsilon = 50\%$, Profile III (eq. 4.42), $t_c = 3$ s.

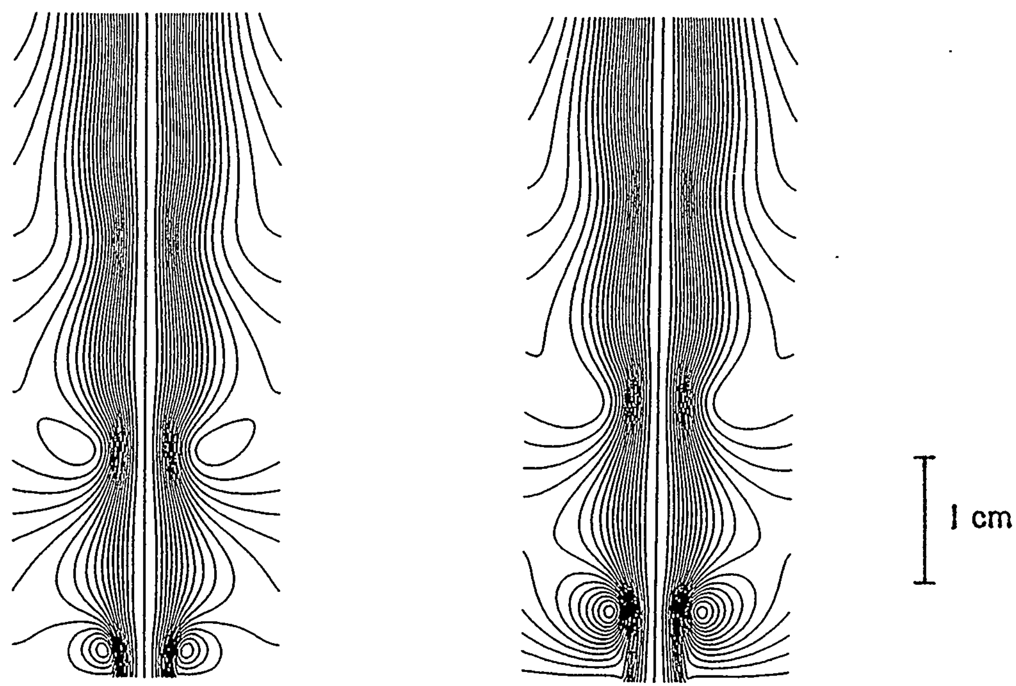

0.3 0.4

Figure 5.37 : continued

Figure 5.38 : Sequence of photographs for a pulsation cycle. $Re_0 = 200.3$, $f^* = 5$ Hz and $\varepsilon = 25\%$. $0.05 \leq \xi \leq 0.07$.

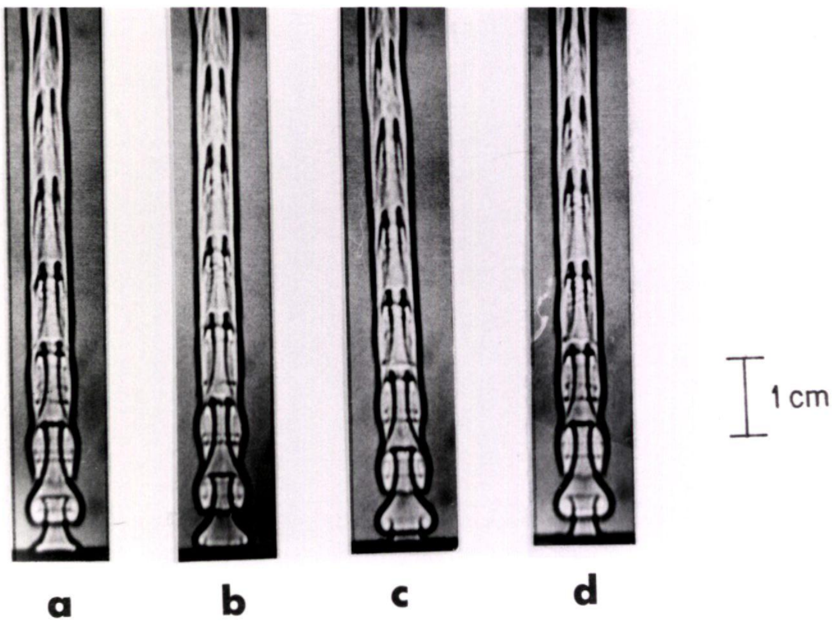
1 cm
a
b
c
d

At lower frequencies, $f^* = 1$ Hz, the patterns are different as shown in Figure 5.39. The formation and initial development of the ring vortex is similar to those observed for $Re_0 = 100.7$, $f^* = 0.5$ Hz and $\varepsilon = 100\%$ (Figure 5.25). In the present flow, the circulation inside the vortex appears to be much stronger. After about 10 nozzle diameter from the orifice, the vortex detached from the jet column and formed an isolated vortex ring. The corresponding streakline plots are shown on Figure 5.40. The patterns match closely with the experimental observations, except that isolated rings were observed formed in experiments about 8 - 9 nozzle diameters downstream of the orifice.

Figure 5.39 : Sequence of photographs for a pulsation cycle. $Re_0 = 200.3$, $f^* =$ 1 Hz and $\varepsilon = 100\%$.. $0.28 \leq \xi \leq 0.32$.

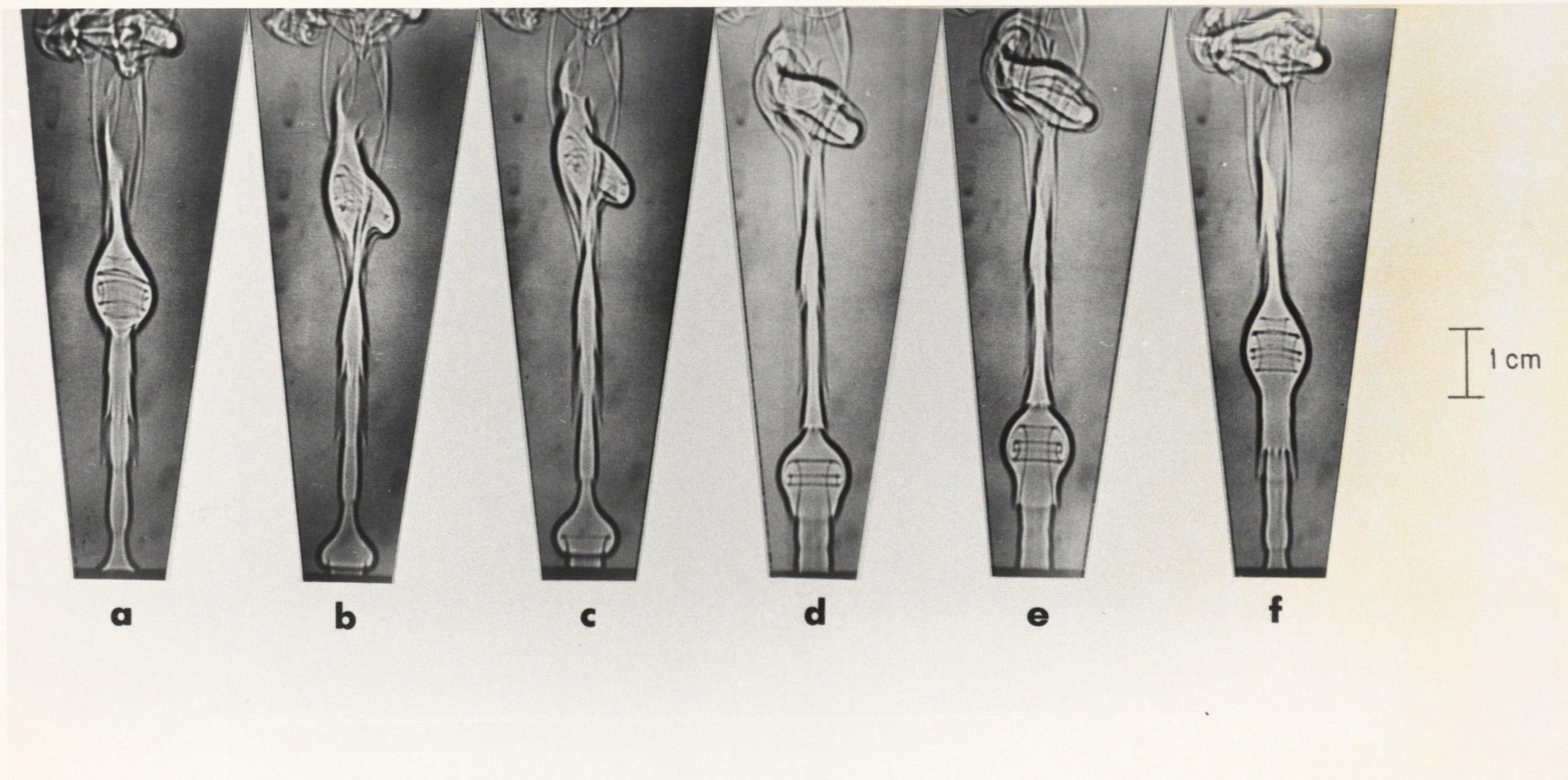
1 cm
a
b
c
d
e
f

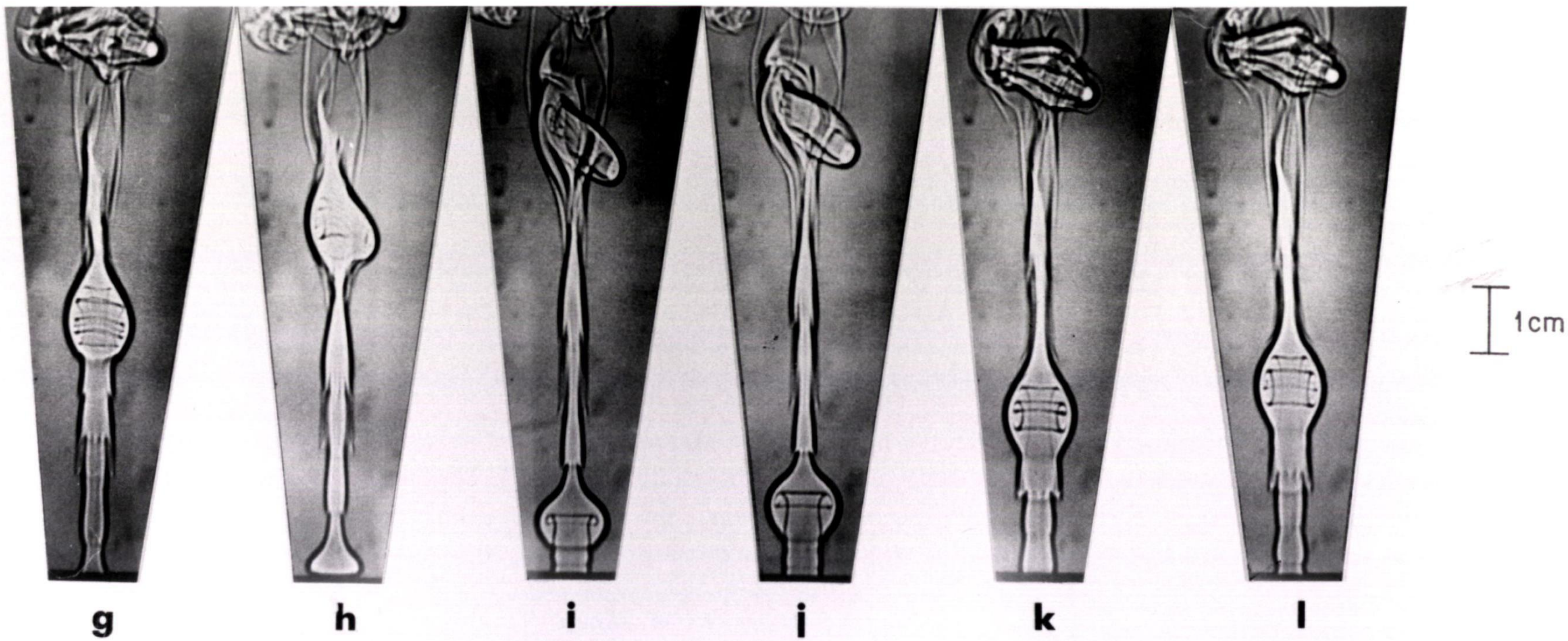
1cm
g
h
i
j
k
l

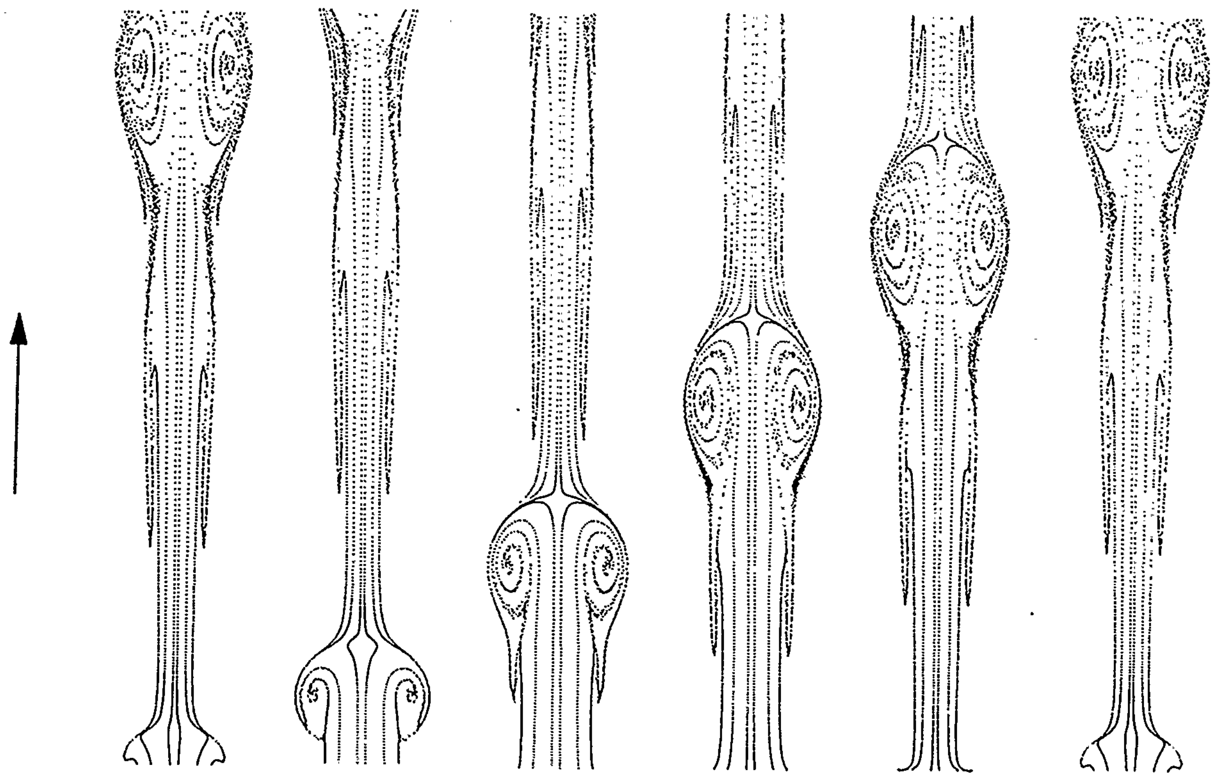

0.0 0.2 0.4 0.6 0.8 1.0

Figure 5.40 : Streaklines for pulsed laminar jets. $Re_0 = 200$, $f^* = 1$ Hz, $\varepsilon = 100\%$, Profile III (eq. 4.42), $t_c = 5$ s.

6. DISCUSSION

In the foregoing section, the experimental and computational results were presented on the basis of the primitive variables for the system; the average velocity through the orifice, the frequency of fluid pulsation (as produced by piston actuation) and the amplitude of variations in the flow rate. These results are now discussed with respect to categories of flow patterns and nondimensional parameters. The importance of the velocity profiles at the orifice to the computational modelling of experimental observations is also considered.

6.1 Classifications based on Images; Schlieren field and Streakline plots

The flow patterns observed through Schlieren optics and predicted by the streakline plots are classified in four different categories. Patterns observed (or predicted) under different operating conditions, which are nonetheless similar in visual form comprise a category. Such classes are compiled below.

6.1.1 Category 1

Category 1 represents the patterns which, from visual display via Schlieren optics, show periodic swellings or bulbs along the jet column in response to flow pulsation. No structures are observed formed within or intruding into the swellings.

Flows with such simple features are generally observed at low pulsation amplitude ($\leq \sim 25\%$) and low frequency (~ 0.5-1 Hz). The higher values of both variables correspond to the higher Reynolds number in this study. The flow conditions and the corresponding appearance as presented in the Figures in Chapter 5 are listed in Table 6.1. From calculations and the results plotted as streaklines, at $Re_0 = 200$, $f^* = 1$ Hz and $\varepsilon = 25\%$ for Figure 5.33, there is evidence that some entrainment of water (core flow) occurred. It is important to note however, that the velocity profiles at the orifice were invariant with time in the calculations. This condition may not have been met experimentally.

6.1.2 Category 2

The features for this category, designated as "core flow", include the intrusion of a stream of jet fluid, surrounded by a thin film of water entrained from the reservoir. A distinct core region, seemingly moving at a uniform speed and at a faster rate than the surrounding liquid is noted. The thin film of advected water terminates abruptly without curling. The projection is continuously elongated within the surrounding swelling while both moved downstream at different speeds. Typical conditions for this form and the corresponding figures are presented in Table 6.2.

Contrasted to the streakline plots at $Re_0 = 100$, $f^* = 2$ Hz and $\varepsilon = 10\%$ (Figure 5.15), core flows with distinctly visible rims (i.e. the edge of the advected

Table 6.1 : Conditions for pulsed laminar jets with periodic swellings and no internal structures

Re_0	f^* (Hz)	ε (%)	Figure No.
100	0.5	10	5.7, 5.8
200	1	25	5.32, 5.33

Table 6.2 : Conditions for pulsed laminar jets with "core flows" but no curling structures

Re_0	f^* (Hz)	ε (%)	Figure No.
100	1	10	5.9, 5.10
100	1.7	10	5.14
100	2	10	5.15
100	2.4	10	5.16

water film was not diffuse but sharply visible) were observed during the experiment under the same condition. For the others, at increased frequencies the core ends show distinct rims or edges as if the water film has been slightly thickened there (Figure 5.16). This may be interpreted as incipient curling of sheets within the flow field.

6.1.3 Category 3

The flow patterns in this category show progressive development and axial displacement of spiral from rings of vortex filaments within swellings on the jet column. These structures ultimately disintegrated spontaneously. The loops of the spirals were never closed and no isolated ring vortices were discharged. Each spiral always remained confined within an annular space between the outline of the swelling and a central core. For low frequencies of pulsation, the swellings were distinct (as in Figure 5.17 and 5.25). At increased frequencies, the structures were stretched longitudinally, nesting with the outline of the one ahead. The overall jet diameter within the schliere boundary remained nearly uniform for up to twenty nozzle diameters downstream. Similar patterns were obtained in streakline calculations (Figure 5.21, 5.30, 5.38). The flow conditions and the numbers of the figures in which the patterns are illustrated are listed in Table 6.3.

Table 6.3 : Conditions for pulsed laminar jets which exhibit spiralling structures within swellings

Re_0	f^* (Hz)	ε (%)	Figure No.
100	1.25	50	5.17, 5.18
100	2.5	50	5.21, 5.22
100	0.5	100	5.25, 5.26
100	2	100	5.30, 5.31
100	2.5	100	Not shown
200	5	25	5.38

6.1.4 Category 4

In this category of flows, isolated ring vortices were ultimately discharged. It is this type of structures that have been much discussed and analyzed (Thomson 1883, Maxworthy 1972, Widnall 1975, Saffman 1981, Lee and Reynolds 1983, Shariff and Leonard 1992). The initial development of the ring vortices is similar in progression to what was observed in Category 3. The spirals initiated remain confined within the annular layer that is located between the edge of the swelling and the central core. Downstream of the orifice, the core diameter shrinks. Vortex filaments may have undergone re-arrangements in response to perturbations (Ashurst, 1981; see Leonard, 1985) to evolve closed loops representative of ring vortices. The flow conditions and the figure numbers are presented in table 6.4.

6.2 Classifications based on nondimensional parameters

In the foregoing section (6.1) the flow patterns were classified in four different categories on the basis of similarities in appearances. An attempt is made in this section to classify the flow structures on the basis of nondimensional parameters which are described as follows.

Table 6.4 : Conditions for pulsed laminar jets which show discharge of isolated ring vortices

Re_0	f^* (Hz)	ε (%)	Figure No.
100	2.5	25	5.34
100	2.5	50	5.35
200	1	100	5.39

Reynolds number

The Reynolds number Re equals LU/ν where L is a characteristic length scale and U is a velocity scale typical for the system. The term ν is the kinematic viscosity. The Reynolds number is the ratio of the inertial to the viscous forces (Schlichting, 1979). In the present system, the most obvious length scale is the orifice diameter D. The velocity may be the time-averaged value $\bar{U}_0$ (which is volumetric rate over orifice area), the peak value $\bar{U}_0(1 + \varepsilon)$ or the root mean squared value $\bar{U}_0(1 + \frac{\varepsilon^2}{2})^{\frac{1}{2}}$ which reflects the periodic nature of the flow. Of these, only the first two were used. The Reynolds numbers are defined as follows,

$$Re_0 = \frac{D\bar{U}_0}{\nu}, \quad Re_{max} = \frac{D\bar{U}_0(1+\varepsilon)}{\nu}$$

Frequency parameter

The nondimensional frequency parameter used in the analysis is

$$f = \frac{f^*}{\bar{U}_0/D}$$

The ratio compares the rate of incremental momentum associated with pulsation at the orifice to the rate of convection of momentum by mean flow out of the orifice.

Circulation parameter

Another important parameter characterizes the excess vorticity generated and discharged over a cycle of pulsation. If the area-averaged velocity at the orifice is represented as $U_0(t^*) = \bar{U}_0(1 + \varepsilon \sin 2\pi f^* t^*)$ and slug flow through the nozzle is assumed, the rate of change of circulation from the nozzle is given by (Shariff and Leonard, 1992)

$$\frac{d\Gamma}{dt} = \frac{U_0^2(t^*)}{2} \tag{6.1}$$

The total circulation discharged over a pulsation cycle is,

$$\Gamma = \frac{1}{2}\int_0^T U_0^2 dt^* \tag{6.2}$$

where T is the time period of pulsation. The total circulation is contributed by both the steady flow component $\bar{U}_0$ and the unsteady component $(\bar{U}_0 \varepsilon \sin 2\pi f^* t^*)$. The excess circulation contributed by the periodic component over the steady component is given by,

$$\Gamma_p = \frac{1}{2}\int_0^T \varepsilon \bar{U}_0 \sin 2\pi f^* t^* dt^* = \frac{\bar{U}_0^2 \varepsilon^2}{4\pi f^*} \tag{6.3}$$

The nondimensional parameter characterizing the disharge of circulation is defined as (Shariff and Leonard, 1992)

$$\gamma = \frac{\bar{U}_0^2 \varepsilon^2}{4\pi f^* \nu}$$

The calculated values of all the nondimensional numbers mentioned above are presented in Table 6.5.

Two different approaches are adopted to characterize the flow patterns. In the first approach the use of two parameters "Re_{max}" and "f" is made and in the second approach the use of the single parameter "γ" is made.

Classification with respect to Re_{max} and f

At a constant Re_{max} of 110, the structures in the field varied progressively as the frequency parameter increased. For $0.1217 \leq f \leq 0.1248$ the flow patterns fall under Category 1 (varicose jet outline without core flow). When the range is $0.2434 \leq f \leq 0.4138$, the flow patterns fall under category 2 (core flow without sharp edge or rim) and when $0.4868 \leq f \leq 0.5842$ there appeared to be incipient curling of the water film entrained into the swellings.

For $150 \leq Re_{max} \leq 250$ the flow patterns fall under Category 3 (spiralling motion without discharge of isolated vortices). For $0.1217 \leq f \leq 0.304$ swellings were distinct or did not merge with each other (Figure 5.17, 5.25, 5.26, 5.29). For

Table 6.5 : Calculated dimensionless quantities

Category	Re_0	f^*	ε	Figure	Re_{max}	f	γ
1	100	0.5	10	5.7,5.8	110	.1217	0.637
	200	1	25	5.32,5.33	250	.1248	7.958
2	100	1	10	5.9,5.10	110	.2434	0.398
	100	1.7	10	5.14	110	.4138	0.187
	100	2	10	-	110	.4868	0.159
	100	2.4	10	5.16	110	.5842	0.133
3	100	1.25	50	5.17,5.18	150	.304	6.366
	100	2.5	50	5.21,5.22	150	.609	3.183
	100	0.5	100	5.25,5.26	200	.1217	63.66
	100	1	100	5.29	200	0.25	31.83
	100	2	100	5.30,5.31	200	.487	15.92
	100	2.5	100	-	200	.609	12.73
	200	5	25	5.38	250	.624	1.592
4	200	2.5	25	5.34	250	.312	3.183
	200	2.5	50	5.35	300	.312	12.73
	200	1	100	5.39	400	.1248	127.3

$0.487 \leq f \leq 0.624$ the swellings merged with each other (Figure 5.21, 5.22, 5.30, 5.31, 5.38). The results would suggest that the relative rate of incremental momentum to the rate of convection of discharge momentum by the mean flow is important in indicating whether the swellings will remain discrete or become nested. A ratio ~ 0.5 or greater may be needed for merging of swellings.

For $Re_{max} \geq 250$, the discharge of isolated ring vortices were observed which corresponds to Category 4. Values for f are less than 0.5 and swellings are distinct. It is noted that both Figure 5.34 and Figure 5.38 have the same Re_{max} (250) but the vortices merge when $f = 0.624$ (Figure 5.38) and are discharged when $f = 0.312$ (Figure 5.34).

An anomaly in the data is observed for $Re_0 = 200$, $f^* = 1$ Hz and $\varepsilon = 25\%$. The value of Re_{max} corresponding to this flow is 250 which is outside the range of Re_{max} for category 1. The flow pattern was anticipated to fall under category 4.

Classification with respect to γ

For $0.4 < \gamma < 1.6$ the flow patterns fall under Category 1. For $0.133 < \gamma < 0.4$ the flow patterns fall under Category 2. For $0.133 < \gamma < 0.159$ the incipience of curling is observed. For $1.6 < \gamma$ the flow patterns fall under Category 3 and Category 4. Distinction between Category 3 and Category 4 could not be made using γ alone.

Again an anomaly is observed for the flow at $Re_0 = 200$, $f^* = 1$ Hz and $\varepsilon =$

25%. The value of γ corresponding to this flow is 7.958 which falls outside the range of γ for category 1. The flow was anticipated to fall under category 3 or category 4.

6.3 Velocity profile at the orifice

For the experiments, a converging nozzle was used in the attempt to achieve a near flat profile at the orifice. The actual shape of the profile was unknown as no velocity measurement was made. This poses a problem in determining the exact boundary condition at the orifice during numerical analysis. An arbitrary functional form for the steady velocity profile at the orifice is imposed (Profile III, Equation 4.42). This profile is termed as the 'tenth power profile' because of the nature of the function. The profile satisfies two important criteria, namely, the flatness of the velocity profile near the centre of the nozzle and the no slip condition at the nozzle wall (see Figure 4.2). Since, the flow of a jet is found to depend on the velocity profile at the source (Ito et al. 1979, Akaike et al. 1988) numerical experiments were performed with two other velocity profiles, namely, a parabolic profile (Profile I, Equation 4.40) and a sixth power profile (Profile II, Equation 4.41). The parabolic profile does not have any flat portion near the centre and the gradient of velocity near the nozzle wall is much smaller than that for the tenth power profile. The sixth power profile is intermediate to the parabolic and the tenth power profiles. The radial velocity v, is assumed to be zero for all the profiles mentioned above, although the actual velocity must have a small but non-zero radial component due to the convergence of the nozzle.

For unsteady flow through the nozzle, the situation is more complicated. Calculation of steady flow through a two dimensional converging channel by Millsaps and Pohlhausen (1953) indicates that the shape of the velocity profile at the end of the channel depends on the Reynolds number. The flatness of the profile increases with the Reynolds number. Since, the instantaneous Reynolds number for the pulsatile flow in the present experiments varies with time, the shape of the velocity profile at the orifice is expected to change with time over a cycle. Such a feature was not considered in the numerical modelling. The shape of the velocity profile was assumed to remain the same over a cycle (Equation 4.9a and 4.9b). Secondly, the instantaneous velocity at any radial position at the orifice is assumed to be in phase with the instantaneous velocities at every other radial locations. This may not be true because a phase lag between the instantaneous velocities at different radial locations may exist due to the boundary layer formation along the nozzle wall.

It was observed in Chapter 5 that the computed velocity profiles for a steady jet and the streakline patterns for pulsed jets veried considerably with the imposed velocity profiles at the orifice. For example, the streakline plots computed with tenth and sixth power profiles (Figure 5.18 and 5.19) predicted the vortical motions observed in the experiments (Figure 5.17) for $Re_0 = 100$, $f = 1.25$ Hz and $\varepsilon = 50\%$.

The streakline plots computed with the parabolic profile did not predict any vortical motion (Figure 5.20). This was probably due to the fact that the velocity gradient and hence the vorticity at the nozzle wall is much smaller for parabolic profile than for sixth and tenth power profiles (see Figure 4.42). These features suggest that the flow inside the nozzle should be computed in order to better predict the experimental observations.

7. CONCLUSIONS AND RECOMMENDATIONS

Experiments have been performed to determine the structures which evolve in a flow field when a jet is laminar and pulsed at large amplitude. Four different flow structures were identified.

The problem has been simulated numerically and successfully subject to imposition of a fixed or invariant (with time) velocity profile at the orifice. Three different profiles were examined.

The resolution of the Schlieren images may be improved by using a two element (two mirrors) optical system rather than a single element system as used in this study.

High speed photographs may resolve the dynamic progression of the flow structures better than still photographs.

The instantaneous velocity profile at the orifice should be known for better modelling. This could be achieved through velocity measurements at the orifice and calculation of flow inside the nozzle.

Computation of mean and transient entrainment rate, momentum and kinetic energy flux should be carried out.

REFERENCES

Abramovich, G.N., *The Theory of Turbulent Jets*, MIT Press, Cambridge, Mass., (1963)

Abramovich, S. and A. Solan, "*The initial development of submerged laminar round jet.*" Journal of Fluid Mechanics, **53**, 791, (1973)

Akaike, S. and M. Nemoto, "*Potential core of a submerged laminar jet*", Trans. ASME, **110,** 392, (1989)

Anderson, A.B.C, " *The jet-tone orifice number for orifices of small thickness - diameter ratio.*", J. Acoust. Soc. Am., **26**, 21, (1954)

Anderson, A.B.C, " *Structure and velocity of the periodic vortex-ring flow pattern of a primarily Pfeifentone (pipe tone) jet.*", J. Acoust. Soc. Am., **27**, 1048, (1955)

Anderson, A.B.C, " *Vortex ring structure-transition in a jet emitting discrete acoustic frequency.*", J. Acoust. Soc. Am., **28**, 914, (1956)

Andrade, E.N. and L.C. Tsien, " *The velocity distribution in a liquid into liquid jet*", Proc. Phys. Soc. Lond., **46**, 381, (1937)

Batchelor, G.K., *An introduction to fluid dynamics*, University Press, Cambridge, (1967)

Beavers, G. and T.A. Wilson, "*Vortex growth in jets*", Journal of fluid mechanics, **44**, 97, (1970) Becker, H. and T. Massaro, "*Vortex evolution in a round jet*", Journal of Fluid Mechanics, **31**, 435, (1968)

Bousfield, D.W., I.H. Stockel and C.K. Nanivadekar, " *The breakup of viscous jets with large velocity modulations*", Journal of Fluid Mechanics, **216**, 601, (1990)

Burden, R.L., J.D. Faires and A.C. Reynolds, *Numerical analysis*, Wadsworth International Student Edition, (1989)

Chanaud, R.C. and A. Powell, "*Experiments concerning the sound sensitive jet*", Journal of Acoustical Society of America, **34**, 907, (1962)

Chen, C.I. and W. Rodi, *Vertical Turbulent Buoyant Jets - A Review of Experimental Data*, Pergamon Press, Oxford (1980)

Fasel, H.R., "*Numerical solution of the complete Navier-Stokes equations for the simulation of unsteady flows.*", Lecture Notes in Mathematics, **771**, 177, Springer-Verlag, Germany, (1979)

Fox, H., R. Sinha and L. Weinberger, "*An Implicit finite difference solution for jet and wake problems*", Astronautica Acta., **17**, 265, (1972)

Ganong, W., *Review of medical physiology*, Appleton and Lange, California, (1991)

Goldstein, S., *Modern development in fluid dynamics, v I,II*, Clarendon Press, Oxford, (1938)

Grant, A.J., "*A numerical model of instability in axisymmetric jet*", Journal of Fluid Mechanics, **66**, 707, (1974)

Hama, F.R., "*Streaklines in a perturbed shear flow*", The Physics of Fluids, **5**, 644, (1962) Ho, C.M. and P. Huerre, "*Perturbed free shear layers*", Ann. Rev. Fluid Mech., **16**, 365, (1984)

Ikeda, M., "*Finite disturbances and growing vortices in a two-dimensional jet*", Journal of Fluid Mechanics, **80**, 401, (1977)

Ito, R. and T. Seno, "*Effect of exit geometry on jet behaviour*", J. Chem. Eng. Japan, **12**, 430, (1979)

Kaden, H., "*Curling of an unstable discontinuity interface*", NASA Tech. Trans., TT F-14, 230, (1931)

Kline, S.J., "*Flow visualization*" in Illustrated Experiments in Fluid Mechanics, The NCFMF Book of Film Notes, MIT Press, Cambridge, (1980)

Kurosaka, M. and P., Sundaram, "*Illustrative examples of streaklines in unsteady vortices: Interpretational difficulties revisited*", Physics of Fluids, **29**, 3474, (1986)

Lai, J.C.S. and J.M. Simmons, "*Numerical solution of periodically pulsed laminar free jets*", AIAA Journal, **19**, 813, (1981)

Lighthill, M.J., "*Introduction. Boundary layer theory*", in Laminar Boundary Layers, 56, Ed. Rosenhead, L., Oxford, (1961)

List, E.J., " Turbulent Jets and Plumes ", *Ann. Rev. Fluid Mech*, **14**, 189, (1982)

Mattingly, G.E. and C.C. Chang, "*Unstable waves on axisymmetric jet column*", Journal of Fluid Mechanics, **65**, 541, (1974)

Maxworthy, T., "*The structure and stability of vortex rings*", Journal of Fluid Mechanics, **51**, 15, (1972) McCormack, P.D, D. Cochran and L. Crane, " *Periodic vorticity and its effect on jet mixing*", Physics of Fluids, **9**, 1555, (1966)

McNaughton, K.J. and C.G. Sinclair, "*Submerged jets in short cylindrical flow vessels*", Journal of Fluid Mechanics, **25**, 367, (1966)

Michalke, A., "*Vortex formation in a free boundary layer according to stability theory*", Journal of Fluid Mechanics, **22**, 371, (1965)

Michalke, A. and P. Freymuth, "*The instability and the formation of vortices in a free boundary layer*", AGARD, Conf. Proc. no. 4, paper 2, (1966)

Mollendorf, J.C. and B. Gebhart, "*Thermal buoyancy in round laminar vertical jets*" Int. J. Heat Mass Transfer, **16**, 735, (1973)

Mollendorf, J.C. and B. Gebhart, "*An experimental and numerical study of the viscous stability of a round laminar vertical jet with and without thermal buoyancies for symmetric and asymmetric disturbances.*", Journal of Fluid Mechanics, **61**, 367, (1973)

Pai, S.I., " Fluid Dynamics of Jets ", *D. Van Nostrand Co.*, (1954)

Perry, R.H. and C.F., Chilton, *Chemical Engineers' Handbook*, McGraw-Hill Kogakusha, Ltd. Tokyo, (1973)

Press, W., B. Flannery, S. Teukolsky and W.T. Vetterling, *Numerical Recipes*, Cambridge University Press, (1989)

Rankin, G.W., K. Sridhar, M. Arulraja and K.R. Kumar, " *An experimental investigation of laminar axisymmetric submerged jets* ", Journal of Fluid Mechanics, **133**, 217, (1968) Reynolds, A.J., "*Observations of a liquid into liquid jet*", Journal of Fluid Mechanics, **14**, 552, (1962)

Roache, P.J., *Computational fluid dynamics*, Hermosa Publ., New Mexico, (1976)

Rodi, W., "A review of experimental data of uniform density free turbulent boundary layers", in *Studies in Convection,* Ed. B.E. Launder, Academic Press, New York, 79, (1975)

Rosenhead, L., *Laminar boundary layers*, Clarendon Press, Oxford, (1963)

Ross, B., *Steam-induced buoyant jets in slurries*, M.Sc thesis, Univ. of Calgary, (1990)

Sarpkaya, T., "*Computational methods with vortices - the 1988 Freeman scholar lecture*", Journal of fluids engineering, **111**, 5, (1989)

Sato, H., "*The stability and transition of a two dimensional jet*", Journal of Fluid Mechanics, **7**, 53, (1960)

Schlichting, H., *Boundary Layer Theory*. McGraw-Hill, Toronto, (1979)

Seno, T., S. Kageyama and R.Ito," *Effect of controlled pulsation on axisymmetric jet behaviour*", J. Chem. Eng. Japan, **20**, 128, (1987)

Seno, T., S. kageyama and R. Ito., "*A modelling of vortex rings in an axisymmetric pulsed jet*", J. Chem. Eng. Japan, **21**, 1, (1988)

Shariff, K. and A., Leonard, Annn. Rev. Fluid Mech., **24**, 235, (1992)

Siekmann, J., "*On a pulsating jet from the end of a tube, with application to the propulsion of certain aquatic animals*", Journal of Fluid Mechanics, **16**, 399, (1962) Sweet "*Connections between fluid mechanics and industrial problems*", Rev. Sci. Instr., **36**, 117, (1965)

Thompson, J.F., "*Numerical solution of flow problems using body-fitted coordinate systems*", Lecture notes on computational fluid dynamics. Von Karman Institute for Fluid Dynamics, Brussels, 1978. Hemisphere Publishing Corporation (1979)

Tritton, D.J., *Physical fluid dynamics*, Clarendon Press, Oxford, (1988)

Turner, J.S., "*The starting plume in natural surroundings*", Journal of Fluid Mechanics, **13**, 356, (1962)

Vermeulen, P.J., P. Rainville and V. Ramesh, "*Measurements of the entrainment coefficient of acoustically pulsed axisymmetric free air jets*", ASME paper 91-GT-235, International gas turbine and aeroengine congress and exposition, Orlando, FL june 3-6, 1991

Weast, R.C., ed., *Handbook of Chemistry and Physics*, CRC Press, Ohio, (1977)

Wille, R., "*Growth of velocity fluctuations leading to turbulence in a free shear layer*", Hermann Fottinger Inst., Berlin, AFOSR Tech. Rep. Contract AF 61(052)-412, (1963)

Yule, A.J., "*Large-scale structure in the mixing layer of a round jet*", Journal of Fluid Mechanics, **89**, 413, (1978)

Zauner, E., "*Visualization of the viscous flow induced by a round jet*", Journal of Fluid Mechanics, **154**, 111, (1985)

APPENDIX A

The design and operation of the cam-piston assembly.

The design of the cams which drive the piston to produce the pulsatile flow is described in this section. The instantaneous area-averaged velocity at the orifice is represented by $\bar{U}_0(1+\varepsilon\sin\eta t^*)$ where, $\bar{U}_0$ is the steady mean velocity. The amplitude of pulsation is $\bar{U}_0\varepsilon$ and the angular frequency is η. A characteristic plot of velocity (spatial average at the orifice) versus time is shown in Figure A.1. Oscillations a4re imposed on a constant flow obtained by maintaining a steady supply of the liquid into the nozzle assembly. The periodic discharge is achieved through longitudinal movements of a piston inside the central chamber (Figure 3.2). Since the diameter of the chamber is double that for the orifice, the piston travel rate is one-fourth of the instantaneous average velocity at the orifice which is expressed as,

$$u = \frac{\bar{U}_0\varepsilon}{4}\sin\eta t^* \qquad \text{(A.1)}$$

The piston actuation is achieved with a cam-follower arrangement as illustrated in Figure A.2. The follower is the stem of the piston. The contact between the cam and the follower is maintained by means of a small wheel which serves to minimize frictional resistance (Ham et. al., 1958). As the cam rotates, its outline is tracked by the wheel and the follower is displaced in the vertical direction. A spring mounted on the piston stem and attached between the wheel and the base

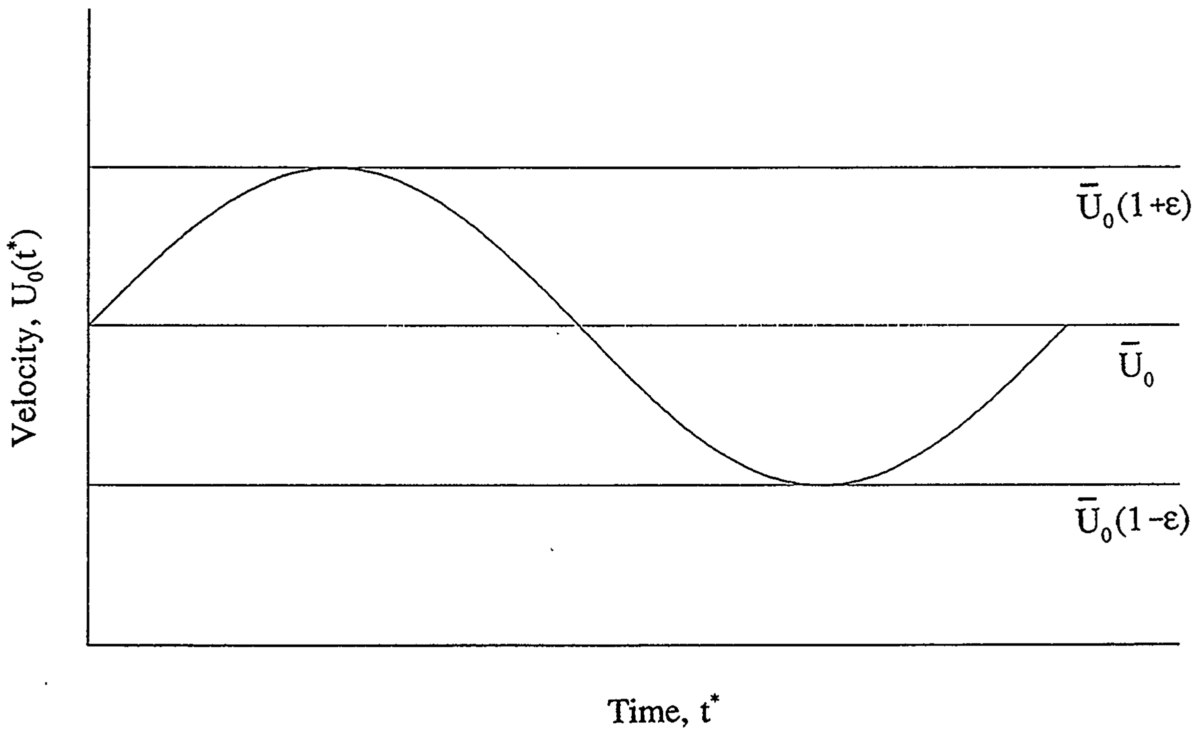

Figure A.1 : Characteristic plot of velocity (spatial averaged at the orifice) versus time

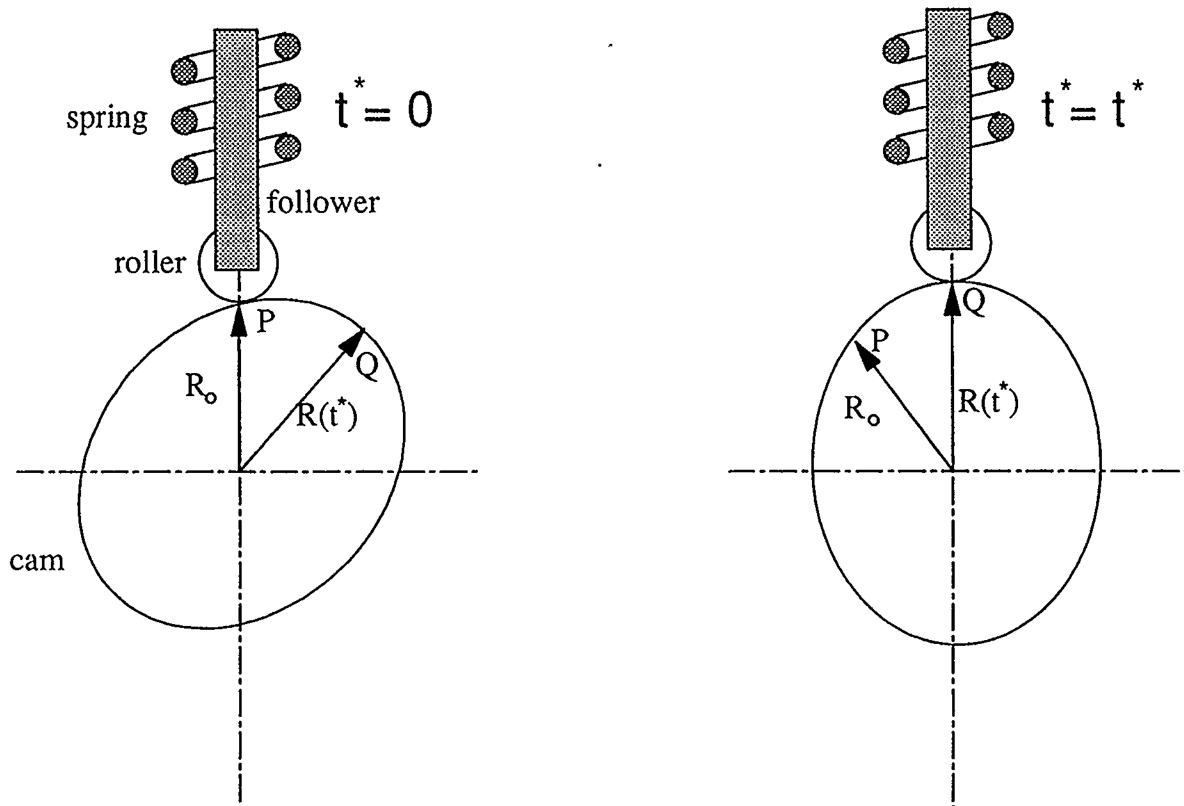

Figure A.2 : Schematic diagram of cam-follower arrangement of the nozzle forced the two parts to remain always in contact. It is essential however, that the spring should not be too stiff to strongly resist the cam's turning at certain positions. The lateral movements of the piston is also restricted by rings on the inner wall of the nozzle (Figure 3.2).

For illustration, it is considered in the following that the cam is rotating in a counter-clockwise direction with a uniform angular velocity η. At $t^* = 0$, the contact line on the cam is at P and the distance of the follower from the axis around which the cam rotates is R_0. After an elapsed period of dt^*, marker Q reaches the point where P was previously located. The distance of the contact from the axis of the cam is now $R(t^*)$. If the angle through which the cam has rotated during this interval is $d\theta$ then,

$$d\theta = \eta \, dt^* \tag{A.2}$$

The velocity of the longitudinal displacement of the follower is given by,

$$u = \frac{\partial R}{\partial t^*} = \frac{\partial R}{\partial \theta}\frac{\partial \theta}{\partial t^*} \tag{A.3}$$

When equations (A.1) through (A.3) are combined, one obtains

$$\eta \frac{\partial R}{\partial \theta} = \frac{\bar{U}_0 \varepsilon}{4} \sin\theta \tag{A.4}$$

An integration of this equation yields,

$$R = R_0 + \frac{\bar{U}_0 \varepsilon}{4\eta}(1 - \cos\theta) \tag{A.5}$$

Equation (A.5) represents the geometry of the cam. The term R_0 is the radius of the cam at $\theta = 0$ and this is also the minimum diameter of the cam. The maximum diameter of the cam is $R_o + \frac{2\bar{U}_0 \varepsilon}{4\eta}$. All the cams in this work were made of stainless steel and fabricated in the C.I.M machine with R_0 of 25.4 mm (1 inch). The computer program to generate the data file to design the cams is listed. The input variables for the program are the steady mean velocity, the frequency and the amplitude of pulsation. The data is written in the output file in a format compatible with the CIM machine.

```
C       PROGRAM TO DESIGN CAMS FOR PRODUCING
C       HARMONIC MOTION  OF  THE  FOLLOWER

C       NOMENCLATURE
C               UO  : STEADY AREA AVERAGED VELOCITY AT THE ORIFICE
C               F   : FREQUENCY (Hz)
C               EPS : AMPLITUDE (5 OF UO)

C       PROGRAM
                IMPLICIT DOUBLE PRECISION (A-H, O-Z)
                DIMENSION X(400), R(400)
                CHARACTER *30 CAM_DAT

                WRITE (5,*) 'INPUT UO'
                READ(*,*) UO
                WRITE(*,*) 'INPUT FREQUENCY'
                READ(*,*) F
                WRITE(5,*) 'INPUT AMPLITUDE (% OF STEADY MEAN)'
                READ(5,*) EPS
                WRITE(5,*) 'INPUT DATA FILE NAME'
                READ(*,'(A9)') CAM_DAT
                OPEN(2,FILE=CAM_DAT)

                ZERO = 0.D0
                RO = 25.4 D0
                WRITE(2,48) ZERO, RO
                PI = 4.D0*DATAN(1.D0)
                W = 2.D0*PI*F
                A = UO*EPS/(400.D0*W)
                DO 10 I = 1,360
                        XI = I
                        R(I) = RO + A*(1-COS(XI*PI/180.D0))
                        IF (I.LE.9) WRITE (2,48) XI, R(I)
                        IF (I.GE.10.AND.I.LE.99) WRITE (2,49) XI, R(I)
                        IF (I.GE.100) WRITE (2,50) XI, R(I)
```

```
10      CONTINUE
48      FORMAT('A',F6.4,'X',F7.4)
49      FORMAT('A',F7.4,'X',F7.4)
50      FORMAT('A',F8.4,'X',F7.4)
        STOP
        END
```

APPENDIX B

Calibration of rotameter

A steady flow of the jet solution (0.5% ethanol) is passed through the rotameter. Time is allowed for the float in the rotameter to be steady. After the steady state is achieved the fluid passing through the rotameter is collected in a measuring cylinder over a set period of time, usually about 1 minute. The volumetric flow rate is calculated by dividing the volume of collected fluid by the elapsed time. For each rotameter reading atleast three runs are performed and the average of the three volumetric flow rates is plotted against the rotameter reading. The calibration curve is shown in Figure B.1. A straight line is fitted through the data points using least square method. The equation of the curve is given by,

$$Q = 0.382927\ x - 0.572971 \qquad \text{(B.1)}$$

where, Q is volumetric flow rate in cm^3/sec and x is the rotameter reading.

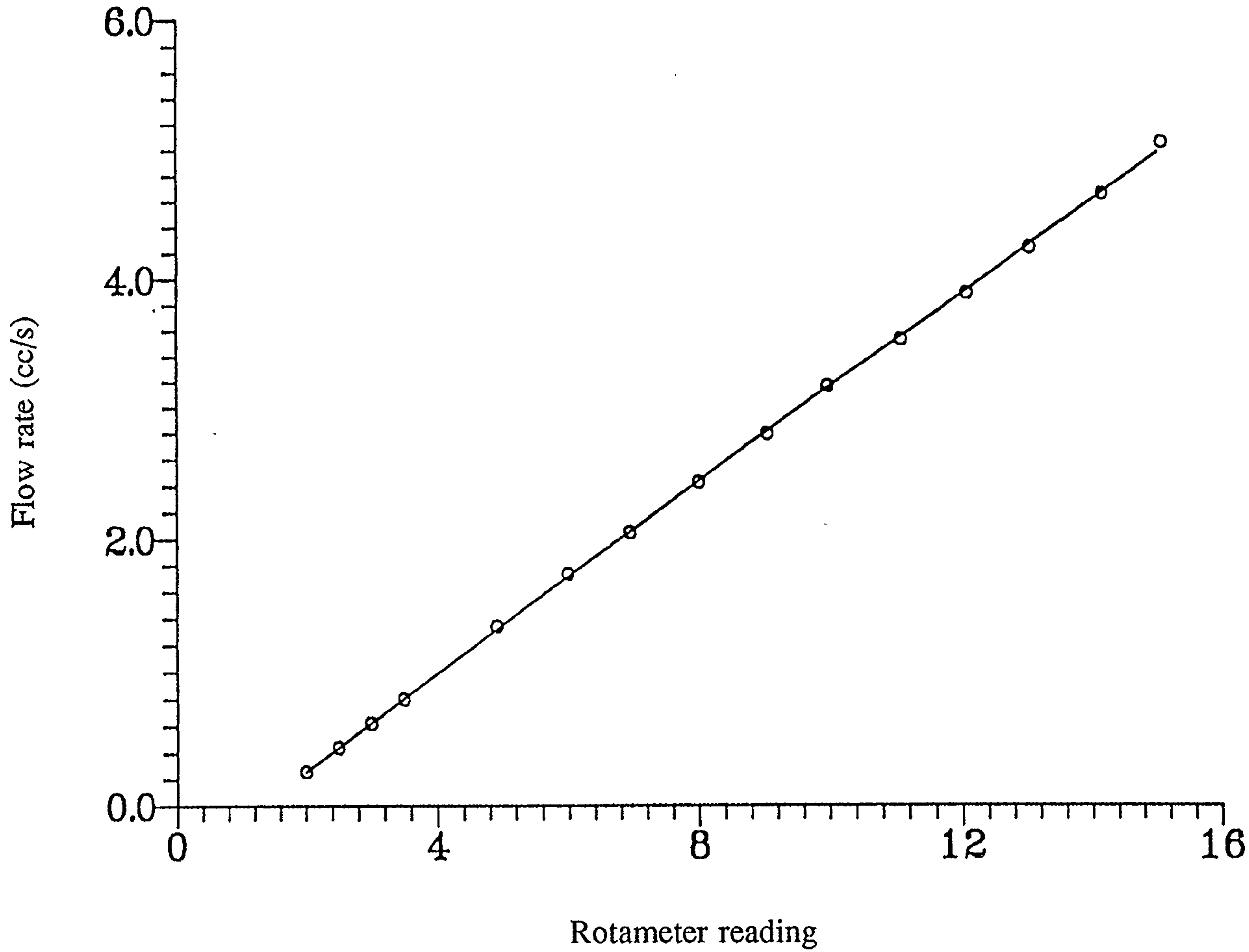

Figure B.1 : Calibration curve for rotameter

APPENDIX C

C.1 Relation between centreline velocity and the area average velocity at the orifice

The relation between the centreline velocity and the area average velocity of the velocity profiles used in section 4 is derived and presented here.

The velocity profiles (Equation 4.40, 4.41 and 4.42) can be represented in a generalized and dimensional form as,

$$u^*(r^*) = \bar{U}_c \left[1 - \left(\frac{2r^*}{D}\right)^n \right] \tag{C.1}$$

where, u^* is the axial velocity, r^* is the radial distance, $\bar{U}_c$ is the centreline velocity and D is the diameter of the orifice. The area average velocity is given by,

$$\bar{U}_0 = \frac{\int_0^{D/2} 2\pi r^* u^*(r^*) dr^*}{\int_0^{D/2} 2\pi r^* dr^*} \tag{C.2}$$

$$= \bar{U}_c \frac{\int_0^{D/2} r^* \left[1 - \left(\frac{2r^*}{D}\right)^n \right] dr^*}{\int_0^{D/2} r^* dr^*} \tag{C.3}$$

Carrying out the integrations one obtains,

$$\frac{\bar{U}_o}{\bar{U}_c} = 1 - \frac{2}{n+2}$$
$$= \frac{1}{2} \text{ for } n = 2 \text{ (Profile I, Equatin 4.40)} \qquad (C.4)$$
$$= \frac{3}{4} \text{ for } n = 6 \text{ (Profile II, Equation 4.41)}$$
$$= \frac{5}{6} \text{ for } n = 10 \text{ (Profile III, equation 4.42)}$$

C.2 Derivation of stream function and vorticity profile at the orifice

The stream function and the vorticity profiles are derived from the corresponding velocity profiles in this section. The nondimensional velocity profiles (Equation 4.40, Equation 4.41 and Equation 4.42) can be represented in a generalized form as follows,

$$U(r) = 1 - (2r)^n \qquad (C.5)$$

The expression for streamfunction is ,

$$\frac{1}{r}\frac{\partial\Psi}{\partial r} = 1 - (2r)^n \qquad (C.6)$$

Integrating with respect to r, one obtains

$$\Psi(r) = \frac{r^2}{2} - \frac{2^n}{n+2} r^{n+2} + c \qquad (C.7)$$

Fixing Ψ equals to zero at the nozzle wall (r = 0.5) the following expression is obtained.

$$\Psi(r) = \frac{r^2}{2} - \frac{2^n}{n+2} + \frac{2^n}{n+2}0.5^{n+2} - \frac{0.5^2}{2} \tag{C.8}$$

The expression for vorticity is derived as,

$$\Omega(r) = \frac{\partial U(r)}{\partial r} = -2^n\, n\, r^{n-1} \tag{C.9}$$